Lagrangian Dynamics of European heat waves

Zur Erlangung des akademischen Grades eines
DOKTORS DER NATURWISSENSCHAFTEN
von der KIT-Fakultät für Physik des
Karlsruher Instituts für Technologie (KIT)

genehmigte

DISSERTATION

von

M. Sc. Philipp Zschenderlein
aus Sindelfingen

Tag der mündlichen Prüfung:	19.06.2020
Referent:	Prof. Dr. Andreas H. Fink
Korreferenten:	Prof. Dr. Joaquim Pinto
	Prof. Dr. Volkmar Wirth (JGU Mainz)

Tell me and I will forget,
show me and I may remember,
involve me and I will understand.

Confucius

Abstract

Heat waves are meteorological extreme events with health and socio-economic impacts. In a changing climate, these events are expected to increase. State-of-the-art numerical weather prediction models are able to forecast the occurrence of heat waves. However, onset, duration, decay and magnitude of these events are still challenging for prediction models and basic understanding of the formation and maintenance of heat waves is still not complete. Therefore, this thesis investigates how high near-surface temperatures during heat waves and the associated upper-tropospheric circulation patterns evolve. Furthermore, the predictability of selected heat wave cases is studied.

The first case study analyses the late summer heat wave over Europe in 2016. Central, western and southwestern Europe are primarily affected by the high temperatures. Seville, Spain, for example, experience the highest September temperature on record on 05 September 2016, reaching a maximum of 44.8°C, and temperatures in Trier, Germany, reaches 34.2°C on 13 September 2016. The heat wave is marked by three distinct peaks, accompanied by record-breaking values for 500-hPa geopotential heights and, to a lesser extent, 850-hPa temperatures. These peaks are associated with the arrival of high-amplitude Rossby wave packets in western Europe. The latter originates several days before the event over western North America. During the three peaks of the heat wave, subsidence and the ensuing adiabatic compression in the free atmosphere in combination with boundary layer processes, rather than local temperature advection, are instrumental in the occurrence of the extreme temperature episodes. Operational ensemble forecasts show, with respect to the model climatology, the highest probabilities for extreme temperatures in Trier, followed by Seville and Bordeaux.

The development of high near-surface temperatures during heat waves is investigated in a climatological analysis across different climates in Europe for the period 1979–2016. Heat waves are defined using a percentile-based index and the main processes quantified along trajectories are adiabatic compression by subsidence and local and remote diabatic processes in the upper- and lower troposphere. This Lagrangian analysis is complemented by an Eulerian calculation of horizontal temperature advection. During typical summers in Europe, one or two heat waves occur with an average duration of five days. Whereas

high near-surface temperatures over Scandinavia are accompanied by omega-like blocking structures at 500 hPa, heat waves over the Mediterranean are connected to comparably flat ridges. Tracing air masses backwards from the heat waves, three trajectory clusters with coherent thermodynamic characteristics, vertical motions, and geographic origins are identified. In all regions, horizontal temperature advection is rather negligible. In two of the three clusters, subsidence in the free atmosphere is very important in establishing high temperatures near the surface, while the air masses in the third cluster are warmed primarily due to diabatic heating near the surface. Large interregional differences occur between the British Isles and western Russia. Over the latter region, near surface transport and diabatic heating appear to be very important in determining the intensity of the heat waves, whereas subsidence and adiabatic warming are of first order importance for the British Isles. Although the large-scale pattern is quasi-stationary during heat wave days, new air masses are steadily entrained into the lower troposphere during the life cycle of a heat wave. Overall, the results of this analysis provide a guideline as to which processes and diagnostics weather and climate studies should focus on to understand the severity of heat waves.

The climatological analysis of high-near surface temperatures during heat waves is followed by a Lagrangian analysis of upper-tropospheric anticyclones that are connected to surface heat waves in different European regions for the period 1979 to 2016. In order to elucidate the formation of these anticyclones and the role of diabatic processes, air parcels are traced backwards from the upper-tropospheric anticyclones and the diabatic heating in these air parcels is quantified. Around 25-45% of the air parcels are diabatically heated during the last three days prior to their arrival in the upper-tropospheric anticyclones and this amount increases to 35-50% for the last seven days. The influence of diabatic heating is larger for heat wave-related anticyclones in northern Europe and western Russia and smaller in southern Europe. Interestingly, the diabatic heating occurs in two geographically separated air streams. Three days prior to arrival, one heating branch (remote branch) is located above the western North Atlantic and the other heating branch (nearby branch) is located over nortwestern Africa/Europe to the southwest of the target upper-tropospheric anticyclone. The diabatic heating in the remote branch is related to warm conveyor belts in North Atlantic cyclones upstream of the evolving upper-level ridge. In contrast, the nearby branch is diabatically heated by convection, as indicated by elevated mixed-layer convective available potential energy along the western side of the matured upper-level ridge. Most European regions are influenced by both branches, whereas western Russia is predominantly affected by the nearby branch. The remote branch predominantly affects the formation of the upper-tropospheric anticyclone, and therefore of the heat wave, whereas the nearby branch is more active during its maintenance. For long-lasting heat waves, the remote branch regenerates. The results from

this study show that the dynamical processes leading to heat waves may be sensitive to small-scale microphysical and convective processes, whose accurate representation in models is thus supposed to be crucial for heat wave predictions on weather and climate time scales.

The thesis closes with the predictability of a long-lasting heat wave, which affected large parts of Central Europe from 24 July to 09 August 2018. Both 3- and 7-day operational forecasts often underestimate 2-m temperatures averaged over the heat wave area. Errors on the 7-day time scale are related to upper-tropospheric dynamics, as shown by a consistent underestimation of 500-hPa geopotential height. However, 500-hPa geopotential height errors are considerably reduced in 3-day forecasts and for this lead time, prediction errors are related to physical processes along trajectories. In a new and unique approach that is based on a combination of trajectories from reanalysis and predictions, it is found that 2-m temperature errors of 3-day forecasts are mostly due to diabatic processes in the planetary boundary layer. In forecasts underestimating 2-m temperature, the diabatic heating along trajectories between 12 and 18 UTC is considerably underestimated. The temperature error at the location of the heat wave is confined to the planetary boundary layer and substantially reduced in the free atmosphere.

Kurzfassung

Hitzewellen sind meteorologische Extremereignisse mit gesundheitlichen und sozioökonomischen Auswirkungen. In einem sich verändernden Klima ist zu erwarten, dass diese Ereignisse zunehmen werden. Modernste numerische Wettervorhersagemodelle sind in der Lage, das Auftreten von Hitzewellen vorherzusagen. Beginn, Dauer, Ende und Ausmaß der Ereignisse stellen jedoch nach wie vor eine Herausforderung für die Vorhersagemodelle dar und das grundlegende Verständnis der Entstehung und Aufrechterhaltung von Hitzewellen ist noch immer nicht vollständig. Daher wird in dieser Arbeit untersucht, wie sich hohe oberflächennahe Temperaturen während Hitzewellen und die damit verbundenen obertroposphärischen Zirkulationsmuster entwickeln. Darüber hinaus wird die Vorhersagbarkeit ausgewählter Hitzewellen untersucht.

Die erste Fallstudie analysiert die spätsommerliche Hitzewelle über Europa im Jahr 2016. Mittel-, West- und Südwesteuropa sind in erster Linie von den hohen Temperaturen betroffen. Sevilla (Spanien) erlebt am 5. September 2016 mit 44,8°C die höchste jemals gemessene Temperatur im September und in Trier (Deutschland) erreichen die Temperaturen am 13. September 2016 34,2°C. Die Hitzewelle ist durch drei deutliche Spitzenwerte gekennzeichnet, begleitet von Rekordwerten der geopotentiellen Höhe in 500 hPa und, in geringerem Maße, der Temperatur in 850 hPa. Diese Spitzenwerte stehen im Zusammenhang mit der Ankunft von hochamplitudigen Rossby-Wellenpaketen in Westeuropa. Letztere entstehen einige Tage vor dem Ereignis über dem Westen Nordamerikas. Während der drei Peaks der Hitzewelle ist nicht die lokale Temperaturadvektion, sondern das Absinken und die daraus resultierende adiabatische Kompression in der freien Atmosphäre in Kombination mit Grenzschichtprozessen für das Auftreten der extremen Temperaturepisoden verantwortlich. Operationelle Ensemblevorhersagen zeigen in Bezug auf die Modellklimatologie die höchsten Wahrscheinlichkeiten für extreme Temperaturen in Trier, gefolgt von Sevilla und Bordeaux.

Die Entwicklung hoher oberflächennaher Temperaturen während Hitzewellen wird für den Zeitraum von 1979 bis 2016 für verschiedene Klimazonen in Europa analysiert. Hitzewellen werden mit Hilfe eines auf einem Perzentil basierenden Index definiert und die Hauptprozesse, die entlang der Trajektorien quantifiziert werden, sind die adiabati-

sche Kompression durch Absinken sowie lokale und entfernte diabatische Prozesse in der oberen und unteren Troposphäre. Diese Lagrangesche Analyse wird durch eine Euler'sche Berechnung der horizontalen Temperaturadvektion ergänzt. Während typischer Sommer in Europa treten ein oder zwei Hitzewellen mit einer durchschnittlichen Dauer von fünf Tagen auf. Während hohe oberflächennahe Temperaturen über Skandinavien von omega-ähnlichen Verteilungen der geopotentiellen Höhe in 500 hPa begleitet werden, sind Hitzewellen über dem Mittelmeer mit vergleichsweise flachen Rücken verbunden. Wenn die Luftmassen von den Hitzewellen rückwärts verfolgt werden, können drei Trajektoriencluster mit kohärenten thermodynamischen Eigenschaften, vertikalen Bewegungen und geographischen Ursprüngen identifiziert werden. In allen Regionen ist die horizontale Temperaturadvektion eher vernachlässigbar. In zwei der drei Cluster ist das Absinken in der freien Atmosphäre sehr wichtig, um hohe Temperaturen nahe der Oberfläche zu erzeugen, während sich die Luftmassen im dritten Cluster hauptsächlich aufgrund der diabatischen Erwärmung nahe der Oberfläche erwärmen. Große interregionale Unterschiede treten zwischen den Britischen Inseln und Westrussland auf. In der letztgenannten Region scheinen oberflächennaher Transport und diabatische Erwärmung sehr wichtig für die Bestimmung der Intensität der Hitzewellen zu sein, während für die Britischen Inseln Absinken und adiabatische Erwärmung von Bedeutung sind. Obwohl das großräumige Muster während der Hitzewellentage quasi-stationär ist, werden während des Lebenszyklus einer Hitzewelle ständig neue Luftmassen in die untere Troposphäre transportiert. Insgesamt bieten die Ergebnisse dieser Analyse einen Leitfaden, auf welche Prozesse und Diagnoseverfahren sich Wetter- und Klimastudien konzentrieren sollten, um die Schwere von Hitzewellen zu verstehen.

Auf die klimatologische Analyse hoher Oberflächentemperaturen während Hitzewellen folgt eine Lagrangesche Analyse von obertroposphärischen Antizyklonen, die in verschiedenen europäischen Regionen im Zeitraum von 1979 bis 2016 mit bodennahen Hitzewellen in Verbindung stehen. Um die Bildung dieser Antizyklonen und die Rolle diabatischer Prozesse zu klären, werden Luftpakete rückwärts von den obertroposphärischen Antizyklonen verfolgt und das diabatische Heizen in diesen Luftpaketen quantifiziert. Etwa 25-45% der Luftpakete werden in den letzten drei Tagen vor ihrer Ankunft in den obertroposphärischen Antizyklonen diabatisch geheizt, und dieser Anteil steigt in den letzten sieben Tagen auf 35-50%. Der Einfluss des diabatischen Heizens ist bei hitzewellenbedingten Antizyklonen in Nordeuropa und Westrussland größer und in Südeuropa kleiner. Interessanterweise findet das diabatische Heizen in zwei geographisch getrennten Luftströmen statt. Drei Tage vor der Ankunft befindet sich ein diabatisch geheizter Luftstrom (entfernter Luftstrom) über dem westlichen Nordatlantik und der andere diabatisch geheizte Luftstrom (nahe gelegener Luftstrom) über Nordwestafrika/Europa südwestlich der obertroposphärischen Zielantizyklone. Das diabatische Heizen im ent-

fernten Luftstrom steht im Zusammenhang mit warm conveyor belts in nordatlantischen Zyklonen stromaufwärts des sich entwickelnden obertroposphärischen Rückens. Im Gegensatz dazu wird der nahegelegene Luftstrom durch Konvektion diabatisch geheizt, was durch eine erhöhte konvektiv verfügbare potenzielle Energie entlang der Westseite der stärker ausgeprägten obertroposphärische Antizyklone deutlich wird. Die meisten europäischen Regionen werden von beiden Luftströmen beeinflusst, während Westrussland überwiegend vom nahe gelegenen Luftstrom betroffen ist. Der entfernte Luftstrom beeinflusst vorwiegend die Bildung der obertroposphärischen Antizyklone und damit der Hitzewelle, während der nahe Luftstrom während der Aufrechterhaltung der Antizyklone aktiver ist. Bei lang anhaltenden Hitzewellen regeneriert sich der entfernte Luftstrom wieder. Die Ergebnisse dieser Studie zeigen, dass die dynamischen Prozesse, die zu Hitzewellen führen, möglicherweise empfindlich auf kleinskalige mikrophysikalische und konvektive Prozesse reagieren, deren genaue Darstellung in Modellen daher für die Vorhersage von Hitzewellen auf Wetter- und Klimazeitskalen entscheidend sein dürfte.

Die Arbeit schließt mit der Vorhersagbarkeit einer lang anhaltenden Hitzewelle, die vom 24. Juli bis zum 9. August 2018 weite Teile Mitteleuropas erfasste. Sowohl 3- als auch 7-tägige operationelle Vorhersagen unterschätzen oft die über das Gebiet der Hitzewelle gemittelten 2-m-Temperaturen. Fehler auf der 7-Tage-Zeitskala hängen mit der Dynamik in der oberen Troposphäre zusammen, wie eine konsistente Unterschätzung der geopotentiellen Höhe von 500 hPa zeigt. Allerdings sind die Fehler von 500 hPa geopotentieller Höhe bei 3-Tages-Vorhersagen erheblich reduziert, und für diese Vorlaufzeit hängen die Vorhersagefehler mit physikalischen Prozessen entlang der Trajektorien zusammen. In einem neuen und einzigartigen Ansatz, der auf einer Kombination von Trajektorien aus Reanalysen und Vorhersagen basiert, wird festgestellt, dass 2-m-Temperaturfehler von 3-Tages-Vorhersagen hauptsächlich auf diabatische Prozesse in der planetaren Grenzschicht zurückzuführen sind. Bei Vorhersagen, die die 2-m-Temperatur unterschätzen, wird die diabatische Erwärmung entlang von Trajektorien zwischen 12 und 18 UTC erheblich unterschätzt. Der Temperaturfehler am Ort der Hitzewelle ist auf die planetare Grenzschicht beschränkt und in der freien Atmosphäre deutlich reduziert.

Preface

The PhD candidate confirms that the research presented in this thesis contains significant scientific contributions by himself. This thesis reuses material from the following publications:

- Zschenderlein, P., Fragkoulidis, G., Fink, A.H. and Wirth, V. Large-scale Rossby wave and synoptic-scale dynamic analyses of the unusually late 2016 heatwave over Europe. *Weather*, 73(9):275–283, 2018. doi: 10.1002/wea.3278.
- Zschenderlein, P., Fink, A.H., Pfahl, S. and Wernli, H. Processes determining heat waves across different European climates. *Quarterly Journal of the Royal Meteorological Society*, 145(724):2973–2989, 2019. doi: 10.1002/qj.3599.
- Zschenderlein, P., Pfahl, S., Wernli, H. and Fink, A. H. A Lagrangian analysis of upper-tropospheric anticyclones associated with heat waves in Europe. *Weather and Climate Dynamics*, 1, 191–206, 2020. doi: 10.5194/wcd-1-191-2020.

Firstly, the abstract and Chapters 1, 3, 4, 5 and 9 reuse material from Zschenderlein et al. (2018). Secondly, the abstract and Chapters 1, 2, 3, 4, 6, 9, 10 and the Appendix A.1 reuse material from Zschenderlein et al. (2019). And thirdly, the abstract and chapters 1, 2, 3, 7, 9, 10 and the Appendix A.2 reuse material from Zschenderlein et al. (2020).

The research leading to these results has been conducted within the subproject C4: Coupling of planetary-scale Rossby wave trains to local extremes in heat waves over Europe of the Transregional Collaborative Research Center SFB/TRR 165 ”Waves to Weather”, funded by the German Research Foundation (DFG). The research proposal of this thesis has been written by Andreas H. Fink and Volkmar Wirth. Analyses in Zschenderlein et al. (2018) were predominantly performed by the candidate, who also wrote the text, but analyses of the Rossby wave packets was performed by Georgios Fragkoulidis and advice came from Andreas H. Fink and Volkmar Wirth. Analyses in Zschenderlein et al. (2019) and Zschenderlein et al. (2020) were solely performed by the candidate, who also wrote the text with advice from Andreas H. Fink, Stephan Pfahl and Heini Wernli. Chapter 8 was solely performed by the candidate, who also wrote the text with advice from Andreas H. Fink and Julian Quinting.

Contents

Chapter 1

Introduction

Heat waves are periods of unusually warm temperatures at the surface above a particular threshold (Robinson, 2001). Recent long-lasting and intense heat waves in Europe occurred in 2003, 2010, 2015, 2018, and 2019. In 2003, mean summer (June, July and August) temperatures exceeded 5 standard deviations compared to the climatological values for 1961–1990 (Schär et al., 2004). A long-lasting heat wave dominated nearly the entire summer of 2010 in Russia with new all-time temperature records (Grumm, 2011). The intense heat wave in 2015 affected many regions in Europe (Dong et al., 2016) and was accompanied by unusually cold sea surface temperatures in the North Atlantic (Duchez et al., 2016), and in 2018, large parts north of 30°N were affected by several concurrent heat waves (Kornhuber et al., 2019; Vogel et al., 2019). During a heat wave in July 2019, many parts of western and central Europe exceeded daily maximum temperatures of 40°C and some countries registered new temperature records (DWD, 2019).

Heat waves are natural hazards and lead to various impacts on society, economy and ecology (Fink et al., 2004; Robine et al., 2008; Seneviratne et al., 2012; WMO and WHO, 2015; Horton et al., 2016; Xu et al., 2016). The concurrent heat waves in 2018 led to deaths, wildfires, crop losses and power shortages in many countries (Vogel et al., 2019). High temperatures reduce labour capacity, especially of people working outdoors (Watts et al., 2018). As an example for the agricultural sector, a reduction of labour capacity leads to smaller harvests for farmers (Watts et al., 2018) and thus increased prices for consumers. During the 2012 heat wave in the United States, crop failures of maize led to a worldwide increase of corn prices (Chung et al., 2014). High temperatures and reduced precipitation amounts lead to water shortages and stress for plants (UNEP, 2004), increasing the probability of forest fires, as for example during the extreme 2010 heat wave in Russia (Gilbert, 2010). A long-lasting heat and drought period led to wildfires over California in 2017 and costed the re-insurances 13 billion US-Dollar (MunichRe, 2018). Forest fires enhance the climate-carbon feedback cycle leading to a higher atmospheric

CO_2 content (Frank et al., 2015). Heat waves can also accelerate glacier melt (Fink et al., 2004), for example, the 2003 heat wave led to a 10% decrease of glacier mass in Europe (UNEP, 2004).

In the view of global warming, heat waves are particularly relevant. According to the 5th Intergovernmental Panel on Climate Change (IPCC) report, it is virtually certain (99-100% probability, cf. Mastrandrea et al., 2010) that heat waves in Europe will be more frequent and intense at the end of the twenty-first century (Collins et al., 2013). Observations show an accelerated increase in mean surface temperatures over Europe since the middle of the twentieth century and observational studies hint at an already elevated probability of heat waves in this region (Hartmann et al., 2013).

Due to the various impacts of heat waves and projected increase of these events in a changing climate, it is pivotal to correctly understand the physical processes leading to the formation and maintenance of heat waves (Messori et al., 2018). Improved process understanding helps to improve weather forecasting systems that are relevant to warn, amongst others, the general public, economy or transport. Although current weather forecasting systems are able to predict the occurrence of heat waves within a one-week lead time, onset and duration, as well as the intensity of heat waves are still challenging for current forecast models (Weisheimer et al., 2011; Lavayasse et al., 2018; Magnusson et al., 2018).

A heat wave is a meteorological phenomenon including a variety of temporal and spatial scales. On the planetary scale, strong Rossby wave activity in the upper troposphere leads to perturbations in the meridional flow (Schubert et al., 2011; Lau and Kim, 2012) and transports hot air from south to north and cold air from north to south (Lackmann, 2011). Embedded in these upper-tropospheric waves, synoptic-scale upper-tropospheric anticyclones are steered by the waves. These anticyclones are often co-located with heat waves, especially when anticyclones become persistent (Pfahl and Wernli, 2012). Processes within the air masses of the anticyclones, e.g. warm air advection, subsidence, diabatic heating, become more relevant for the development of the local heat wave (Bieli et al., 2015). In the lower troposphere and at the location of the heat wave, meso-scale processes, especially land-atmospheric feedbacks, can further amplify near-surface temperatures (Fischer et al., 2007).

This chain of processes is the research area of the project, in which this thesis is embedded. The focus of this thesis is on the synoptic- and meso-scale dynamics of European heat waves with following **main research aims**:

A Determine processes leading to high near-surface temperatures during heat waves.

B Determine processes leading to upper-tropospheric anticyclones associated with heat waves.

C Analyse predictability and predictive skill of near-surface temperatures during heat waves.

At first, the thesis provides a review of existing literature on the definition of heat waves (section 2.1), on physical processes leading to heat waves (section 2.2) and on the predictability and predictive skill of the events (section 2.3). Then, specific research questions are raised and motivated in order to reach the main research aims A–C. Subsequently, data and methods are described in Chapter 4. Chapters 5 and 6 address research aim A, Chapter 7 addresses research aim B and Chapters 5 and 8 address research aim C. The thesis closes with a summary and avenues for further research in Chapters 9 and 10.

Chapter 2

Literature review

This chapter reviews the current scientific knowledge on aspects of heat waves relevant for this thesis. Section 2.1 starts with a discussion on the definition of heat waves and presents commonly used heat wave indices. In the second part of the literature review, relevant process contributing to the development of heat waves are discussed: the general concept of potential vorticity is introduced in subsection 2.2.1, followed by a brief overview of the role of Rossby wave packets (subsection 2.2.2) and a more thorough discussion on the upper-tropospheric anticyclonic systems associated with heat waves (subsection 2.2.3), the evolution of high near-surface temperatures during heat waves (subsection 2.2.4) and land-atmospheric feedbacks (subsection 2.2.5). The literature review closes with relevant aspects on the predictability of heat waves in section 2.3.

2.1 Heat wave definitions

Depending on the meteorological variable or the type of impact, a heat wave can be defined in many different ways (Horton et al., 2016). In general, heat wave definitions should reflect the intensity, duration and frequency of the events. They are typically based on a type of temperature, e.g. maximum temperature, but can also include humidity (Perkins, 2015). Interesting characteristics deduced from the definitions are, for example, number of heat wave days, whether heat waves increase due to global warming, or how these events impact on human health, agriculture, wildfire, or power. The remainder of this section gives an overview of commonly used indices and closes with a description of the heat wave index utilised in this thesis.

The definition of heat waves can be divided into the following two groups: absolute and relative thresholds. Absolute thresholds are more suitable for assessing societal impacts (Horton et al., 2016). For example, the index ”apparent temperature” is based on temperature and relative humidity and reflects the effects of heat stress on the human

body[1]. The disadvantage of an absolute threshold is that the identified heat waves cannot be compared across different climates. To circumvent this disadvantage, relative thresholds, e.g. percentiles, reflect the local climate and, when calculated for each calendar-day individually, consider the seasonal cycle. This kind of heat wave definition is therefore applicable to all seasons (Perkins, 2015).

A first major global framework to establish international recognised measures for extreme indices was the formation of the Expert Team on Climate Change Detection (ETCCDI, Alexander et al., 2006) under the umbrella of the World Meteorological Organisation (WMO). In this framework, a couple of measures, e.g. maximum daily maximum temperature (i.e. highest annual or seasonal daily maximum temperature), annual occurrence of summer days (maximum temperatures above 25°C), were developed. Moreover, workshops were organised to increase data availability especially in data-sparse countries. This helped to compare the occurrence of heat waves across the globe.

Apart from the ETCCDI, many studies develop their own definitions and some of them are presented in the following. Meehl and Tebaldi (2004) introduce two concepts of heat indices. At first, the "worst heat event" identifies the highest three consecutive nighttime minimum temperatures. In their second concept, they define heat waves as the longest period where following three conditions are fulfilled: (i) daily maximum temperature above the 97.5th percentile for at least three days, (ii) average daily maximum above the 97.5th percentile for all days and (iii) daily maximum temperature above the 81st percentile for all days. Fischer and Schär (2010) define heat waves as periods in which the 90th percentile is exceeded for at least six consecutive days. In order to account for the seasonal cycle, the 90th percentile is calculated for every calendar day with a 15-day running mean. Deduced from this index, they identify average annual frequency and number of heat waves, as well as mean hottest summer temperatures and durations of the longest heat waves. To discard individual hot grid points, Stefanon et al. (2012) utilise a minimum spatial threshold. Nairn and Fawcett (2013) introduce the excess heat factor and define heat waves as periods of at least three consecutive days, where the average maximum and minimum temperature exceeds the 95th percentile and is anomalously warm compared to the preceding 30 days.

In order to reduce the number of existing heat wave indices, Perkins and Alexander (2013) and Perkins et al. (2012) initiate a framework and define a heat wave based on three measures: daily minimum temperature, daily maximum temperature and the excess heat factor (Nairn and Fawcett, 2013). The measures must exceed their calendar-day 90th percentiles for at least three successive days. Based on these measures, different heat wave characteristics can be deduced: number of discrete events, onset/decay of events,

[1]https://www.ncdc.noaa.gov/societal-impacts/apparent-temp/app-temp, last accessed: 28 April 2020

average heat wave magnitude, heat wave days and others (Fig. 2.1).

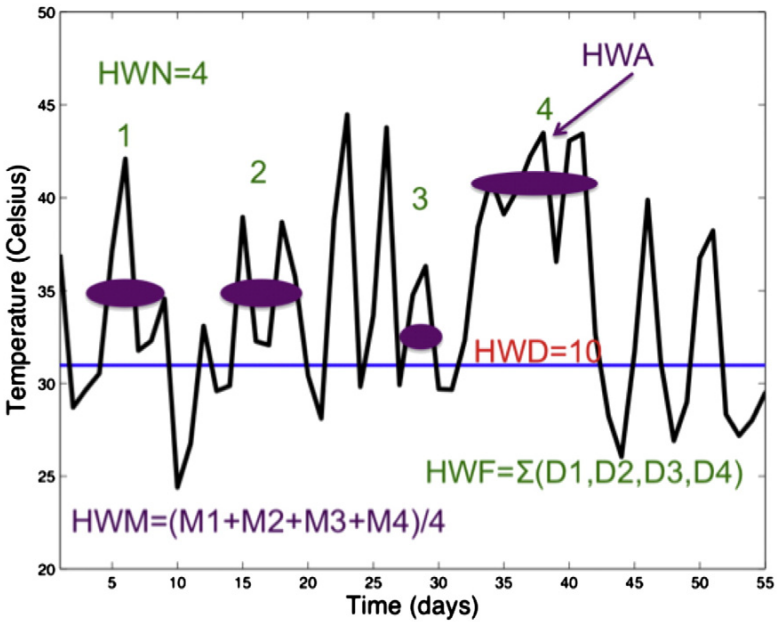

Figure 2.1: Multi-characteristic framework for heat waves based on Perkins and Alexander (2013) and Perkins et al. (2012). The schematic shows a 55-day time series of temperature and the threshold value (90th percentile, blue line) that must be exceeded to detect a heat wave. Four discrete heat wave events occur (HWN, heat wave number), the longest heat wave lasts 10 days (HWD, heat wave duration), number of heat wave days is the sum of all events (HWF), heat wave amplitude is the hottest day of the event with the hottest average (HWA, heat wave amplitude) and the heat wave magnitude is the average temperature across all four events (HWM, heat wave magnitude). Reprinted from Perkins (2015), © 2015, with permission from Elsevier.

Recently, Russo et al. (2015) proposed the Heat Wave Magnitude Index daily, abbreviated HWMId, which is applicable to different climates. The HWMId combines duration and magnitude of a heat wave. The duration is defined as a period of at least three consecutive days above a threshold. For a certain day d, this threshold is calculated as the 90th percentile of the following days (set A_d):

$$A_d = \bigcup_{y=1981}^{2010} \bigcup_{i=d-15}^{d+15} T_{y,i}, \tag{2.1}$$

where $\bigcup$ denotes the union of sets and $T_{y,i}$ the maximum daily temperature of day i in year y.

The magnitude M_d of a given heat wave day is calculated as follows:

$$\mathrm{M_d}(\mathrm{T_d}) = \begin{cases} \dfrac{\mathrm{T_d} - \mathrm{T_{30y25p}}}{\mathrm{T_{30y75p}} - \mathrm{T_{30y25p}}} & \text{if} \quad \mathrm{T_d} > \mathrm{T_{30y25p}} \\ 0 & \text{if} \quad \mathrm{T_d} \leq \mathrm{T_{30y25p}}, \end{cases} \tag{2.2}$$

where $\mathrm{T_d}$ denotes the maximum daily temperature and $\mathrm{T_{30y75p}}(\mathrm{T_{30y25p}})$ the 75$^{\text{th}}$ (25$^{\text{th}}$) percentile of *annual* maximum temperatures of the reference period 1981–2010. The magnitude of the heat wave is the sum of all days compositing the heat wave.

When calculating the magnitude of the heat wave, only intense heat waves are considered because temperatures must exceed the 25$^{\text{th}}$ percentile of annual maximum temperatures. Therefore, magnitudes can only be derived for summer heat waves. A HWMId of 1 implies that the temperature $\mathrm{T_d}$ is equal to $\mathrm{T_{30y75p}}$ and a magnitude of 5 that the temperature anomaly is 5 times the inter quartile range (denominator in Eq. 2.2). Based on HWMId, the five strongest heat waves are the heat waves in Russia (2010), Central Europe (2003), Finland (1972), United Kingdom (1976) and Norway (1969; cf. Tab. 1 in Russo et al., 2015).

2.2 Processes

Heat waves are preceded by processes on different temporal and spatial scales, as mentioned in the Introduction. This section presents the different processes, starting with the planetary- and synoptic-scale and continuing with the meso-scale feedbacks in the boundary layer at the location of the heat wave. Planetary-scale processes are only briefly discussed because this thesis focuses more on the synoptic- and meso-scale. The concept of potential vorticity (PV) is firstly introduced, because processes on the planetary and synoptic scale are often analysed using the PV concept.

2.2.1 The general concept of potential vorticity

PV was first described by Rossby (1940) and Ertel (1942) and is a quantity combining the conservation of absolute circulation and mass (Hoskins, 2015). This can be better understood, when discussing the conserved quantities for a cylinder between two isentropic surfaces (Fig. 2.2). Provided that no frictional or diabatic sources exist, the blue circuits on the two isentropic surfaces remain on those surfaces and circulation C is conserved. The circulation is defined as:

$$\mathrm{C} = \zeta_n \cdot \delta \mathrm{S}, \tag{2.3}$$

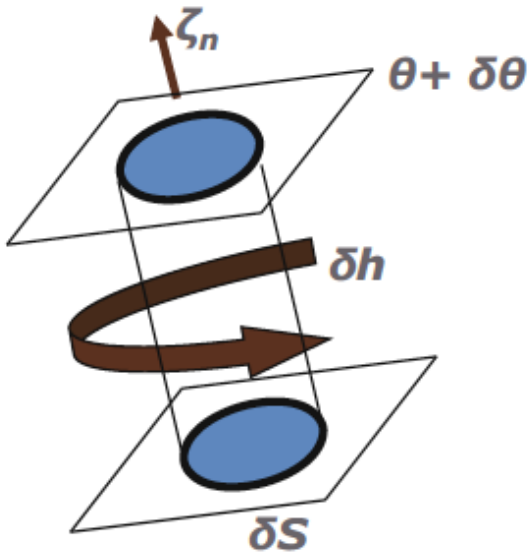

Figure 2.2: Schematic of a cylinder between two isentropic surfaces θ and $\theta+\delta\theta$. δh indicates the height of the cylinder and δS the intersections of the cyclinder with the isentropic surfaces. The arrow indicates the sense of rotation and ζ_n the vorticity normal to the surface. Reprinted by permission from Springer Nature: Hoskins (2015), © 2015.

where ζ_n is the vorticity normal to the isentropic surfaces. The second conserved quantity is mass and defined as:

$$\mathrm{m} = \rho \cdot \delta\mathrm{S} \cdot \delta\mathrm{h}, \tag{2.4}$$

where ρ denotes the density and δh the height of the cylinder. The principle of PV is obtained when dividing Eq. 2.3 by 2.4, and because both mass and circulation are conserved, the term

$$\frac{\mathrm{C}}{\mathrm{m}} = \frac{\zeta_n}{\rho \cdot \delta\mathrm{h}} \tag{2.5}$$

is materially conserved. As an example, when the cylinder is stretched, δh is increasing, and the vorticity ζ_n must increase. Multiplying Eq. 2.5 with $\delta\theta$ and since $|\vec{\nabla}\theta| = \frac{\delta\theta}{\delta h}$, PV is defined as:

$$\mathrm{PV} = \frac{1}{\rho}\vec{\zeta_a} \cdot \vec{\nabla}\theta, \tag{2.6}$$

where $\vec{\zeta_a}$ is the absolute vorticity vector and $\vec{\nabla}\theta$ the three-dimensional gradient of po-

tential temperature (Hoskins et al., 1985). The unit of PV is $\mathrm{m^2\,s^{-1}\,K\,kg^{-1}}$ and typically converted to PV units (1 PVU = $10^{-6}\,\mathrm{K\,kg^{-1}\,m^2\,s^{-1}}$).

In adiabatic, frictionless motions, PV is materially conserved, whereas in cases of diabatic and frictional forces, the PV tendency equation reads:

$$\frac{d\mathrm{PV}}{d\mathrm{t}} = \frac{1}{\rho}\vec{\zeta_a} \cdot \vec{\nabla}\dot{\theta} + \frac{1}{\rho}(\vec{\nabla} \times \vec{F}) \cdot \vec{\nabla}\theta, \tag{2.7}$$

where $\dot{\theta}$ is the diabatic heating rate and $\vec{F}$ the friction (Hoskins et al., 1985).

In the free atmosphere, frictional processes can be neglected and the material derivative of PV therefore depends only on the vertical gradient of potential temperature tendencies. For synoptic-scale motions, PV changes are sufficiently described in pressure coordinates as:

$$\frac{d\mathrm{PV}}{d\mathrm{t}} = -g\zeta_a\frac{\partial\dot{\theta}}{\partial p}, \tag{2.8}$$

where g is the acceleration due to gravity (Martin, 2006).

Hence, the vertical gradient of potential temperature tendencies is vital in synoptic-scale systems. Figure 2.3 sketches a trajectory, starting from the lower troposphere and ascending towards the upper troposphere. In the middle, a diabatic heating source is added and, according to Eq. 2.8, PV is generated below the level of maximum diabatic heating and destroyed above. This mechanism is further discussed in subsection 2.2.3.

2.2.2 Rossby wave packets

Weather in the midlatitudes is mainly driven by the westerlies in the upper troposphere, the so-called jetstream (e.g. Hall et al., 2015). Meridional undulations from the zonal jetstream are referred to as Rossby waves that transport energy, moisture and momentum across the globe (Wirth et al., 2018). When amplitudes of Rossby waves are enhanced in a longitudinally confined band, they are defined as Rossby wave packets (RWP, Wirth et al., 2018). Figure 2.4 illustrates two main characteristics of RWPs: (i) they appear as enhanced anomalies of the meridional wind in the upper troposphere and (ii) are typically not circumglobal, even when anomalies are averaged over a period of 10 days.

Lower-tropospheric temperature extremes are often associated with high-amplitude RWPs in the northern hemisphere, especially over the continents and during summer (Fragkoulidis et al., 2018). The high-impact heat wave during summer 2003, affecting large parts of western Europe (Fink et al., 2004; Trigo et al., 2005), was associated with a

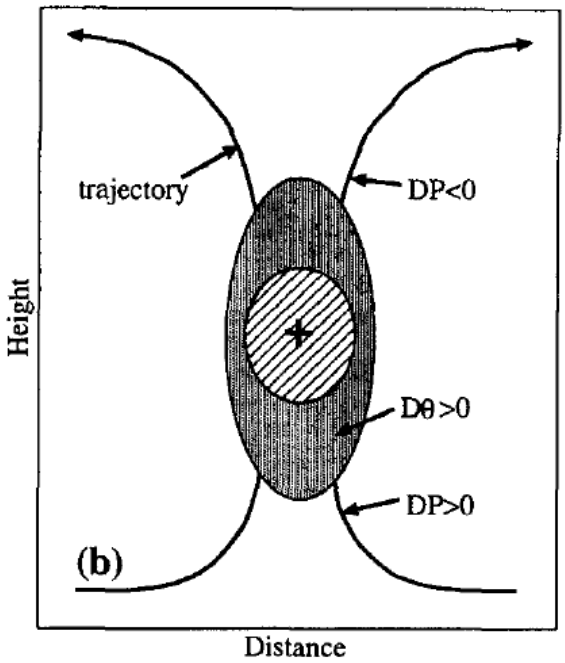

Figure 2.3: Schematic of trajectories (solid lines) ascending from the planetary boundary layer to the upper troposphere. The positive sign indicates diabatic heating, hatched and shaded regions indicate regions of diabatic heating. DP and Dθ indicates material derivatives of potential vorticity and potential temperature, respectively. Figure taken from Wernli and Davies (1997). © 1997 John Wiley and Sons.

high amplitude, non-circumglobal RWP originating from western North America around seven days prior to the heat wave and attaining the highest amplitude when hottest temperatures in Europe were recorded (Fragkoulidis et al., 2018). Also, the 2010 heat wave in Russia was associated with RWPs, but maximum temperatures were reached without a strong RWP activity (Fragkoulidis et al., 2018), hence, processes on other temporal and spatial scales are relevant.

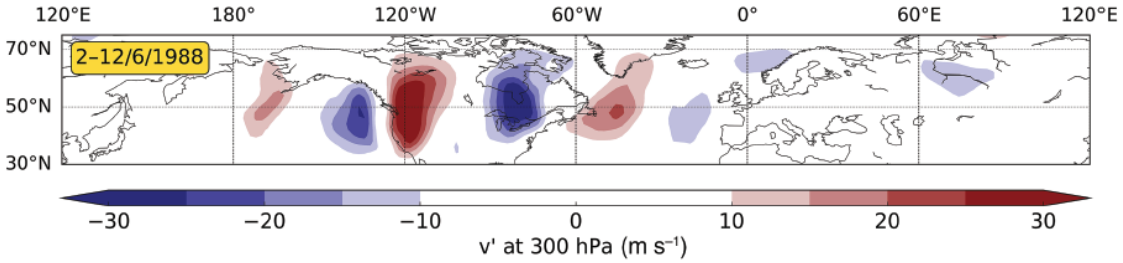

Figure 2.4: Rossby wave packet characteristics. 10-day mean (2-12 June 1988) of 300-hPa meridional wind anomalies v' (colours). Figure taken from Fragkoulidis et al. (2018). © 2018 John Wiley and Sons, CC-BY.

2.2.3 Link between blocking and heat waves

Atmospheric blocks interrupt the prevalent westerlies in the upper troposphere and can lead to a revearsal of the zonal flow in the middle and high latitudes (Tyrlis and Hoskins, 2008; Woollings et al., 2018). These systems can be identified based on absolute meteorological fields, e.g. geopotential height or potential vorticity, as well as deviations from climatology, e.g. the zonal mean (Tibaldi and Molteni, 1990; Pelly and Hoskins, 2003; Barriopedro et al., 2010). When applying the PV-perspective, blocks are viewed as quasi-stationary negative PV anomalies in the upper troposphere (Schwierz et al., 2004). The persistent anticyclonic circulation of blocks drives subsidence, which leads to strong heating of air masses due to adiabatic compression (Pfahl and Wernli, 2012). Furthermore, subsidence leads to clear-sky conditions and increased incoming solar radiation (Trigo et al., 2004). Therefore, blocks provide conditions conducive to heat waves.

Atmospheric blockings are often linked to high-impact weather events. For example, heat waves in Europe in summer 1976 (Green, 1977), in southern and southeastern USA in 1980 (Karl and Quayle, 1981), in Russia in 2010 (Matsueda, 2011), but also cold spells, e.g. the European winter of 2010 (Cattiaux et al., 2010), are associated with blockings.

Pfahl and Wernli (2012) investigated the statistical link between atmospheric blocking and temperature extremes in summer and found a robust connection between blocking and high temperature events over the northern hemisphere. Climatologically, summer blockings occur more frequently over the eastern parts of North Pacific and North Atlantic, respectively, and less over western North America (Fig. 2.5a). The probability of a co-located high temperature extreme and a block is higher for continents than for oceans, and generally more pronounced for northern Europe compared to southern Europe (Fig. 2.5b). Hence, there is a significant relation between blocking and high temperature extremes. Schaller et al. (2018), using large climate model ensembles, demonstrated that this relationship between heat waves and blocking will not be modified in the future. However, high temperature extremes in southern Europe, especially over the Iberian Peninsula, but also in parts of Central and western Europe are less influenced by blockings, as climatologically shown by Sousa et al. (2018). In these regions, heat waves are often caused by intense subtropical ridges extending to southern Europe (Sousa et al., 2018) or by a displacement of a North Atlantic subtropical high to Central Europe (Garcia-Herrera et al., 2010). In addition, a deep trough covering the North Atlantic Ocean with an adjacent ridge downstream over the European continent can lead to warm air mass advection from northern Africa and the Mediterranean basin (Cassou et al., 2005).

Both blockings and subtropical ridges are associated with negative PV anomalies in the upper troposphere (Schwierz et al., 2004). These anomalies are the result of isen-

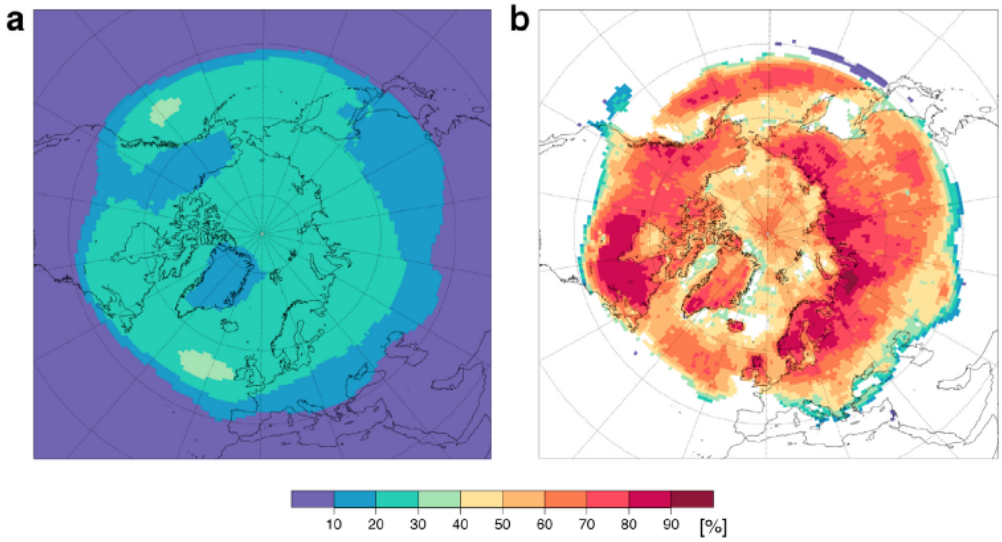

Figure 2.5: Blocking and high-temperature extremes. (a): Relative frequencies of northern hemispheric summer blocking events. (b): Percentage of having a high-temperature extreme and a co-located blocking. Reprinted by permission from Springer Nature: Pfahl and Wernli (2012), © 2012.

tropic advection of low-PV air or cross-isentropic transport of low-PV air along moist ascending air streams. The isentropic advection of low-PV air corresponds to (i) the mechanism introduced by Yamazaki and Itoh (2013), in which blocking is maintained by the absorption of synoptic-scale anticyclones or (ii) the quasi-adiabatic transport of air from lower latitudes, often ahead of extratropical cyclones (e.g. Sanders and Gyakum, 1980; Colucci, 1985). In a Lagrangian framework, Pfahl et al. (2015) and Steinfeld and Pfahl (2019) investigated the influence of diabatic heating, i.e. the cross-isentropic transport of low-PV air along moist ascending airstreams, on the formation and maintenance of blocking. Around 46% of the air masses in northern hemispheric blocks experience latent heating by more than 2 K during the three days prior to their arrival in the block (Fig. 2.6a) and this percentage increases up to 70% when considering a seven-day period (Fig. 2.6b; Pfahl et al., 2015). The contribution of latent heating to the formation and maintenance of blocking is not uniform. Latent heating is more important for the onset than for the maintenance of the block (Pfahl et al., 2015). And in northern hemispheric winter, the contribution of latent heating is much larger for blocks over the oceans than for continental blocks, while in summer also continental blocks are substantially affected by latent heating (Steinfeld and Pfahl, 2019).

Latent heating due to condensation of water vapour is not only restricted to the formation of blocking, it generally influences the upper-level ridge building and amplification (e.g. Pomroy and Thorpe, 2000; Grams et al., 2011). In the midlatitudes, synoptic-scale latent heating occurs within moist ascending air streams from the lower to the upper tro-

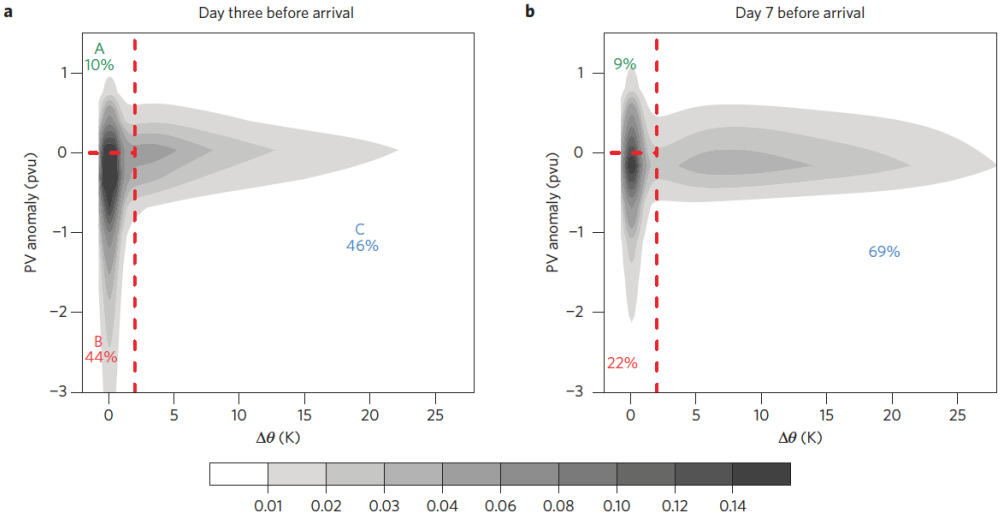

Figure 2.6: Frequency distribution of PV anomaly three (a) and seven (b) days prior to the arrival of the trajectories in the blocking region and maximum diabatic heating during this periods. Colour shading represents frequency densities. The percentages denote the three categories of trajectories defined by the red dashed lines. Reprinted by permission from Springer Nature: Pfahl et al. (2015), © 2015.

posphere, so-called warm conveyor belts (WCBs) (Green et al., 1966; Harrold, 1973; Browning et al., 1973). The outflow of the WCB produces negative PV anomalies at the level of the midlatitude jetstream (cf. Fig. 2.3 and Eq. 2.8) and is therefore a key process for upper-level ridge building (Madonna et al., 2014).

Recently, Quinting and Reeder (2017) analysed trajectories reaching upper-tropospheric anticyclones during heat wave events in southeastern Australia. They emphasised the influence of cloud-diabatic processes over a baroclinic zone to the south of the Australian continent on the formation of upper-tropospheric anticyclones. Hence, diabatic heating in ascending air streams, and therefore the cross-isentropic transport of low-PV air from the lower to the upper troposphere is also crucial for ridge building in connection to heat waves.

2.2.4 Evolution of lower-tropospheric high temperatures

Until now, it has been shown how Rossby wave packets and persistent upper-tropospheric anticyclones are associated with heat waves at the surface. But this does not yet explain, how this leads to high temperatures *near the surface* during heat waves. Therefore, a theoretical derivation of possible processes leading to temperature changes is presented first[2], followed by a literature review on the evolution of near surface temperatures during heat waves.

[2]the derivation follows Carlson (1994)

The first law of thermodynamics relates temperature and pressure change and is, for adiabatic processes (i.e. no exchange of heat with the environment, dq=0), given as:

$$dq = 0 = c_p dT - \frac{1}{\rho} dp, \tag{2.9}$$

where c_p is the specific heat of dry air at constant pressure ($c_p = 1004\,\mathrm{J\,kg^{-1}\,K^{-1}}$), ρ the density and dT and dp the differential of temperature and pressure, respectively. Integrating Eq. 2.9 from p to p_0 and using the ideal gas law yields the Poisson equation:

$$\left(\frac{p}{p_0}\right)^{R_d/c_p} = \frac{T(p)}{T(p_0)}, \tag{2.10}$$

where R_d is the specific gas constant for dry air (R_d = 287 J kg^{-1} K^{-1}). p_0 is set to 1000 hPa and T(p_0) is defined as the potential temperature (θ), i.e. the temperature of an air parcel that is reached when compressing or expanding adiabatically to 1000 hPa. Hence, the relation for temperature is

$$T = \theta \left(\frac{p}{p_0}\right)^{\kappa}, \tag{2.11}$$

where $\kappa = R_d/c_p$. Calculating the material derivative of Eq. 2.11 yields:

$$\frac{dT}{dt} = \underbrace{\frac{d\theta}{dt}\left(\frac{p}{p_0}\right)^{\kappa}}_{A} + \underbrace{\frac{T\kappa\omega}{p}}_{B}, \tag{2.12}$$

where ω is the vertical motion ($\omega = \frac{dp}{dt}$, cf. Holton and Hakim, 2013). Eq. 2.12 is the Lagrangian temperature tendency equation, i.e. following the motion of an air parcel, and relates temperature changes to diabatic processes (term A) and adiabatic processes, i.e. vertical motion (term B). Adiabatic processes do not exchange energy with the environment and the potential temperature change is zero, whereas diabatic processes exchange energy with the environment. Possible examples of diabatic processes are, amongst others, radiative heating/cooling, surface fluxes or latent heat release.

The temperature tendency equation can also be solved in an Eulerian approach, meaning that the processes are calculated at a fixed location. The equation for that perspective can be achieved by means of the Eulerian decomposition:

$$\frac{dT}{dt} = \frac{\partial T}{\partial t} + \vec{v} \cdot \vec{\nabla} T \tag{2.13}$$

By combining Eqs. 2.12 and 2.13 and rearranging, the Eulerian temperature tendency equation reads:

$$\frac{\partial T}{\partial t} = -\vec{v} \cdot \vec{\nabla} T + \frac{d\theta}{dt} \left(\frac{p}{p_0} \right)^{\kappa} + \frac{T \kappa \omega}{p} \tag{2.14}$$

The term on the left side of Eq. 2.14 is the local time derivative of temperature and the first term on the right side is temperature advection.

After the theoretical derivation of physical processes contributing to temperature changes, it is now discussed what physical processes is relevant for the development of high near-surface temperatures during heat waves. As shown in section 2.2.3, blocking anticyclones are often associated with surface heat waves. The persistence of these anticyclones is relevant for the intensity of the heat wave, because highest temperatures often occur at a later stage of the heat wave (Kyselý, 2008). Furthermore, the spatial distance between the anticyclone and the heat wave also determines which process is most important for the development of high temperatures. Subsidence and radiative forcing typically dominates in the vicinity of the anticyclone, whereas advection of warm air masses become more relevant when the anticyclone is spatially shifted from the center of the heat wave (Chang and Wallace, 1987; Pfahl and Wernli, 2012; Pfahl, 2014; Sousa et al., 2018; Woollings et al., 2018).

Warm air mass advection is often mentioned as an important reason of high temperatures near the surface. In that sense, high pressure systems induce a windflow from hot and dry areas towards the heat wave region (Fink et al., 2004; Cassou et al., 2005; Hudson et al., 2011; Pezza et al., 2012; Marshall et al., 2014; Miralles et al., 2014; Boschat et al., 2015; Perkins, 2015; Schumacher et al., 2019). In a comprehensive study, Sousa et al. (2018) quantified the contribution of advection, vertical motion and diabatic processes to high near surface temperatures for heat waves in an Eulerian approach (cf. Eq. 2.14). Figure 2.7 depicts the relevant processes for Central European heat waves and shows that diabatic heating due to enhanced short-wave radiative fluxes is the most important driver, followed by horizontal advection at the edge of the ridge, while subsidence is less relevant.

Studying temperature extremes with Lagrangian trajectories gives insight into source regions, typical transport patterns, and physical processes within the air masses (Black et al., 2004; Bieli et al., 2015; Santos et al., 2015; Quinting and Reeder, 2017). Bieli

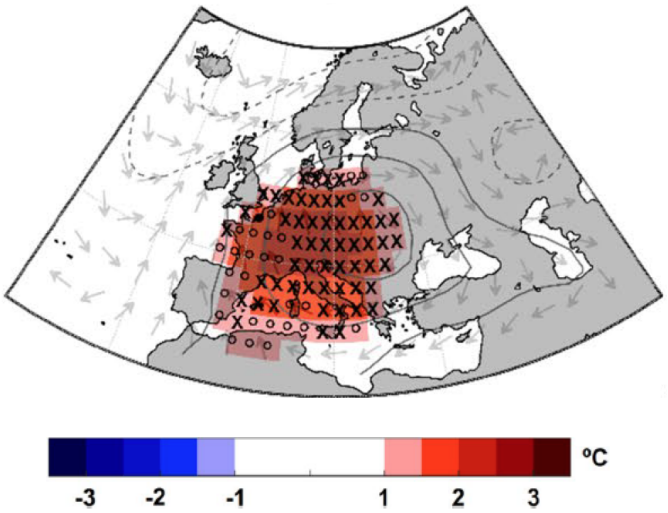

Figure 2.7: Mechanisms leading to high near surface (850-1000 hPa) temperatures during heat waves in Central Europe. Symbols indicate the highest contribution of horizontal advection (○), vertical motion (●) and diabatic processes (X) to temperature anomalies. Contours depict 500-hPa geopotential height anomalies (in 15 dam increments, positive (negative) anomalies solid (dashed)) and grey arrows show horizontal wind direction at 850 hPa. Reprinted by permission from Springer Nature: Sousa et al. (2018), © 2018.

et al. (2015) focused on high and low temperature extremes in three European regions, regardless of their duration, and showed that high temperature events are generally associated with weaker temperature advection (Fig. 2.8) than cold temperature events but they experience strong adiabatic warming by subsidence and enhanced surface radiation and fluxes. Seven days before trajectories enter the heat wave area in Central Europe, some are located in the far north near Greenland (Fig. 2.8). For these trajectories, temperature advection can not be a main contributor to high temperatures. Therefore, processes changing the property of the air mass leading to heat waves are of primary importance. Santos et al. (2015) studied temperature extremes occurring in different seasons over the Iberian Peninsula, noting the importance of the Iberian heat low in summer and the significant contribution of air parcel descent, radiative cooling in the free atmosphere and near-surface warming. Lee and Grotjahn (2016) employed backward trajectories and showed that adiabatic heating and horizontal advection were the main factors in determining the anomalous high temperatures in the lower troposphere above California. A study focusing on heat waves in southeastern Australia emphasized the role of adiabatic compression and deemphasized the role of local surface fluxes (Quinting and Reeder, 2017).

In summary, temperature advection is often mentioned as an important process that leads to high near-surface temperatures during heat waves, especially in studies applying Eulerian approaches. Trajectory-based studies, on the other hand, emphasise subsidence

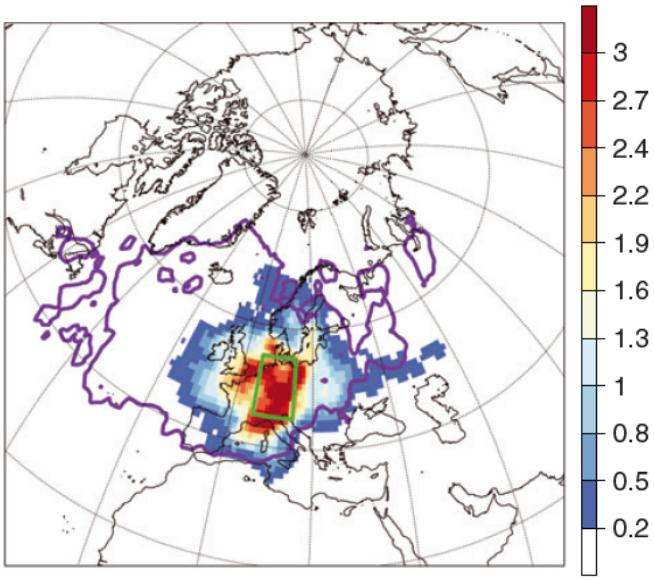

Figure 2.8: Trajectory densities (amount of trajectories per 1000 km^2) four days prior to high temperature extremes in Central Europe (green box), the purple contourline denotes a density level of 0.2 seven days prior to hot extremes. Figure taken from Bieli et al. (2015). © 2015 John Wiley and Sons.

and increased surface sensible heat fluxes. It is therefore not entirely clear at present which process is most relevant.

2.2.5 Land-atmospheric feedbacks

In the planetary boundary layer (PBL), the air interacts with the surface by means of evapotranspiration (e.g. evapotranspiration from land, including plant transpiration and soil evaporation) and surface sensible/latent heat fluxes (Seneviratne et al., 2010). The air-surface interaction is determined by land energy and water balances and both are connected via evapotranspiration, which is highly sensitive to soil moisture content (Seneviratne et al., 2010). Soil moisture is defined as the amount of water in the unsaturated soil zone with respect to a predefined soil volume (Hillel, 1998; Seneviratne et al., 2010). During periods of high soil moisture content, evapotranspiration is high and latent heat fluxes exceed surface sensible heat fluxes. However, dry soil periods, which are more typical during heat waves, are characterised by a decrease of evaporation and therefore by an increase in sensible heat fluxes, which in turn leads to a temperature increase (Seneviratne et al., 2010; Alexander, 2011).

Observational studies have shown that extreme temperatures during heat waves in southeastern Europe are strongly associated with a low soil and vegetation moisture content (Hirschi et al., 2011) and model studies confirm this relation also for other parts in Europe (Fischer et al., 2007). As an example, a reduction of 100 mm in soil mois-

ture increase maximum temperatures by up to 1.6 °C (Whan et al., 2015). Hence, land-atmospheric feedbacks are relevant during heat waves and can further amplify extreme temperaures.

Figure 2.9 shows a conceptual model of land-atmosphere interactions based on Miralles et al. (2014). During heat waves, soils are progressively desiccated and the PBL is steadily heated by surface sensible heat fluxes. In addition, warm air entrainment from aloft leads to a progressive build up of high temperatures in the PBL and an increase of the PBL height (Miralles et al., 2014).

Since soil moisture is a slowly varying meteorological variable on the time scale of weeks to months (Shukla and Mintz, 1982; Huang and van den Dool, 1993; D'Andrea et al., 2006), it may be a useful predictor for seasonal predictions. Indeed, various studies have shown that a precipitation deficit, and therefore reduced soil moisture, in the months before a heat wave increases the probability of this event (Della-Marta et al., 2007; Vautard et al., 2007; Hirschi et al., 2011). This relation is particularly robust for southern Europe, where dry winter and spring seasons are typically followed by an increased frequency of hot days (Quesada et al., 2012). In contrast, when winter and spring season is humid, the frequency of hot days is reduced event when circulation patterns conducive to heat waves, e.g. blockings, occur (Quesada et al., 2012).

2.3 Predictability and predictive skill of heat waves

Before discussing the predictability of heat waves, the two important terms *predictability* and *predictive skill* are discussed at first. The term *predictability* denotes "the extent to which future states of a system may be predicted based on knowledge of current and past states of the system" (American Meteorological Society, 2012). *Predictive skill*, on the other hand, quantifies the ability of a model to predict a certain meteorological variable (Robinson et al., 2002; Wang et al., 2018) using quantitative measures of forecast ability (Wilks, 2011).

In 2010, western Russia was affected by a heat wave and this event was associated with a persistent block (Matsueda, 2011). Although the block was well predicted up to 9 days lead time, the persistence of the block during the hottest period of the heat wave was underestimated. And this in turn led to underestimated near-surface temperatures during the heat wave. The reduced predictability during this period was due to uncertainties of the upstream trough (Matsueda, 2011; Quandt et al., 2017). Other studies, focusing more generally on the predictability of blocking, point towards the reduced predictability during regime transitions, i.e. from a zonal to a meridional flow (Tibaldi and Molteni, 1990; Pelly and Hoskins, 2006). In addition, the persistence of blocks in Europe is underesti-

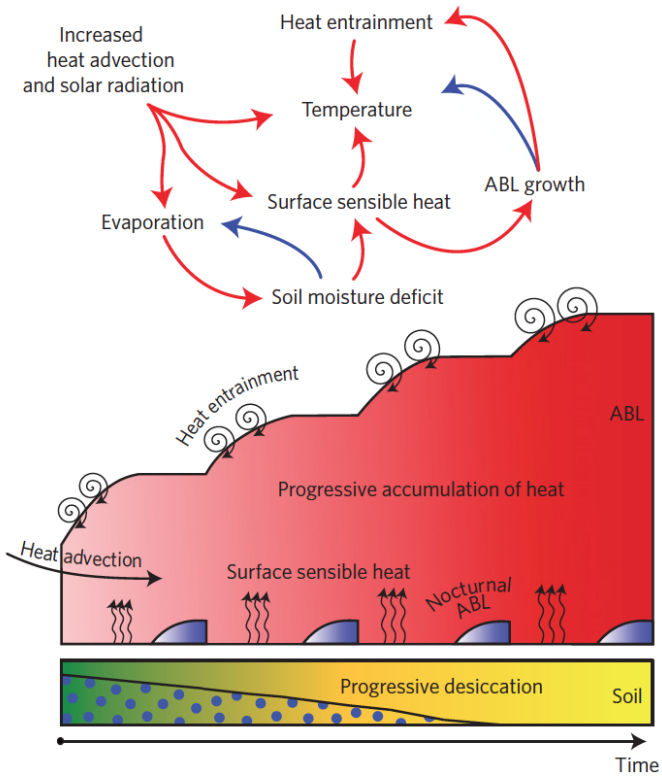

Figure 2.9: Schematic of land-atmosphere interactions during heat waves (ABL denotes atmospheric boundary layer). Red (blue) arrows indicate positive (negative) correlation. Reprinted by permission from Springer Nature: Miralles et al. (2014), © 2014.

mated since models tend to return too fast to the zonal flow (Ferranti et al., 2015).

De Perez et al. (2018) verified forecasts of high near-surface temperature extremes globally and they show predictive skill up to 10 days in advance in large parts of eastern Europe, middle east, most of Russia and USA/Canada. Focusing more regionally on Europe, models possess some skill to forecast heat waves in a two-week lead time, however, intensity, onset and decay of the events remain challenging (Lavayasse et al., 2018). Underestimations of extreme temperatures can be attributed to errors in the coupling between soil moisture and near-surface temperature (Ford et al., 2018). The seasonal forecast from the European Centre for Medium-Range Weather Forecasts (ECMWF) of the 2003 heat wave in Europe was improved due to better interactions between the dry soil and local circulation patterns as well as changes in the convection scheme by increasing convective inhibition, and hereby reducing precipitation (Weisheimer et al., 2011).

Magnusson et al. (2015) evaluated monthly to short-term operational ECWMF ensemble forecasts of the 2015 heat wave in Europe. Figure 2.10 illustrates ensemble forecasts of 2-m temperature for Paris valid on 1 July 2015 12 UTC in comparison with the model climate. The model climate is constructed of 9 consecutive re-forecasts, covering a 5-week period centred around the initialisation time of the actual ensemble forecast

(Owens and Hewson, 2018). Re-forecasts are initialised on Monday and Thursday and calculated for the last 20 years with 11 ensemble members, and therefore, the model climate consists of 1980 re-forecasts (20 years x 9 runs x 11 members). The monthly forecast renders no added value since it simply resembles model climatology (Fig. 2.10). Forecasts initialised on Monday 22 June, i.e. 9 days prior to the event, already hint at higher temperatures, however, some members still predict lower temperatures. Three days prior to the heat wave, on 27 June, the ensemble is more certain, albeit underestimating observed temperature of around 36 °C in Paris. The underestimation of maximum temperatures occurred also during the period 07 May to 12 August 2018 (Fig. 2.11), when parts of Europe were affected by several heat waves (Magnusson et al., 2018). In addition, minimum temperatures were overestimated in the same period (Fig. 2.11). The underestimation of the diurnal cycle strongly affects forecasts of near-surface variables, like temperature, humidity and wind. ECMWF has launched a project on this topic and preliminary results on the underestimation of near-surface temperature indicate an insufficient temperature gradient in the lowest 200 m, as well as incorrect vertical mixing and entrainment at the top of the planetary boundary layer, with the latter tending to affect near-surface humidity (Haiden et al., 2018).

Overall, current forecasting models are useful for heat wave predictions, however, uncertainties remain especially with respect to onset, duration, decay and intensity. In addition, it seems that current ECMWF ensemble forecast often underestimate observed 2-m temperatures.

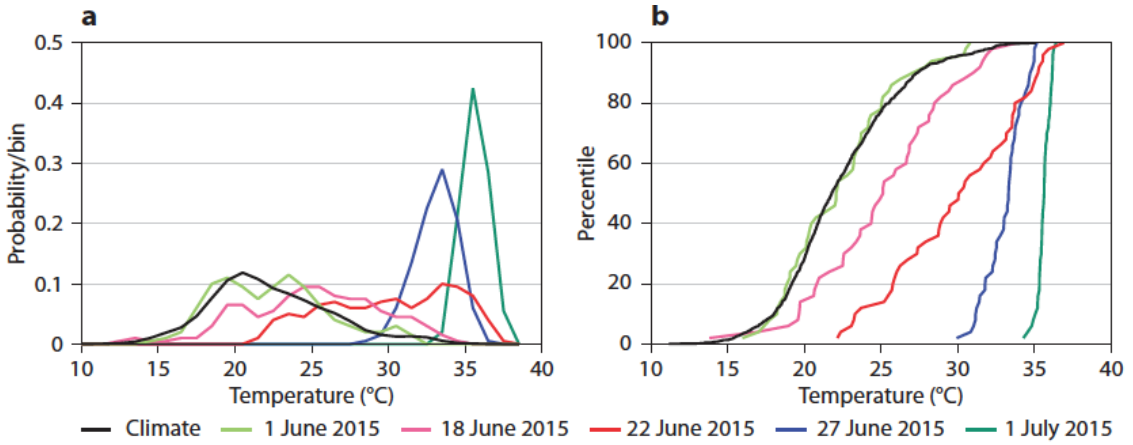

Figure 2.10: Ensemble 2-m temperature forecasts for Paris, valid on 1 July 2015 (12 UTC). (a): Probability density functions of ensemble members, the different colours indicate the initialisation dates (always at 00 UTC), the black line denotes the model climate. (b): The same as (a), except that a cumulative density function is shown. Figure taken from Magnusson et al. (2015).

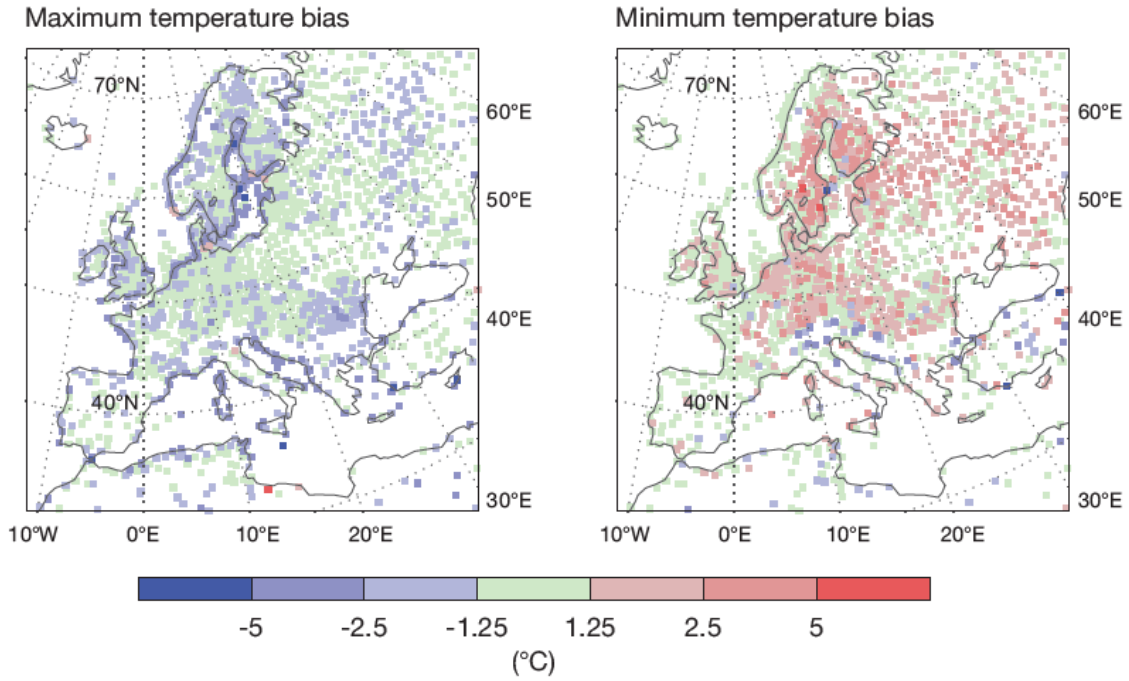

Figure 2.11: Maximum and minimum temperature biases for 2-day forecasts between 07 May and 12 August 2018. Temperatures are verified against SYNOP stations. Red (blue) colours indicate too warm (cold) forecasts. Figure taken from Magnusson et al. (2018).

Chapter 3

Research questions

The previous chapter has reviewed the various processes leading to heat waves and the predictability and predictive skill of these events. It has been shown that heat waves are relevant due to their various impacts, but that especially onset, decay and magnitude of heat waves are still not well understood. As outlined in the Introduction, the thesis follows three main research aims and each aim is decomposed into specific research questions. This chapter motivates and poses these research questions[1].

A diversity of studies exists on the subject of heat waves and the role of soil moisture anomalies on seasonal to climate timescales, but fewer studies have investigated the (thermo-)dynamic development and predictability of heat waves (sections 2.2 and 2.3). Heat waves are often associated with the development of ridging or blocking in the upper-level flow, several days prior to the events, which can be related to Rossby wave dynamics (subsection 2.2.2). Without these large-scale precursors, a heat wave is unlikely to occur, even in the presence of already-desiccated expanses of soil. Under similar large-scale ridging characteristics persisting for 1–3 days prior to peak temperatures, synoptic and mesoscale boundary layer processes will be more important in determining the exact value of the maximum temperature at a weather station. In late summer and early autumn 2016, central, western and southwestern Europe was affected by an unusually late heat wave. Since this heat wave occurred very late in the year, it is interesting to understand which planetary- and synoptic- to meso-scale processes contributed to this event. The aim of Chapter 5 is to shed light on these processes. This case study therefore serves as a good starting point of the thesis to investigate the main research aim A. The path of the Rossby wave packets can be traced back using a diagnostic technique proposed by Fragkoulidis et al. (2018) and the role of the synoptic- to meso-scale processes – that is, horizontal temperature advection, adiabatic compression by subsidence, and heat fluxes – are in-

[1]Research questions are consecutively numbered according to the main research aim. For example, **A1** denotes the first research question of the main research aim **A**.

vestigated with trajectories. These are all terms of the Eulerian form of the temperature tendency equation (Carlson, 1994), as outlined the literature review (subsection 2.2.4). In addition, the predictive skill of ECMWF ensemble forecasts is quantified for the heat wave. More specifically, following research questions are addressed for this case study:

A1 How intense is the heat wave?

A2 How can high temperatures during the heat wave be related to upper-tropospheric Rossby wave packets?

A3 Which physical processes lead to high temperatures during the event?

C1 How accurate are the predictions for this event?[2]

As outlined in the literature review, it is not yet clear which of the three processes – viz. horizontal advection, vertical motion and diabatic processes – contributes most to high near-surface temperatures during heat waves. Many studies assert that high near-surface temperatures are the result of temperature advection and dry soils, while the role of subsidence is less mentioned. Furthermore, it is not yet discussed in the literature, how these processes evolve during the life cycle of a heat wave. The aim of Chapter 6 is to quantify, in a climatological analysis, which process dominates in establishing near-surface high temperature extremes across different European climates. To this end, a heat wave climatology is derived and air masses associated with heat waves in Europe are traced backwards in time, similar to Bieli et al. (2015). In contrast to Bieli et al. (2015), the focus is on heat waves with a minimum duration of three days in six European regions, including regions that were not yet studied with Lagrangian trajectories so far, i.e. western Russia and Scandinavia. Therefore, Chapter 6 addresses following research questions:

A4 How often is Europe affected by a heat wave and how long do these events last?

A5 What synoptic patterns are associated with heat waves?

A6 What are typical source regions, pathways and physical processes along trajectories reaching heat wave areas?

A7 Are heat waves steadily influenced by new air masses or are the air parcels being stalled in the lower troposphere over a longer time period?

[2]Note that predictability and predictive skill of heat waves is studied in Chapters 5 and 8. Therefore, research questions for main research aim C are splitted between these two chapters.

As mentioned earlier in this chapter and in the literature review, heat waves in the mid-latitudes are typically co-located with atmospheric blocking or intense subtropical ridges. Both blockings and intense ridges are associated with anticyclonic flow anomalies in the upper troposphere, and therefore with low PV air masses. These low-PV air masses are substantially influenced by upstream latent heating (subsection 2.2.3). Recent climatological studies on blocking tend to be dominated by oceanic blocking (Pfahl et al., 2015; Steinfeld and Pfahl, 2019), but heat waves are typically associated with summertime continental blocks (Röthlisberger et al., 2016; Brunner et al., 2018; Chan et al., 2019), which are typically weaker than wintertime oceanic blocks (Pfahl and Wernli, 2012). Also, the influence of latent heating on the formation of continental blocking may differ. Quinting and Reeder (2017) analysed trajectories reaching the lower and upper troposphere during heat waves over southeastern Australia. However, Quinting and Reeder (2017) did not analyse the life cycle of upper-tropospheric anticyclones, i.e. whether the role of diabatic heating differs between the formation and maintenance of these anticyclones. Since Quinting and Reeder (2017) focused on Australia and no similar study exists for Europe, the aim of Chapter 7 is therefore to analyse the role of diabatic heating for the formation and maintenance of upper-tropospheric anticyclones associated with heat waves in different parts of Europe. An impact-oriented perspective is applied, meaning that a particularly impact-related type of upper-tropospheric flow anomalies is studied. The following questions are addressed:

B1 What are typical source regions of low-PV air masses that constitute the upper-tropospheric anticyclones associated with European summer heat waves?

B2 Are there inter-regional differences in the contribution of diabatic heating to the formation of these anticyclones?

B3 Where and in which synoptic environment does the diabatic heating occur in airflows entering the anticyclones?

B4 Are there differences in the relevance of diabatic heating during the formation and maintenance of the anticyclones?

The last chapter analyses the predictability and predictive skill of a long-lasting heat wave in 2018 affecting Central Europe. During this year, the author had access to operational ECMWF ensemble forecasts with very high vertical resolution. This allows the calculation of trajectories in the forecast space. This is normally not possible, as the forecasts are usually not made available for research at this high vertical resolution due to lim-

ited storage capacity[3]. A key hypothesis is that forecast errors on different temporal scales are related to meteorological phenomena on different spatial scales. Prediction errors on a one-week lead time are related to errors in upper-tropospheric dynamics, e.g. phase speed of individual troughs and ridges or amplitude of Rossby wave packets (Teubler and Riemer, 2016; Wirth et al., 2018; Baumgart and Riemer, 2019). Former studies focused on errors in the upper-tropospheric flow, but forecast errors of surface variables, such as 2-m temperature, with three days lead time are thought to be related to processes within the air masses, e.g. subsidence and diabatic temperature changes that are located closer to the heat wave. Chapter 8 addresses this hypothesis by quantifying the predictive skill of 3- and 7-day ECMWF ensemble forecasts. It is investigated why ensemble members over- or underestimate the observed temperature. To this end, a new approach is applied based on a combination of observed trajectories from reanalysis and predicted trajectories from ensemble forecasts. To our knowledge, no such trajectory-based approach has been applied to temperature predictions in association with heat waves before. Specifically, following research questions are addressed:

C2 How accurately does the ECMWF ensemble predict the 2-m temperature during the heat wave?

C3 How can the performance of predictions be related to air mass histories?

[3]Many thanks to Christian Grams and his working group for downloading and granting access to the dataset.

Chapter 4

Data and Methods

This chapter presents the data and most relevant methodologies. All datasets are presented in this Chapter, but, in order to avoid redundancy or breaks in the reading flow, methods that only concern individual chapters are presented at the beginning of each results section and methods applied in more than one chapter are introduced here.

4.1 Data

The most relevant dataset utilised in this thesis is the ERA-Interim reanalysis product of the European Centre for Medium-Range Weather Forecasts (ECMWF, Dee et al., 2011). It is a gridded product and contains, amongst others, global surface data and upper-air parameters and is produced with one consistent data assimilation and forecasting system. The forecasting system is the ECMWF Integrated Forecasting System (IFS), which is fully coupled for atmosphere, land surface and ocean waves. It is based on release Cy31r2, which was operationally used at ECMWF from 12 December 2006 until 05 June 2007 (Berrisford et al., 2011). The reanalysis is generated with 12 h analysis cycles, in which observations from the atmospheric state are compared with prior information from the forecast model, which was initialised from the preceding analysis. As an example for the analysis at 00 UTC, observations between 15 UTC of the previous day and 03 UTC of the present day are taken. The comparison of observations and forecasts from upper-air parameters is based on the 4D-Var data assimilation system that constrains the evolution of the atmospheric state within each analysis cycle with the forecast model. Near-surface parameters, e.g. 2-m temperature and humidity, are assimilated separately by means of an optimal interpolation of observed parameters. Here, a regular 1° latitude-longitude grid for the time steps 00, 06, 12 and 18 UTC during 1979–2016 is used[1]. Only for the

[1]ERA-Interim archive is used from ETH Zurich. Many thanks to Christian Grams for granting access.

case study in Chapter 5, a regular 0.75° latitude-longitude grid is utilised[2].

The predictability of heat waves in Chapters 5 and 8 is analysed with operational ECMWF ensemble forecasts that consist of 50 perturbed and one control forecast (Owens and Hewson, 2018). The initial perturbations are created by means of singular vectors and ensemble of data assimilation, while uncertainties resulting from physical parameterisations or unresolved processes are simulated with the Stochastically Perturbed Parameterisation Tendencies (SPPT) scheme throughout the execution of the forecast. More information on the ensemble generation can be found in Owens and Hewson (2018). Forecasts are initialised twice per day, at 00 and 12 UTC, and run up to 15 days. For the case study in Chapter 5, 2-m temperatures at 0.25° x 0.25° latitude-longitude resolution and at lead times of 1, 2, 3, 5, 7, 10 and 15 days are downloaded. Forecasts are based on release Cy41r1, which was operationally used from 08 March 2016 to 22 November 2016. For the case study in Chapter 8, 500-hPa geopotential height, as well as horizontal and vertical wind, temperature, specific humidity from the lower 63 model levels are utilised at a 1° x 1° latitude-longitude regular grid and for 3 and 7 day lead time[3]. Forecasts for this study are based on release Cy45r1, which was operationally used between 05 June 2018 and 11 June 2019.

Synoptic observations from Bordeaux, Seville and Trier in Chapter 5 are downloaded from the Integrated Surface Database (ISD). The database includes over 35,000 stations from the whole globe and consists of hourly synoptic observations.

4.2 Area of study

The focus of this thesis is on different European regions (Fig. 4.1) with the aim to reflect and compare the different climates in Europe. Most of the regions are defined following Bieli et al. (2015) and Santos et al. (2015). The other regions are chosen in order to complement the different European climates. The position of the easternmost region is motivated by the position of extreme heat wave in 2010 over western Russia, e.g. Grumm (2011).

The climatological studies in Chapters 6 and 7 use the regions from Fig. 4.1, while the case studies only use a subset of the regions or a larger region, where heat waves were most intense. Chapter 8 focuses on Central Europe and Chapter 5 on regions containing Central, western and southwestern Europe.

[2]This study was performed before access to ERA-Interim archive from Christian Grams was possible.

[3]Operationally, 91 model levels are available, but due to limited storage capacities, lower 63 model levels are downloaded. Operational ensemble forecasts on model levels are downloaded by the Large-scale dynamics and Predictability group at KIT. Many thanks to Christian Grams for granting access.

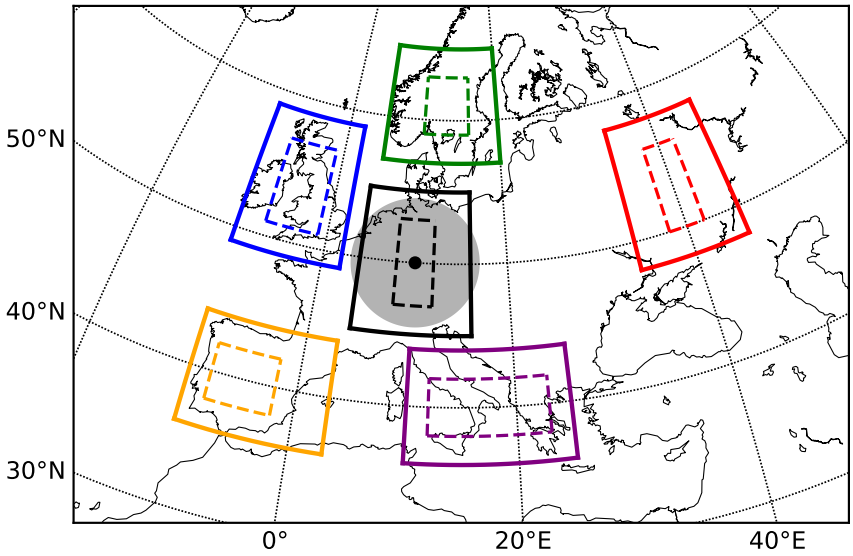

Figure 4.1: Studied regions in Europe: Scandinavia (green; solid box: 57°N-65°N, 5°E-20°E; dashed box: 59°N-63°N, 10°E-16°E); western Russia (red; solid box: 48°N-58°N, 34°E-46°E; dashed box: 50°N-56°N, 38°E-42°E); Greece/ Italy (purple; solid box: 36°N-44°N, 10°E-25°E, dashed box: 38°N-42°N, 12°E-23°E); Iberian Peninsula (orange; solid box: 36°N-44°N, 10°W-3°E; dashed box: 38°N-42°N, 8°W-2°W); British Isles (blue; solid box: 49°N-59°N, 10°W-2°E; dashed box: 51°N-57°N, 8°W-1°W) and Central Europe (black; solid box: 45°N-55°N, 4°E-16°E, dashed box: 47°N-53°N, 8°E-12°E). The solid lines represent the regions employed for the backward trajectories, the dashed lines are the borders for the forward trajectories, for more details see section 6.1. The grey circle (exemplarily shown for Central Europe) with a radius of 500 km is used for the calculation of the residence time, for more details see section 6.1. Figure taken from Zschenderlein et al. (2019).

4.3 Heat wave definition

The derivation of a heat wave climatology that is used in Chapters 6 and 7 is performed with the HWMId (cf. section 2.1). Heat waves are identified across different European regions (Fig. 4.1). According to Russo et al. (2015), a heat wave is defined as a period of at least three consecutive days with a daily maximum temperature above a threshold. This threshold is defined as the 90$^{\text{th}}$ percentile of the daily maximum of 00, 06, 12 and 18 UTC temperatures at 2 m height within a centred 31-day window in the years 1979–2016. This approach identifies heat waves in all seasons. As an example to calculate the 90$^{\text{th}}$ percentile on 16 August we consider the grid point daily maximum temperature values between 01 and 31 August of the 38 years between 1979–2016.

The second part of the HWMId filters the stronger heat waves that usually occur during summer, i.e. June, July and August in the Northern Hemisphere. The daily heat wave magnitude M_d is defined as:

$$M_d = \begin{cases} \dfrac{T_d - T_{38y25p}}{T_{38y75p} - T_{38y25p}} & \text{if} \quad T_d > T_{38y25p} \\ 0 \quad \text{if} \quad T_d \leq T_{38y25p} \end{cases} \tag{4.1}$$

with T_d being the maximum temperature of 00, 06, 12 and 18 UTC 2-m temperature and T_{38y75p} (T_{38y25p}) the 75$^{\text{th}}$ (25$^{\text{th}}$) percentile of annual maximum temperatures between 1979 and 2016. The criterion $T_d > T_{38y25p}$ identifies heat waves in the warmest time of the year, usually during June, July and August (JJA). Hence, all heat waves identified with $M_d > 0$ occur during the summer season. Then, very small areas of high temperature extremes are excluded, because heat waves are typically a synoptic-scale phenomenon (Stefanon et al., 2012). As a consequence, it is defined that at least 5% of the pre-defined region (Fig. 4.1) should exceed $M_d > 0$ per day to be identified as a heat wave. As a result of the three identification steps, a heat wave list is deduced for every region that serves as the heat wave climatology in Chapters 6 and 7.

4.4 Trajectories

This section presents at first some general aspects on trajectories, following Hantel (2013). In the second part, the calculation of trajectories in the Lagrangian analysis tool LAGRANTO is explained.

4.4.1 General aspects

The velocity $\vec{v}$ is defined as the time derivative of the position vector $\vec{x}$:

$$\frac{d\vec{x}(t)}{dt} = \vec{v}(t). \tag{4.2}$$

This is only useful when following an individual air parcel, i.e. in a Lagrangian perspective. The Eulerian perspective, in contrast, views the velocity as the velocity of *all* air parcels ($\vec{v} = \vec{v}(\vec{x})$). When applying the Lagrangian perspective to all air parcels, the velocity becomes

$$\vec{v} = \vec{v}(\vec{a}, t), \tag{4.3}$$

where $\vec{a}$ is the position vector of an air parcel at an initial time t_0, i.e. $\vec{a} = \vec{x}(t_0)$. And when applying the Eulerian perspective to all time steps, velocity reads $\vec{v} = \vec{v}(\vec{x}, t)$.

A trajectory is defined as the pathway $\vec{x}(t)$ of an individual air parcel and is always parallel to the velocity field (Fig. 4.2). Hence, integrating Eq. 4.2 yields the trajectory

$$\vec{x}(t) = \vec{x}(0) + \int_{t'=0}^{t'=t} \vec{v}(t')dt' \tag{4.4}$$

and contains information of the velocity field at the location of the air parcel for all timesteps.

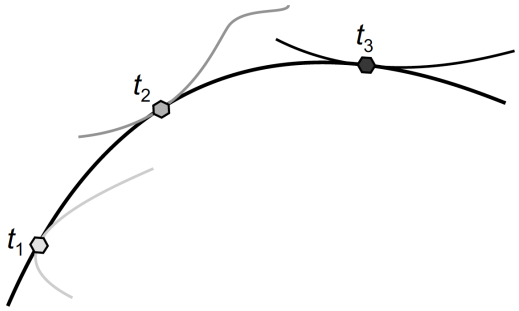

Figure 4.2: Schematic of a trajectory (black solid line). The trajectory is always tangential to the velocity field (grey lines) at the time steps t_1, t_2 and t_3. Reprinted by permission from Springer Nature: Hantel (2013), © 2013.

During the next chapters, trajectories are extensively analysed and interpreted. In order to be consistent throughout the whole thesis, the following terminology is used. The starting point is the initialisation point of a trajectory (black circle in Fig. 4.3). After the initialisation, forward or backward trajectories can be calculated (red and blue arrow in Fig. 4.3). The endpoint of a backward trajectory is regarded as the source or origin, whereas the endpoint of a forward trajectory is considered as the target.

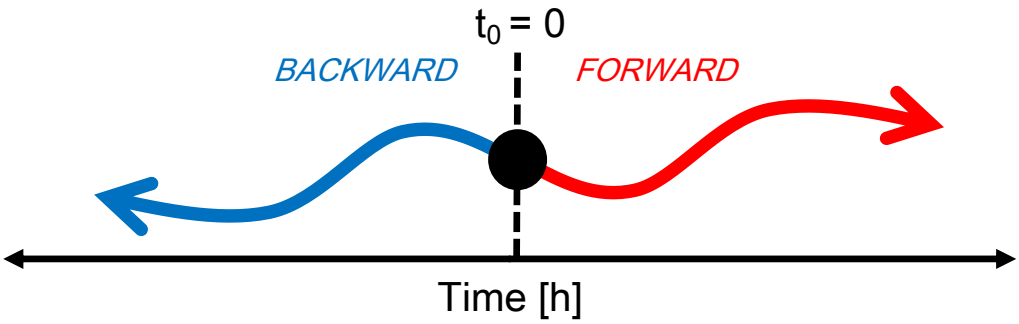

Figure 4.3: Schematic of forward and backward trajectories. The black circle represents the initialisation/starting point of the trajectory. For more information, see text.

4.4.2 Lagrangian analysis tool (LAGRANTO)

All trajectories are calculated with the Lagrangian analysis tool LAGRANTO, which is originally developed by Wernli and Davies (1997) and later updated by Sprenger and Wernli (2015). The pathway of the trajectory is iteratively calculated. Initially, starting at a fixed position at time t and using wind $\vec{u}(\vec{x}, t)$ at this position, the first iteration to calculate the new position is defined as

$$\vec{x}^* = \vec{x} + \vec{u}(\vec{x}, t) \cdot \Delta t \tag{4.5}$$

with Δt being the time step. The next iteration uses the average of the wind at the starting position $\vec{u}(\vec{x}, t)$ and the wind at the estimated ending position $\vec{x}^*$:

$$\vec{u}^* = 0.5(\vec{u}(\vec{x}, t) + \vec{u}(\vec{x}^*, t + \Delta t)) \tag{4.6}$$

and the next iteration of the new position is:

$$\vec{x}^{**} = \vec{x} + \vec{u}^* \cdot \Delta t \tag{4.7}$$

Three iterations are applied in LAGRANTO to calculate the new position of the trajectory and the time step Δt is typically 1/12 of the input data. For example, in ERA-Interim the time step Δt is 30 min, because the reanalysis has a temporal resolution of 6 h.

Calculating trajectories with LAGRANTO typically consists of three major steps. Firstly, starting points must be defined. They can be defined on a regular latitude-longitude grid, or on an equidistant grid and on certain pressure levels or altitudes above ground level. Secondly, trajectories are calculated and LAGRANTO produces a file with informations about the time since initialisation, geographical coordinates and pressure of the trajectory. In a third step, meteorological variables along the trajectories, e.g. temperature, potential temperature, specific humidity, potential vorticity etc., can be traced. The optional fourth step select trajectories according to the meteorological variable. For example, only trajectories with an absolute value of less than 1 PVU at the starting points can be selected.

LAGRANTO is used for calculating backward trajectories, driven by three-dimensional ERA-Interim wind fields on 60 model levels in Chapters 5, 6, 7 and 8. Forward trajectories, driven by three-dimensional wind fields on 63 model levels, which are based

on ECWMF ensemble forecasts, are also calculated with LAGRANTO in Chapter 8. Details on starting points and the selection of trajectories are introduced at the beginning of each chapter.

4.5 Temperature - potential temperature phase space

When tracing potential temperature and temperature along trajectories, it is possible to explain, whether the temperature change of a trajectory is due to diabatic or adiabatic processes. This is relevant to study the evolution of the near-surface high temperatures during heat waves (cf. subsection 2.2.4 and Eq. 2.12) in Chapters 5 and 6.

In order to distinguish adiabatic and diabatic temperature changes experienced by an air parcel following its motion, a so-called T–θ phase diagram (Figure 4.4) can be used (Bieli et al., 2015). The diagram depicts both the temperature T (y-axis) and the potential temperature θ (x-axis) of an air parcel, and its possible changes. The potential temperature θ is the temperature that an air parcel would attain when moved adiabatically to 1000 hPa. Adiabatic processes are defined as processes that do not change the dry entropy of an air parcel, which implies that the potential temperature is materially conserved following the motion of the parcel and that any changes occur reversibly. Diabatic processes, in contrast, are associated with an exchange of energy between an air parcel and its environment, resulting in an irreversible material rate of change of the potential temperature. Examples of diabatic processes include radiative processes, subgrid-scale turbulent fluxes (especially in the boundary layer) and the release of latent heat due to phase changes in clouds. When looking at the illustration in Figure 4.4, the reader should imagine an air parcel located at the origin of the arrows, as marked by the grey circle. Movements in the strictly vertical direction of the T–θ diagram correspond to adiabatic processes, since θ is conserved. By contrast, diabatic processes occur for all non-strictly-vertical displacements of the parcel in the T–θ diagram, with the red (blue) semicircles indicating diabatic heating (diabatic cooling). The parcel may undergo the following changes: increasing T due to subsidence (compression of the air parcel, adiabatic warming), as indicated by the arrow pointing upwards towards the letter 'A'; decreasing T due to lifting (expansion of the air parcel, adiabatic cooling), as indicated by the arrow pointing downwards towards 'C'; increasing θ due to diabatic warming, but simultaneously decreasing T, which can only be explained by lifting and, hence, adiabatic cooling exceeding diabatic heating (quadrant 'B2'); decreasing θ due to diabatic cooling, but simultaneously increasing T, which can only be explained by subsidence and, hence, adiabatic warming exceeding diabatic cooling (quadrant 'D1'); the quadrants 'B1' and 'D2' are associated with diabatic heating and cooling, respectively, but no conclusion can be drawn regarding the vertical

motion.

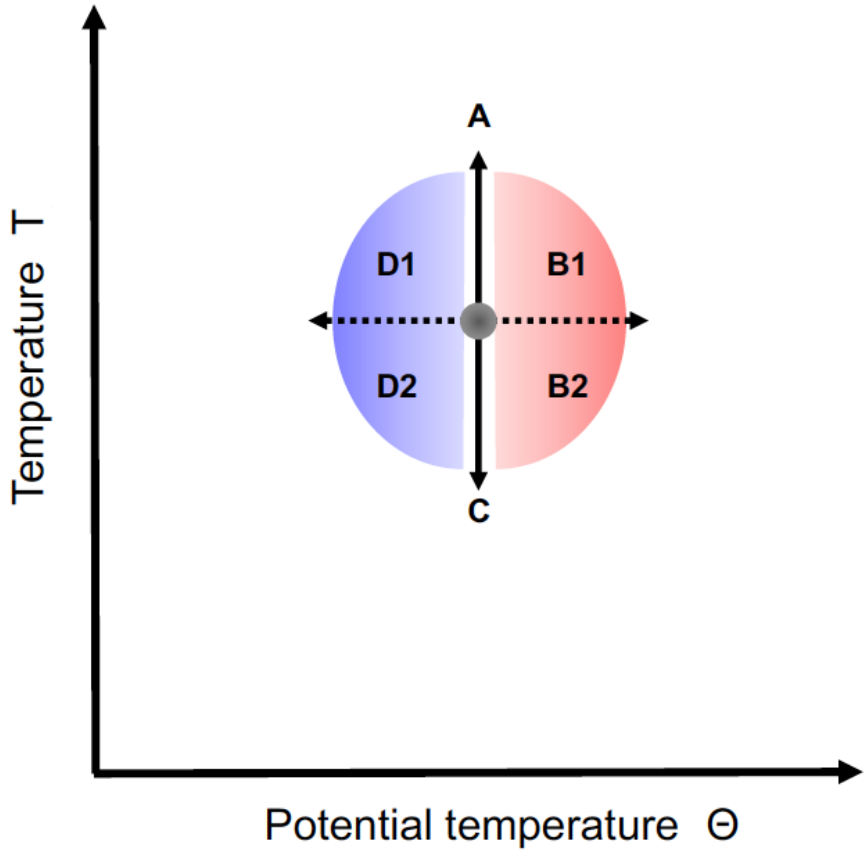

Figure 4.4: T–θ diagram. For more information, see text. Figure taken from Zschenderlein et al. (2018). © The authors and John Wiley & Sons, CC-BY.

Chapter 5

Large-scale Rossby wave and synoptic-scale dynamic analyses of the unusually late 2016 heat wave over Europe

This chapter investigates the large-scale Rossby wave and synoptic-scale dynamic processes leading to the 2016 heat wave in different European regions. Specific methods for this case study are first explained, followed by an overview on the duration and temperature records of the heat wave in section 5.2. Then, section 5.3 quantifies the heat wave magnitude and section 5.4 discusses the synoptic evolution during the heat wave. Large-scale Rossby wave processes are examined in section 5.5 and section 5.6 investigates the development of high temperatures near the surface. This chapter closes with some aspects on the predictive skill of this event.

5.1 Methods

5.1.1 Area of study

The analysis of this event is restricted to parts of central, western and southwestern Europe due to the highest intensity of the heat wave in this regions (grey box in Fig. 5.2b). Bordeaux, Seville and Trier reached record temperatures and are therefore analysed in more detail (see locations of the cities in Fig. 5.1).

5.1.2 Magnitude and duration of the event

In order to quantify the magnitude of the heat wave, the percentile-based HWMId (Russo et al., 2015) is used (cf. section 2.1). In view of the decrease of the climatological temperature towards the end of August and during September (Fig. 5.2a), the reference period is adjusted to calculate the heat index. More specifically, as a climatological reference only annual maximum temperatures between 15 August and 30 September 1981–2010 are considered, in contrast to the full year used in Russo et al. (2015).

The duration of the event is based on the anomaly of the daily 2-m maximum temperature from the climatology, averaged over the area bounded by the grey box in Fig. 5.2b. The climatology encompasses a centred 21-day time window of daily 2-m maximum temperatures, covering the years 1979-2016. Daily maximum temperatures are derived from temperatures at 00, 06, 12 and 18 UTC.

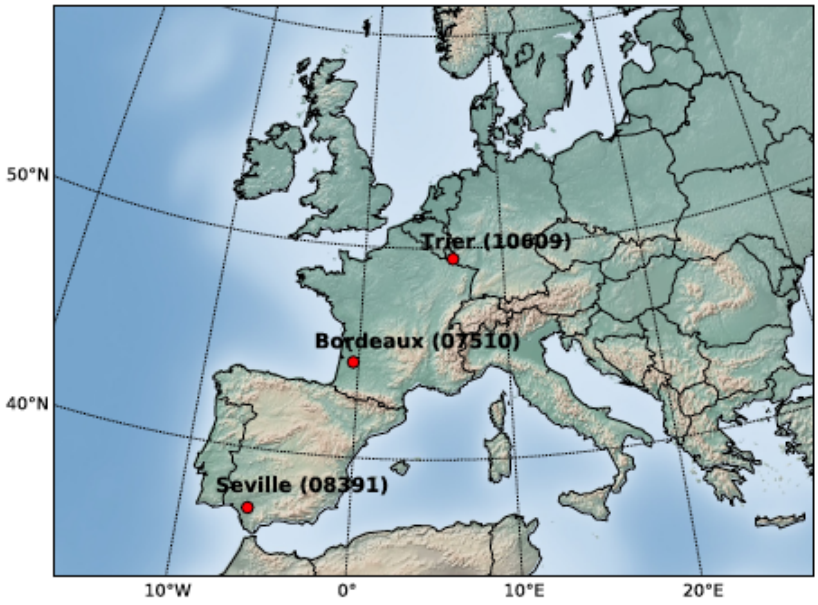

Figure 5.1: Map showing the locations of the weather stations under study: Bordeaux (France), Seville (Spain) and Trier (Germany). Their WMO station numbers are included in parentheses. Figure taken from Zschenderlein et al. (2018). © The authors and John Wiley & Sons Ltd, CC-BY.

5.1.3 Trajectories

In order to study the development of the temperature extremes during the heat wave, 5-day backward trajectories are calculated with LAGRANTO (cf. section 4.4.2), driven by 6-hourly ERA-Interim three-dimensional wind fields. They are started at the nearest

grid points to the three locations, i.e. Bordeaux, Seville and Trier. Vertically, trajectories are initialised in the lower and middle troposphere in 25 hPa increments, provided that temperature anomaly at the respective pressure level exceeds the 95th percentile of the climatology.

The climatology is calculated for each pressure level between 975 and 500 hPa at the respective grid points with a centred 21-day time window, covering the years 1979-2016.

5.1.4 Predictive skill of the heat wave

The predictive skill of this heat wave is investigated following the approach of Magnusson et al. (2015). In a case study for a heat wave affecting Paris (France) in July 2015, Magnusson et al. (2015) compared the distribution of the ECMWF ensemble 2-m temperature forecasts for different lead times (cf. section 2.3). For both the model climate as well as for the various forecast lead times a cumulative distribution function (CDF) is constructed (see Fig. 2.10b).

5.2 Overview of the event

The 2016 late-summer heat wave is remarkable in that it sets the stage for the development of the first-ever reported tropical-like storm in the Bay of Biscay (Maier-Gerber et al., 2017). These authors noted the record-breaking sea surface temperatures (SSTs) in the Bay of Biscay, which were consequences of the calm, sunny and warm weather in the weeks leading up to the 'Biscane' (named as a counterpart to the 'Medicane' – a Mediterranean hurricane) Stephanie on 15 September 2016. Figure 5.2a shows the ERA-Interim-based time series of daily maximum 2-m temperature, averaged between 35°–55°N and 11°W–15°E (the region bounded by the rectangle in Fig. 5.2b) for June to September 2016, in comparison with the daily climatology for 1979–2016. The summer of 2016 is characterised by several short warm periods, especially in June and July. Towards the end of the summer season, a heat wave commences around 23 August and lasts until mid-September. With three peaks occurring around 23 August, 5 September and 13 September, mid-summer temperature levels persist throughout a period over which the climatological temperature exhibits a large decrease (green dashed line in Fig. 5.2a). As a consequence, the temperature anomalies steadily increase.

Based on the HWMId, the largest positive temperature anomalies are observed in Spain and central and western Europe (Fig. 5.2b). Bordeaux, in southwestern France, registers a maximum daily temperature of 37 °C during the first peak on 23 August 2016. The second peak is record-breaking, in particular for southern Spain. Seville measures 44.8 °C on 5 September 2016, which is the highest temperature on record for any Septem-

ber month at this station. The last peak mainly affects central Europe, where, for example, Trier measures 34.2 °C on 13 September 2016, which is also the highest temperature on record for any day in September at this station.

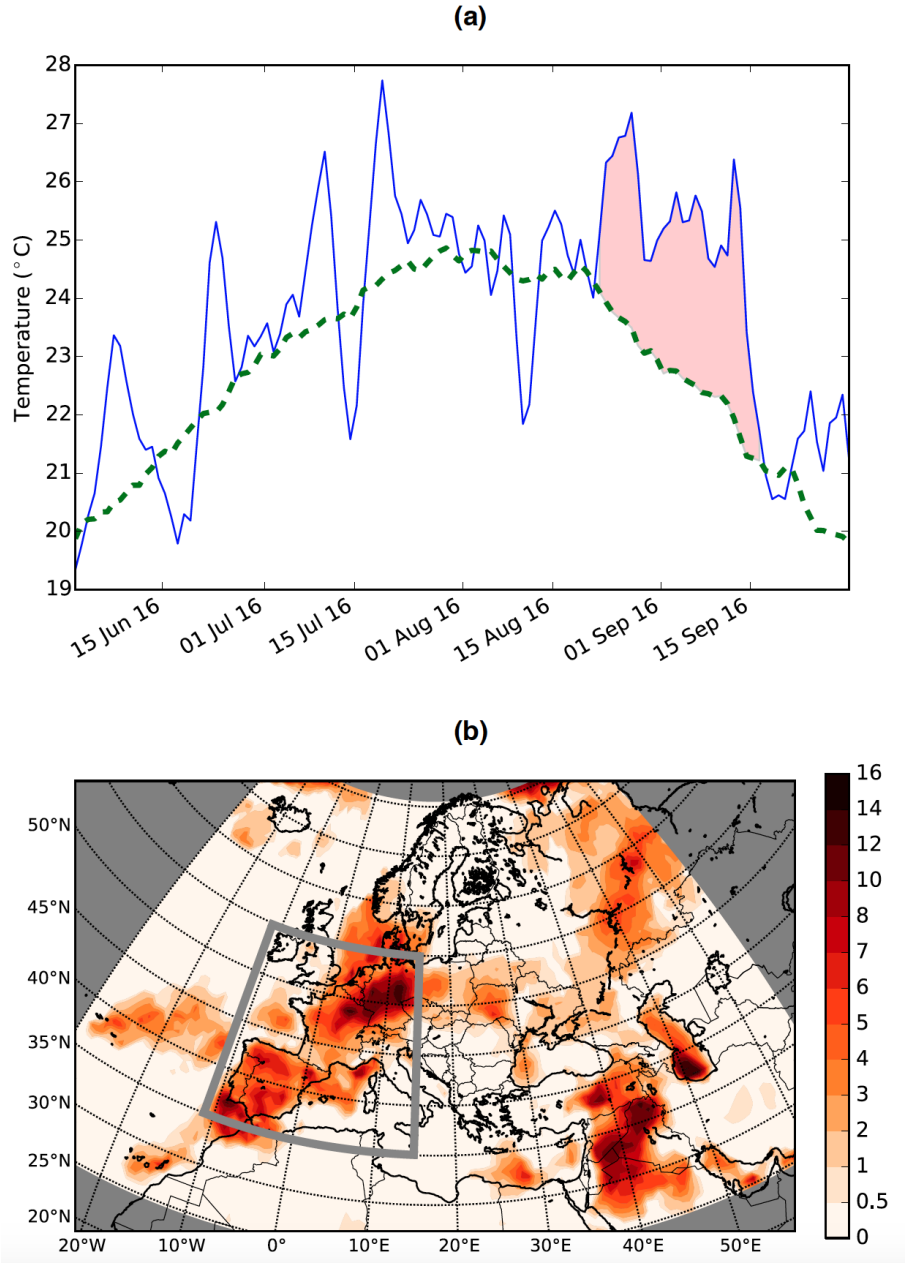

Figure 5.2: Spatio-temporal extent of the late summer heat wave in 2016. (a) Time series of area averaged (35°–55°N, 11°W–15°E; see rectangle in panel (b)) daily maximum 2-m temperature between 1 June and 30 September 2016. The green dashed line shows the daily ERA-Interim climatology for the reference period 1979–2016. The red filled area corresponds to the heat wave from 23 August to 16 September 2016. (b) Accumulated Heat wave Magnitude Index daily (HWMId, Russo et al. (2015)) values for the heat wave period. Figure taken from Zschenderlein et al. (2018). © The authors and John Wiley & Sons Ltd, CC-BY.

5.3 Magnitude of the heat wave

Figure 5.2b shows the HWMId sum for 2-m temperatures for the heat wave period 23 August–16 September. Contrary to the methods of Russo et al. (2015), the index is calculated over both land and ocean – positive values above land surfaces indicate high surface temperatures, whereas positive values above the oceans indicate high SSTs, due to their strong influence on 2-m temperatures. Central and western Europe are particularly affected during the first and last peaks, whereas the second peak is very intense for Spain, thus resulting in the cumulative heat index displayed in Fig. 5.2b. Adjacent waters also show high HWMId values, especially over parts of the Bay of Biscay, the Gulf of Cadiz and the Gulf of Lion, and the North and Baltic Seas. Note that in the North Sea, for the first time since observations began in 1968, the highest SSTs are recorded in September rather than August (BSH, 2016). Compared with the 2003 heat wave in parts of Europe, the spatial extent of the 2016 heat wave is comparable, but the HWMId values are smaller for 2016 (not shown). It should be noted that this could be due to differences in both the magnitudes and the durations of the heat waves. The HWMId index can also be applied to the data for the temperature at 850 hPa. While a similar overall spatial pattern emerged, higher values at 850 hPa occur over the UK and the North Sea, suggesting that the maritime climate of the British Isles diminished the warmth at the surface (not shown).

5.4 Synoptic evolution

In this section, the spatio-temporal evolution of the heat wave is examined from a synoptic perspective. The first peak of the heat wave on 23 August 2016 is associated with an extremely strong 500-hPa ridge that extended from the Iberian Peninsula across central Europe to the southern parts of Scandinavia (Fig. 5.3a). The maximum geopotential height value of approximately 596 gpdam is located near the Pyrenees. As can be inferred from the pink shading in Fig. 5.3a, the highest geopotential height values for the 1979–2016 period are recorded over large parts of west and southwest Europe on this day. The percentile values given for any particular day in Fig. 5.3 are calculated with respect to a centred 21-day window (for 12 UTC only), spanning the years 1979–2016. Eastern France records the highest geopotential height since 1979. Though they are not as extreme as the geopotential height measurements, temperatures at 500 hPa (Fig. 5.3b) are also very high, with values above the 95$^{\text{th}}$ percentile covering much of western Europe. At the western flank of the ridge, extremely high temperatures dominate at 850 hPa (Fig. 5.3c), with values exceeding 22 °C over France. At this time of year, such high temperatures are very unusual poleward of 40°N in western Europe and correspond to the

top 1% of the climatological distribution (red areas in Fig. 5.3c). The upper-level ridge propagates eastwards over the following few days, after which the flow becomes more zonal and the heat wave weakens.

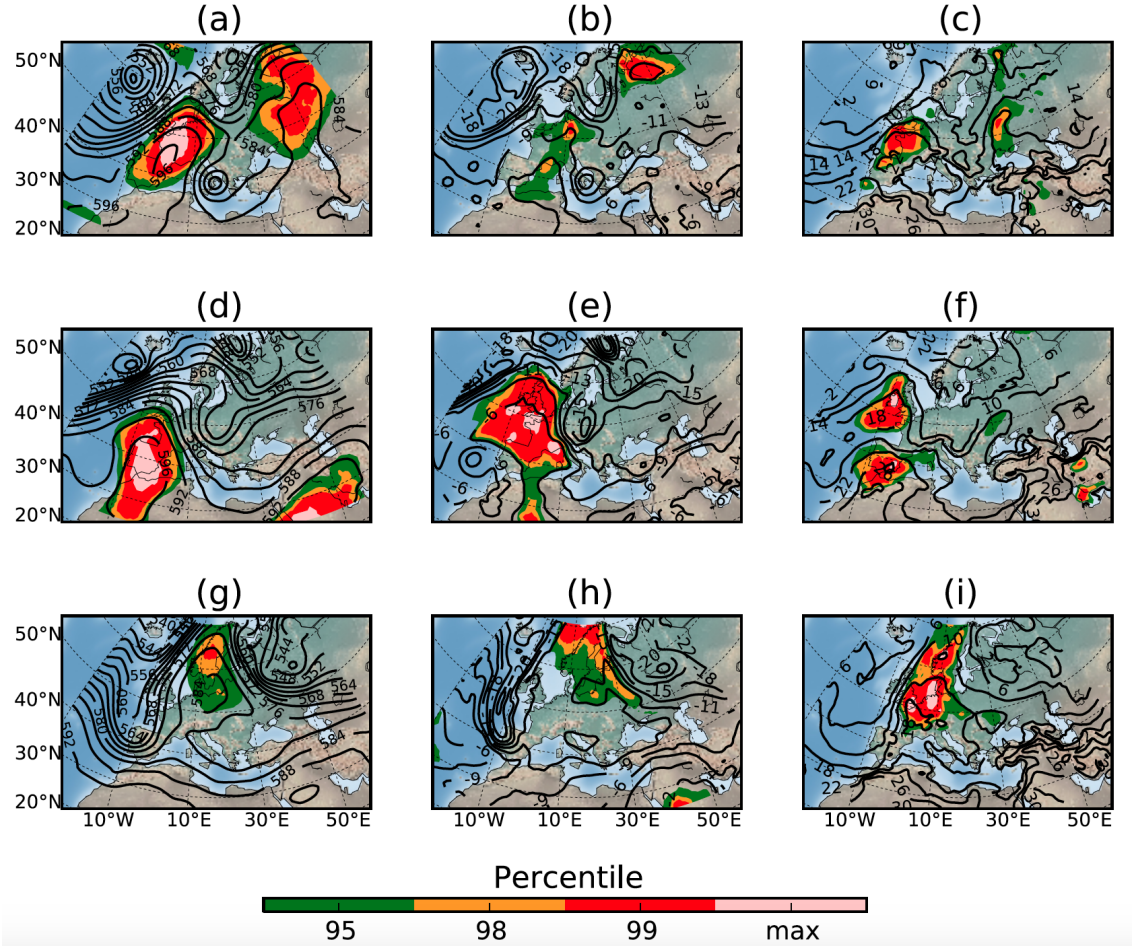

Figure 5.3: Synoptic overview for the three peaks during the heat wave, on (a, b, c) 23 August 2016, (d, e, f) 5 September 2016, and (g, h, i) 13 September 2016. The column of three plots on the left hand side (a, d, g) shows geopotential height at 500 hPa in gpdam; the middle column (b, e, h) shows temperature at 500 hPa in °C; and the right-hand column shows temperature at 850 hPa in °C. These variables are contoured, and the areas for which values exceed the 95th, 98th and 99th percentiles – and the highest value recorded for the reference period 1979–2016 – are colour shaded (see label bar). Figure taken from Zschenderlein et al. (2018). © The authors and John Wiley & Sons Ltd, CC-BY.

The second peak of the late summer warmth primarily affects Spain and evolves under a strong ridge extending over southwestern Europe. Similar to the first peak, a large area surpasses the highest geopotential height values on record (Fig. 5.3d), with a maximum of 599gpdam measured in southern Spain. However, this time the region of highest geopotential heights is displaced to the southwest and is located over Spain and northern Morocco. In contrast to the first peak, temperatures at both 500 and 850 hPa reach record

values (Figs. 5.3e,f), though the areas are not as large and contiguous as their geopotential height equivalents. Small areas of record-breaking temperatures at 850 hPa are observed over Ireland and southeastern Spain, with absolute values of 17 and 26 °C, respectively. As a consequence, the thermal tropopause, according to measurements derived from sounding data from Murcia, Spain, reached altitudes of about 15 km (not shown) – values which are in keeping with observations of tropical air masses.

The final peak of the heat wave is related to an 'Omega-type' blocking, with the ridge centred over central Europe and Scandinavia. The ridge pattern for the preceding days is similar, leading to the interruption of the prevailing westerlies over central Europe and providing conditions that are conducive to the occurrence of extreme temperature events (Pfahl and Wernli, 2012). While 500-hPa geopotential height and temperature values on 13 September 2016 are by far less extreme than during the previous two heat peaks (Figs. 5.3g,h), the 850-hPa temperatures are extreme under the western flank of the ridge over northwestern Europe and Scandinavia, with values over the English Channel and North Sea (above 18 °C) being the highest in the reference period (Fig. 5.3i). Finally, it is worth noting that the elongated trough extending down to the western Iberian Peninsula later develops into a cut-off low over the Bay of Biscay that led to the development of the Biscane Stephanie (Maier-Gerber et al., 2017).

5.5 Large-scale atmospheric precursors

In this section, a large-scale perspective of the heat wave is presented by trying to describe the upstream development of the Rossby wave packets (RWPs) in which the ridges described in the previous section are embedded[1]. A large-amplitude RWP can be considered as the envelope encompassing a series of high-amplitude ridges and troughs in the upper-level flow. The activity of RWPs has been shown to be related to surface weather conditions (Wirth et al., 2018).

Figure 5.4 shows maps of anomalous meridional wind v' (the prime denoting anomalies from the de-trended 1979–2016 mean; see Fragkoulidis et al. (2018) for details) at 300 hPa, temperature T' at 850 hPa and geopotential height at 300 hPa for the three days corresponding to the three peaks in Fig. 5.2a. In all cases, waviness at 300 hPa over the North Atlantic/ Europe region is apparently high. Deep 300-hPa troughs upstream of Europe are marked by strong southerly winds at their eastern flanks, with the 850-hPa temperature anomalies being located farther downstream of the wind maxima (Fig. 5.4).

The time evolution of the RWP can be studied using a refined RWP diagnostic described in Fragkoulidis et al. (2018) that allows one to track zonally constrained wave

[1]The RWP analysis of this section was performed by Georgios Fragkoulidis (JGU Mainz).

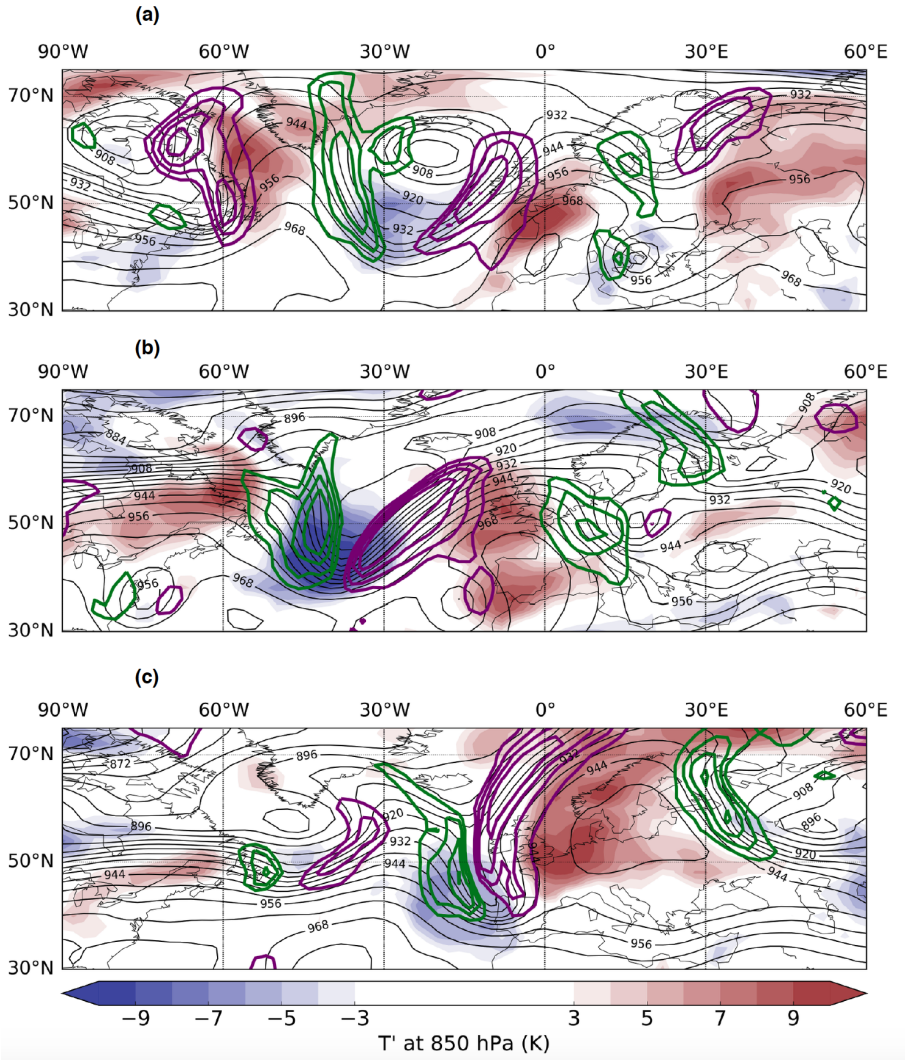

Figure 5.4: Relationship between 300-hPa waviness and low-level temperature anomalies for the three peaks of the heat wave. Geopotential height (black contours, in gpdam) and meridional wind isotachs (with contours, northerlies in green, and southerlies in purple) starting at 20 m s^{-1}, then every 10 m s^{-1}. Coloured areas denote temperature anomalies at 850 hPa (reference period 1979–2016). (a) 23 August 2016, (b) 5 September 2016, and (c) 13 September 2016. Figure taken from Zschenderlein et al. (2018). © The authors and John Wiley & Sons Ltd, CC-BY.

packets propagating eastwards in a self-adjusting latitude band, instead of assessing the Rossby waviness along an entire latitudinal circle using Fourier analysis. The left panel of Fig. 5.5 shows a circumglobal Hovmoeller diagram for the period from mid-August to mid-September 2016, with the 300-hPa RWP amplitudes as contours and meridional wind anomalies v' as colour fill. In addition, the right panel of Fig. 5.5 shows the normalised temperature anomalies T' at 850 hPa (red line) averaged over 35°–55°N and 11°W–15°E, highlighting in orange values in excess of the August – September 90$^{\text{th}}$ percentile (blue dashed line). Apparently, three successive periods of extremely high temperatures occur over Europe between 23 August and 14 September 2016. All of these periods coin-

cide with strong signals of upper-tropospheric waviness, associated with series of strong meridional wind anomalies embedded in the larger-scale RWPs. The meridional wind anomalies mark the troughs and ridges embedded in the RWP. These RWPs form over western North America (at around 120°W) and propagate eastwards with a group velocity of the order of 30° longitude per day (green arrows in left panel of Fig. 5.5). This is faster than the phase speed of the embedded troughs and ridges that can be inferred from the propagation speed of the meridional wind anomalies. The RWPs acquire their maximum amplitude over the North Atlantic Ocean. Their arrival over Europe concur with the aforementioned hot periods. Large-amplitude ridges in all three cases provide favourable conditions for the smaller-scale processes that lead to warming in the locations under study (see next section). Finally, after the dispersion of the RWPs, the warm air masses are not sustained, and short periods of mild temperatures provided relief to the affected areas.

Figure 5.5 clearly shows that the enhanced atmospheric upper-level waviness is a midlatitude propagating phenomenon that can be traced back upstream for a few days before the event and is initiated several thousand or, as for the second heat wave with a potential precursor in the Pacific Ocean, more than 10,000 km to the west of Europe. The related large-scale, sometimes even planetary-scale, Rossby wave dynamics suggest a relatively high degree of predictability – and indeed at lead times of a few days, the data from the 51 members of the ECMWF ensemble prediction system shifted towards positive anomalies for Bordeaux, Seville, and Trier, indicating increasing probabilities of an imminent heat wave at the respective locations (more details in section 5.7). However, the spatio-temporal details of the extent of the body of warm air ultimately depend on the phase velocity and amplitudes of the Rossby waves (i.e. the trough ridge systems embedded in the RWP – see discussion in Fragkoulidis et al. (2018) for the 2003 and 2010 European heat waves), as well as on the related temperature advection, subsidence and heat fluxes in the boundary layer. The role of the latter two processes is discussed in the next section.

5.6 Development of high temperature extremes near the surface

In this section, following questions are adressed: (i) What is the place of origin of the hot air masses? (ii) Which physical processes contribute to the high temperature extremes at the observation stations? (iii) Does the heat propagate from upper levels to the surface or vice versa?

Figure 5.6a shows 5-day backward trajectories, starting at 12 UTC on 23 August

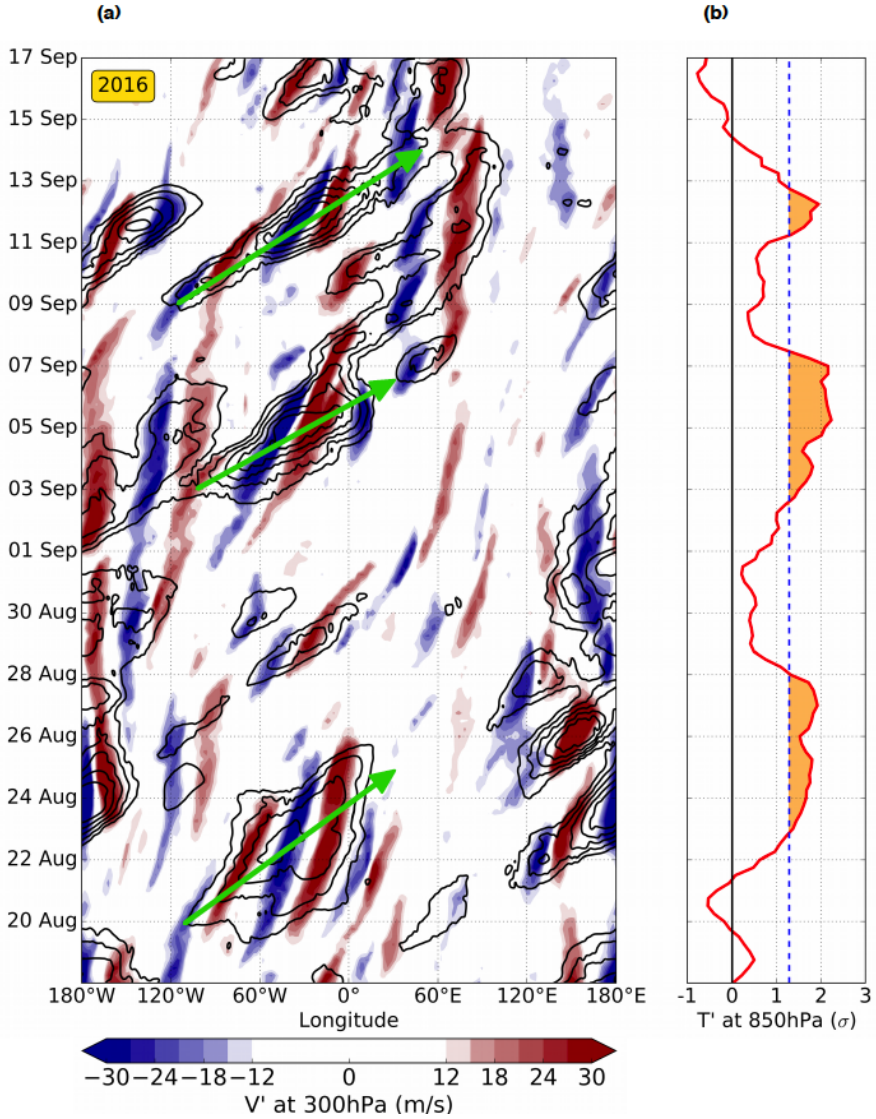

Figure 5.5: Hovmoeller diagram illustrating the upper tropospheric dynamics for the 2016 heat wave. The contours in (a) depict 300-hPa RWP amplitude (in $\mathrm{m\,s^{-1}}$; contours every $4\,\mathrm{m\,s^{-1}}$ from 22 to $38\,\mathrm{m\,s^{-1}}$). A weak bivariate interpolation (using cubic Hermite splines) has been applied to slightly smoothen the resulting field. The colour fill represents the 300-hPa meridional wind anomaly (blue for northerlies and red for southerlies). The time resolution is 6 h. Both fields are averaged over a 20° latitude band which self-adjusts (within the 30°N–70°N band) to those latitudes in which the highest RWP amplitudes occur. The green arrows represent the approximate group velocity of the eastward-propagating RWPs. (b) Normalised temperature anomaly at 850 hPa (red line) averaged over 35°–55°N and 11°W–15°E (with a cos(latitude) weighting). Orange shading corresponds to temperature anomaly values in excess of the 90$^{\mathrm{th}}$ percentile for the months of August and September (blue dashed line). Figure taken from Zschenderlein et al. (2018). © The authors and John Wiley & Sons Ltd, CC-BY.

2016 between 975 and 550 hPa over Bordeaux (note that trajectories at the surface in this three-dimensional plot are the projection of the upper-air trajectories, both of which are

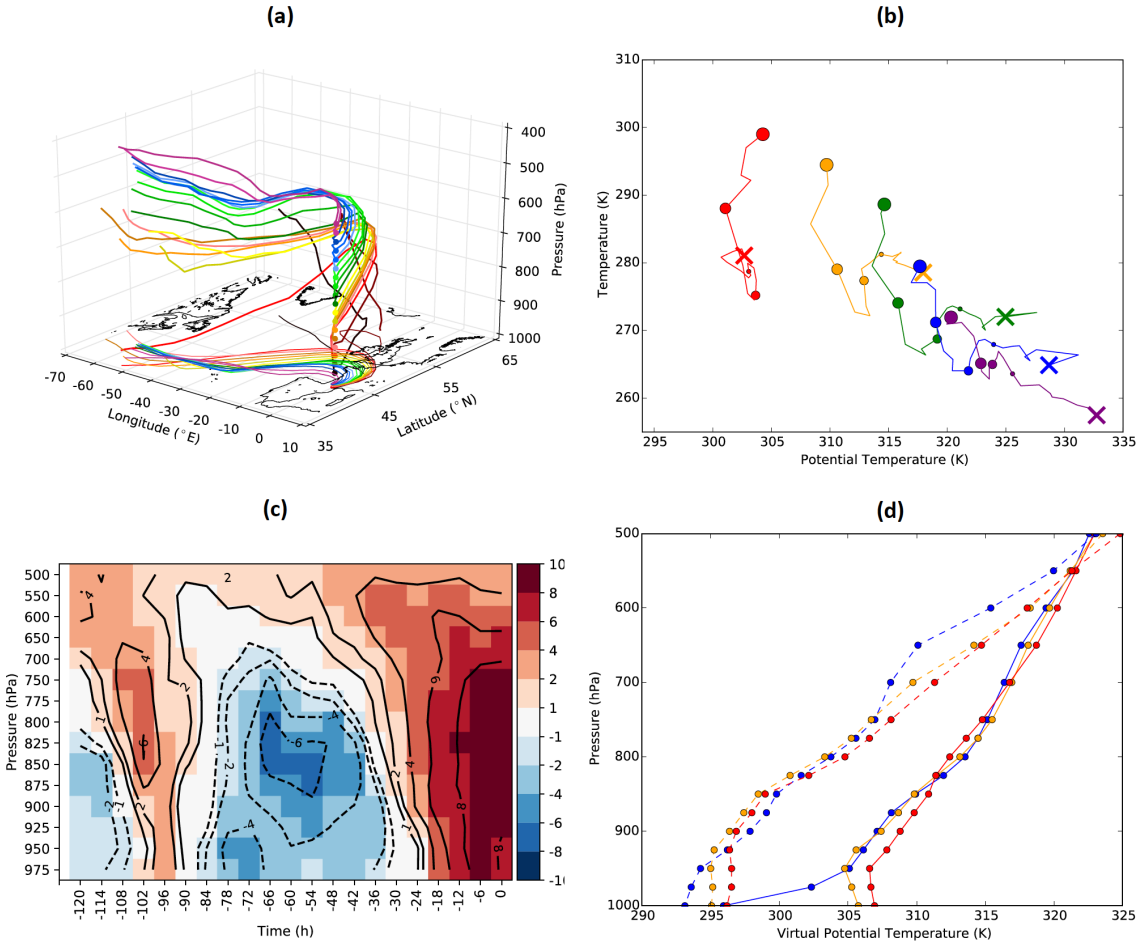

Figure 5.6: Lagrangian and Eulerian perspectives of the development of the peak of the heat wave in Bordeaux between 12 UTC on 18 August and 12 UTC on 23 August 2016. (a) Three-dimensional representation of 5-day backward trajectories, started over Bordeaux between 975 and 550 hPa in 25 hPa increments. Only starting levels at which temperatures exceeded the 95$^{\text{th}}$ percentile at 12 UTC on 23 August 2016 were used. The surface position of the parcel is given on a two-dimensional map (bottom layer), with the colours indicating identical trajectories (black/reddish: 975–900 hPa, orange/yellowish: 875–800 hPa, greenish: 775–700 hPa, blueish: 675–600 hPa, purple: 575–550 hPa; the colour coding depends on the starting level of the trajectories above Bordeaux). (b) T–θ diagram (cf. section 4.5) showing the evolution of the mean T and θ values for the trajectories shown in (a), grouped into 5 pressure levels that started over Bordeaux: 975–900 hPa (red), 875–800 hPa (orange), 775–700 hPa (green), 675–600 hPa (blue) and 575–550 hPa (purple). The filled circles of decreasing size represent 24 h intervals prior 23 August 2016 (i.e. 0, 24, 48 and 72h). The cross indicates the origin. (c) 6-hourly vertical temperature anomalies from the climatological mean (colour shading, in K; base period 1979–2016) over Bordeaux for 18–23 August 2016. (d) Vertical virtual potential temperature profiles θ_v for 18 August (dashed, pre-heat wave) and 23 August (heat wave) at 06 (blue), 12 (orange) and 18 UTC (red). Figure taken from Zschenderlein et al. (2018). © The authors and John Wiley & Sons Ltd, CC-BY.

shown in the same colour). Almost all trajectories arriving at Bordeaux on 23 August 2016 cross the North Atlantic Ocean between 800 and 500 hPa (i.e. above the marine boundary layer). Near Europe, 48 h before the event, the air parcels strongly descend along an anticyclonic trajectory to approach Bordeaux from the northeast – that is, the direction from which they travel for a long time over land – experiencing clear-sky conditions (not shown). The T–θ phase diagram (cf. section 4.5) clearly illustrates that the air parcels, especially when arriving at lower levels over Bordeaux, experience a substantial increase in temperature of 20–25 K due to adiabatic compression 48 h prior to the event (Fig. 5.6b). The temperature increase is close to adiabatic, as indicated by the very small rate of change of the parcels' potential temperature during this stage (Fig. 5.6b). Apparently, this adiabatic warming is consistent with the subsidence visible in Fig. 5.6a. Just before the extreme temperature event, the trajectories closest to the surface experience slight diabatic heating (red line in Fig. 5.6b), presumably due to turbulent heat fluxes as they are transported above land surfaces (Fig. 5.6a). Figure 5.6c shows the development of temperature anomalies between 18 and 23 August in the lower and mid-troposphere above Bordeaux from an Eulerian perspective. Between 90 and 36 h before the peak temperatures are reached at 12 UTC on 23 August 2016, the atmosphere is comparably cold, especially between 900 and 800 hPa. The temperatures increase rapidly before the actual extreme temperature event. Interestingly, the positive temperature anomalies initially occur at higher levels and subsequently penetrate downwards, 'propagating' from the upper levels to the surface. This propagation is consistent with the subsidence, which is remarkably high in the last 36 h prior to the heat wave. Overall, this suggests that subsidence and adiabatic compression are the driving factors in the development of high temperatures at the surface. Figure 5.6d shows diurnal cycles (06, 12, 18 UTC) of vertical profiles of virtual potential temperature θ_v for the pre-heat wave on 18 August 2016 (dashed lines) and the heat wave on 23 August 2016 (solid lines). The profiles reveal (i) the strong lower tropospheric warming between 18 and 23 August 2016, (ii) the reasonably constant and shallow depth of the well-mixed (i.e. θ_v nearly constant with height) boundary layer, and (iii) a strong diurnal cycle on 23 August 2016.

Figure 5.7 shows the same set of panels as Fig. 5.6, but for the hottest September day on record in Seville (05 September 2016). Backward trajectories are only started up to 700 hPa, because at higher altitudes the temperatures were not extreme, i.e. above the 95$^{\text{th}}$ percentile (Fig. 5.7c). Compared with the Bordeaux episode, the air parcels travel a much shorter distance during the 5 days preceding the Seville heat wave. Although most of the trajectories have an anticyclonic curvature, the individual origins of the air parcels are diverse. Parcels which end up near the surface in Seville originate in northern Spain, and those ending up at higher altitudes over Seville have their origins mostly over warm northern Africa – a pathway that is favoured by the large-scale setting to the

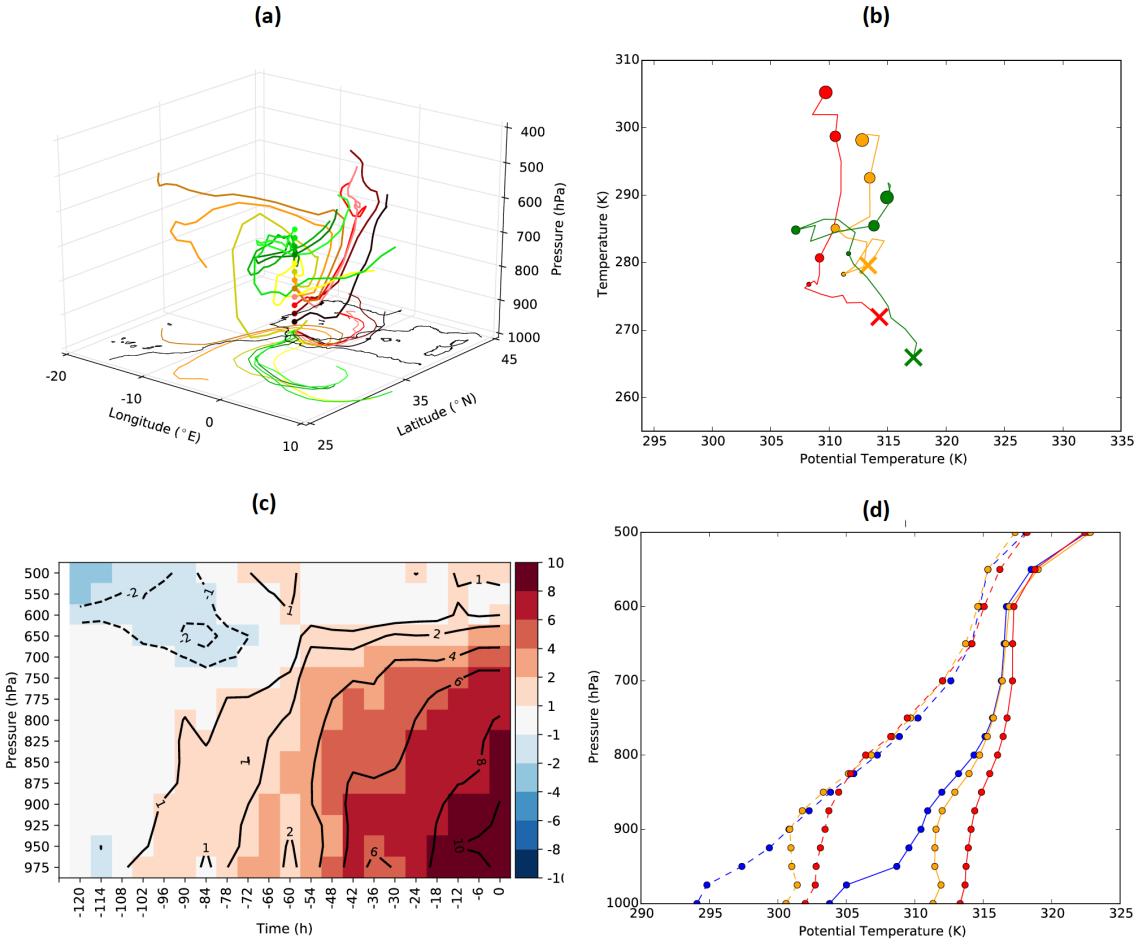

Figure 5.7: As in Fig. 5.6, but for Seville. Backward trajectories are started between 975 and 700 hPa, and the 5-day period under consideration is from 12 UTC on 31 August to 12 UTC on 5 September 2016. Figure taken from Zschenderlein et al. (2018). © The authors and John Wiley & Sons Ltd, CC-BY.

North (RWP) and realised in connection to a short upper-level trough to the southwest of the Iberian Peninsula (Fig. 5.4b). Nearly all trajectories enter the Seville area from the east. Parcels arriving near the surface warm adiabatically in the last 72 h by about 30 K (Fig. 5.7b). They experience subsidence over a longer time period (3 days) than those over Bordeaux (2 days). Again, this suggests that subsidence contributes significantly to this heat wave event. Interestingly, the air parcels starting between 700 and 775 hPa in Seville are diabatically heated 48 to 24 h before the event. This takes place in the surroundings of the Atlas Mountains (Fig. 5.7a), which suggests that turbulent heat fluxes and moist convection in this area plays an important role. A more detailed analysis of the diabatic processes (including cloud microphysics) is beyond the scope of this study. Figure 5.7c shows the vertical structure of the atmosphere over Seville from 31 August to 5 September. The markedly different behaviour of this heat event compared to the former case is striking. Distinct positive temperature anomalies develop 48 h prior to the

extreme temperature episode, with a maximum at the surface and the lower tropospheric layers. Compared with the lower planetary boundary layer heights 5 days before the high temperature event in Seville, the boundary layer deepens during the heat event. This can be inferred from the near-constant vertical profile of θ_v in Fig. 5.7d. Black et al. (2004) also found elevated planetary boundary layer heights above Paris during the 2003 heat wave. It appears that strong insolation, ensuing surface fluxes and dry convection deepen the boundary layer. The evolution of the temperature profiles suggests a bottom-up development similar to the findings of Miralles et al. (2014). Thus, adiabatic compression works in concert with boundary layer processes to create the hottest September day ever recorded in Seville. Despite the suggested importance of subsidence and boundary layer processes, they cannot be considered to be independent of the RWP. The large ridge embedded in the RWP is instrumental in steering the parcels toward the Seville region on anticyclonic trajectories and under clear-sky conditions.

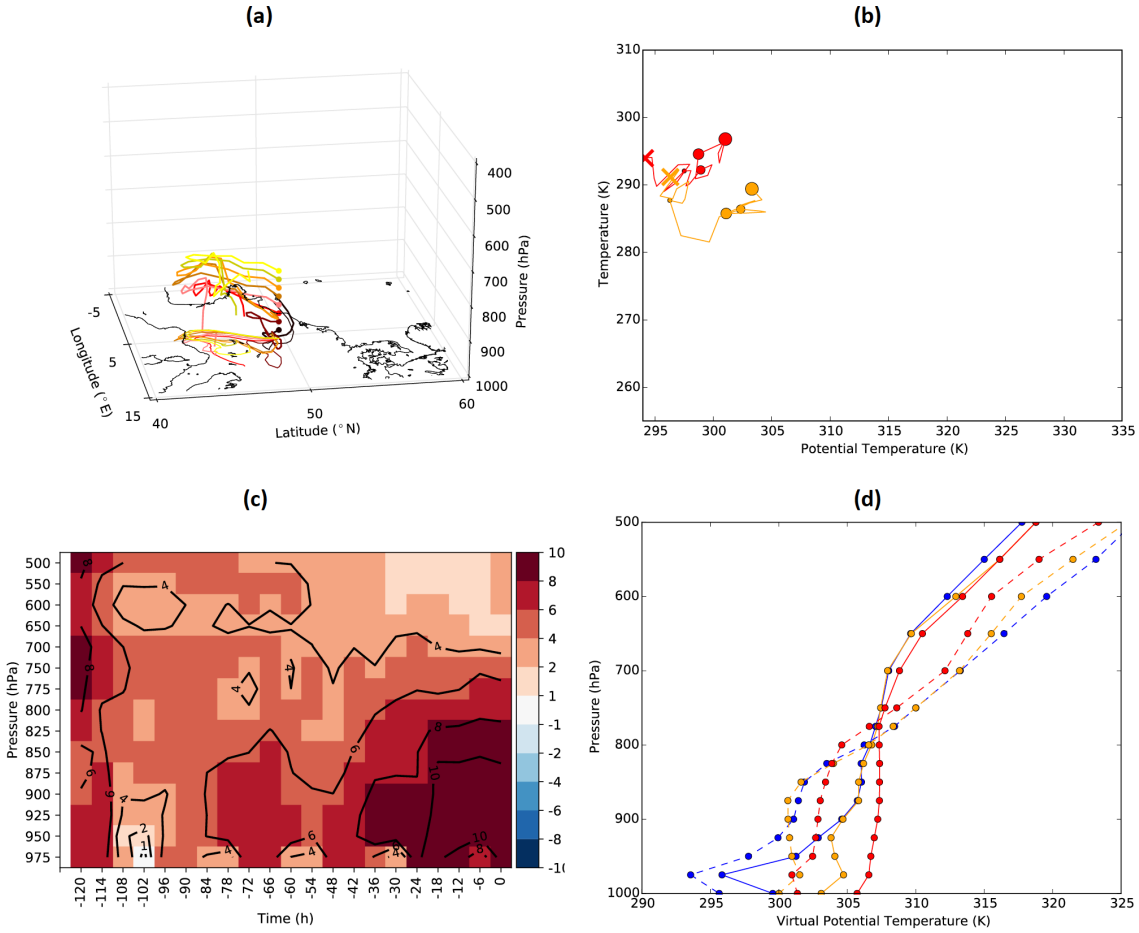

Figure 5.8: As in Fig. 5.6, but for Trier. Backward trajectories are started between 975 and 800 hPa, and the 5-day period considered is from 12 UTC on 8 September to 12 UTC on 13 September 2016. Figure taken from Zschenderlein et al. (2018). © The authors and John Wiley & Sons Ltd, CC-BY.

Yet another picture emerges as an explanation of the cause of the hottest September day on record at Trier on 13 September 2016. Most of the trajectories – which start from 975 up to 800 hPa, where temperature extremes are present over Trier – originate close to the Rhône valley and northern Italy (Fig. 5.8a), yielding a horizontal transport over comparably short distances and above land surfaces only. The lowest trajectories are trapped in the planetary boundary layer, suggesting significant interaction with the land surface, presumably due to enhanced surface heat fluxes. This can be seen in Fig. 5.8b as an increase in potential temperature of approximately 10 K (diabatic heating). The fluctuating temperature shown in Fig. 5.8b illustrates the diurnal temperature variation. Note that the diurnal temperature variation is also clearly visible in Fig. 5.8c, as the lowest temperature anomalies are always attained at 06 UTC near the surface. The air parcel temperature increases shown in Fig. 5.8b are generally smaller than those observed for the other locations, and subsidence from higher levels is not observed for this location. Instead, heat is trapped in the planetary boundary layer and accumulated day by day (Fig. 5.8c), leading to an increase in the top of the boundary layer over Trier (Fig. 5.8d). The boundary layer top is quite high for this location and time of year (i.e. late in the year). Figure 5.8c also reveals positive temperature anomalies above Trier up to 500 hPa from 8–13 September. It is concluded that the main factor in the development of the extreme temperature episode over Trier is the influence of diabatic processes in the planetary boundary layer – for example, heating due to upward-directed surface sensible heat fluxes caused by strong insolation over several days, which is experienced both locally over Trier and by air parcels reaching Trier over the same period.

5.7 Predictive skill

The last section of this case study investigates the predictability of the temperature peaks in Bordeaux, Seville and Trier. For that, the cumulative distribution functions (CDF) of the ECMWF ensemble 2-m temperature forecasts for different lead times are compared with the observation and the reanalysis (ERA-Interim).

10–15 days prior to the heat wave on 23 August 2016 in Bordeaux, the ensemble is not able to forecast the event, although a shift towards warmer temperatures is apparent (Fig. 5.9a). Although the five-day forecasts shifts to slightly warmer conditions, still, 80% of the ensemble members underestimate the temperature from ERA-Interim (dashed green vertical line in Fig. 5.9a). 20% of the members even overestimate the temperature, hence, the forecast uncertainty is still quite high. Only on 21 August, i.e. 2 days prior to the event, uncertainty of the forecast reduces, albeit slightly underestimating the temperature. However, the observed temperature (solid green vertical line in Fig. 5.9a) is

overestimated.

Similar to the Bordeaux case, also the 10–15 day forecast is slightly warmer than the model climatology, but with a generally much too cold distribution compared to the analysed/observed temperature (Fig. 5.9b). But even 5 days prior to the event, the distribution is still too cold, however, the ensemble spread is reduced compared to the higher lead times. The 3-day ensemble forecast shifts rapidly towards higher temperatures, and the 2- and 1-day forecasts predict the temperature quite well.

Also for the last event in Trier, 10–15 day ensemble forecasts predict warmer than average temperatures and the signal is more pronounced compared to the other cases (Fig. 5.9c), i.e. predictive skill is enhanced for this case. Interestingly, forecasts change substantially between 7- and 5-day lead time: the ensemble mean increases, the distribution sharpens and especially the cold distribution vanishes. From 31 August, forecasts are very similar and slightly underestimate the temperature from the reanalysis. Striking is the large difference between the reanalysed and observed temperature. It is hypothesised that local effects, e.g. urban heat island, local wind systems, in the vicinity of the station have an impact on the observed temperature, which cannot be represented by the model.

Overall, 10–15 day forecasts for the three cases show some signal of a warmer than average temperature and the ensemble progressively shifts towards higher temperatures and the distribution sharpens towards the event. However, forecasts are not always improving progressively, but can improve abruptly, as for example the 7- and 5-day forecast for Trier. A more in depth analysis of the possible causes for the different reliabilities of the ensemble is beyond the scope of this study and left for further analysis.

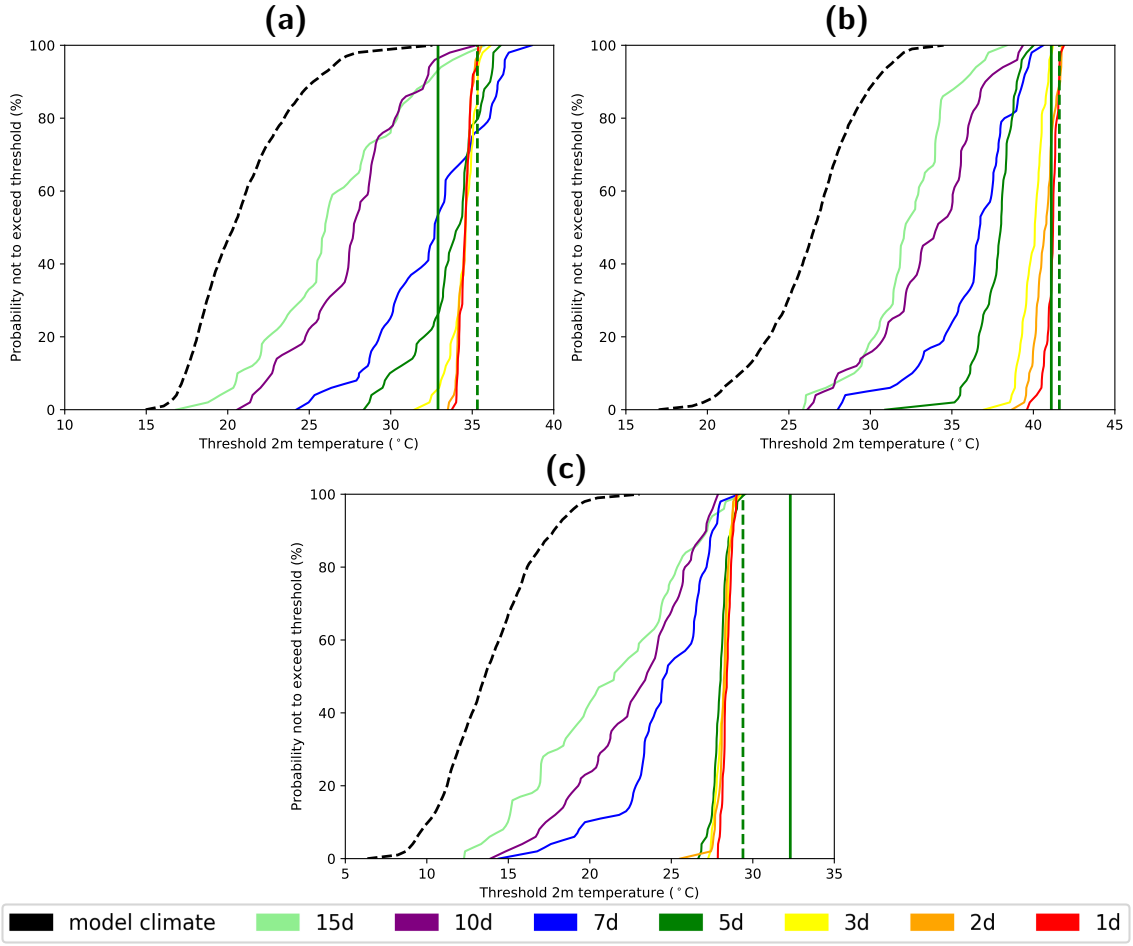

Figure 5.9: Cumulative distribution functions of ECMWF 2-m temperature ensemble forecasts for different lead times and cities. (a) Bordeaux, forecasts valid on 23 August 2016, (b) Seville, forecasts valid on 05 September 2016 and (c) Trier, forecasts valid on 13 September 2016, and at 12 UTC, respectively. The black dashed line indicates the model climate and coloured lines the lead times of the forecasts. The vertical dashed (solid) line represents the temperature from ERA-Interim (observation) for the respective day.

Chapter 6

Processes leading to high near-surface temperatures

This chapter presents a climatological analysis how high near-surface temperatures during heat waves can be explained by temperature advection, vertical motion and diabatic processes. At first, section 6.1 provides a detailed description on the calculation of trajectories. The identification of heat waves has been introduced in section 4.3. Then, section 6.2 presents the typical duration and frequencies of the events, followed by the synoptic patterns associated with the onset of heat waves in section 6.3. The clustering of the trajectories is discussed in section 6.4, as well as the source regions and the physical processes along the trajectory clusters in sections 6.5 and 6.6. After that, it is quantified, in section 6.7, how long trajectories stay in the target region.

6.1 Method – Trajectory calculation

Ten-day backward trajectories are computed with LAGRANTO (Sprenger and Wernli, 2015), which are driven by six-hourly ERA-Interim three-dimensional wind fields on a 1° x 1° latitude/ longitude grid and 60 vertical model levels. Trajectories are started for every heat wave day at 12 UTC. In order to understand the build-up of the near-surface heat, trajectories are started at 10, 30, 50 and 100 hPa above ground level. Starting points above sea surfaces are excluded. Furthermore, the following variables are traced along the trajectories: pressure (p), temperature (T), potential temperature (θ), relative humidity (rh), specific humidity (q) and 6-hourly accumulated surface sensible heat fluxes ($sshf$).

For each trajectory, it is the aim to quantify the overall temperature and potential temperature changes and relate these changes to vertical motions. For that, the approach of Binder et al. (2017) is used and the maximum changes of temperature and potential temperature, as well as maximum pressure increases, i.e. descents, along all trajectories

are calculated. More precisely, we calculate for both T and θ the maximum absolute difference between the respective value at the starting point of the trajectory and the previous time steps. The outcome of this method is referred to as ΔT_{max} and $\Delta\theta_{\text{max}}$, respectively (Fig. 6.1). In order to relate these changes to the descent of the air parcels, we also calculate the maximum pressure increase in all 48 h windows along the trajectories (Fig. 6.1). Accordingly, the outcome of this method is referred to as Δp_{max}. These three values allow us to sort the trajectories into different categories with different thermodynamic characteristics: (i) positive ΔT_{max} and negative $\Delta\theta_{\text{max}}$ (cluster *A*) , (ii) both positive ΔT_{max} and $\Delta\theta_{\text{max}}$ (cluster *B*), (iii) negative ΔT_{max} and positive $\Delta\theta_{\text{max}}$ (cluster *C*), and (iv) both negative ΔT_{max} and $\Delta\theta_{\text{max}}$ (cluster *D*). Assuming a surface pressure of 1000 hPa, the starting points of the trajectories are defined at 990, 970, 950 and 900 hPa. Hence, a maximum pressure increase of 100 hPa in 48 h for air parcels starting at 900 hPa would imply a level of around 800 hPa as maximum height, when the ascend directly starts from 900 hPa. In that case, the air parcel is still in the lower troposphere. In addition to the thermodynamic characteristics, trajectories can therefore be subdivided into clusters with strong descent, i.e. more than 100 hPa in 48 h, and weak descent, i.e. less than 100 hPa in 48 h. The choice of the 100 hPa threshold is subjective, but the results in the next sections justify this threshold. Section 6.4 shows that the subdivision in strong and weak descent is mainly important for cluster *B*. Table 6.1 summarises the characteristics of the different clusters. This physical clustering is very useful in quantifying the relative roles of subsidence and diabatic processes in shaping near-surface high temperature extremes.

Table 6.1: Definition of the trajectory clusters, bold marked clusters are discussed in the study. ΔT_{max}, $\Delta\theta_{\text{max}}$ and Δp_{max} are described in section 6.1 and Fig. 6.1. Table taken from Zschenderlein et al. (2019). © The authors and John Wiley & Sons Ltd, CC-BY.

Cluster	ΔT_{max}	$\Delta\theta_{\text{max}}$	Δp_{max} **in 48 h**
A	>0	<0	not considered
$\boldsymbol{B_{sd}}$	>0	>0	$>$ 100 hPa
$\boldsymbol{B_{wd}}$	>0	>0	$\leq$ 100 hPa
C	<0	>0	not considered
D	<0	<0	not considered

In order to identify the residence time of air parcels in the regions defined in Fig. 4.1, forward trajectories are calculated for all identified heat wave days. The residence time is defined as the time period between the start of the trajectories and the first time exiting the region. Due to the different sizes of the solid boxes in Fig. 4.1, the region is defined as a circle with a fixed radius of 500 km. The centre of the circle is located in the middle of each solid box, as exemplarily shown for Central Europe in Fig. 4.1. A radius of 500 km is chosen because the regions have a size of roughly 900x900 km^2. Forward trajectories

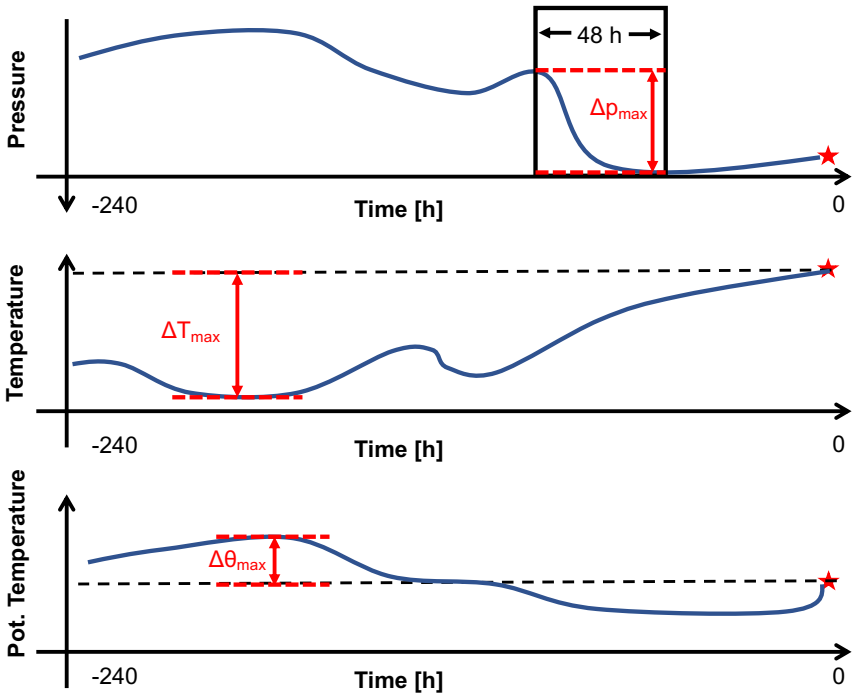

Figure 6.1: Schematic to describe the three properties used for the clustering of trajectories. The three diagrams show a temporal evolution of temperature (T), pressure (p) and potential temperature (θ) along one backward trajectory, which has its starting point at the red star. The three red-marked properties Δp_{max}, ΔT_{max} and $\Delta\theta_{\text{max}}$ will be used for the clustering described in Table 6.1. For further explanations, see section 6.1. Figure taken from Zschenderlein et al. (2019). © The authors and John Wiley & Sons Ltd, CC-BY.

starting near the border of the region may have very short residence times. To avoid these cases, the amount of initialisation points of the forward trajectories are reduced to the dashed rectangles inside the regions (Fig. 4.1). As an example, forward trajectories for Central Europe are initialised only between 47° and 53°N and 8° and 12°E and quantify the duration air parcels need to leave the circle with its centre at 50°N and 10°E.

The following section first gives a statistical overview of the identified heat waves, followed by the typical 500-hPa geopotential height onset patterns. Subsequently, the origin of the trajectories and the associated processes are presented.

6.2 Heat wave statistics

Typically in each region one or two heat waves occur during a year (Fig. 6.2a). The variability of occurrence is largest in western Russia, presumably due to the continental climate. Maximum numbers of heat waves per year range between five and eight. It is possible that two heat waves are only interrupted by one day, although this is very rare. The extreme summer of 2003, which mainly affected Central Europe (Fink et al., 2004),

consists of five heat waves, each with different lengths (Fig. A1.1). The most intense one occurred during the first half of August 2003 (Tab. A1.1). Hence, the accumulation of several heat waves can lead to an overall extreme summer. Regions under maritime influence, i.e. Greece/Italy, the Iberian Peninsula and the British Isles have some years with no heat wave, presumably due to the generally lower climate variability in the maritime regions. Additionally it is also possible that extreme hot days occur on a smaller scale in the maritime regions.

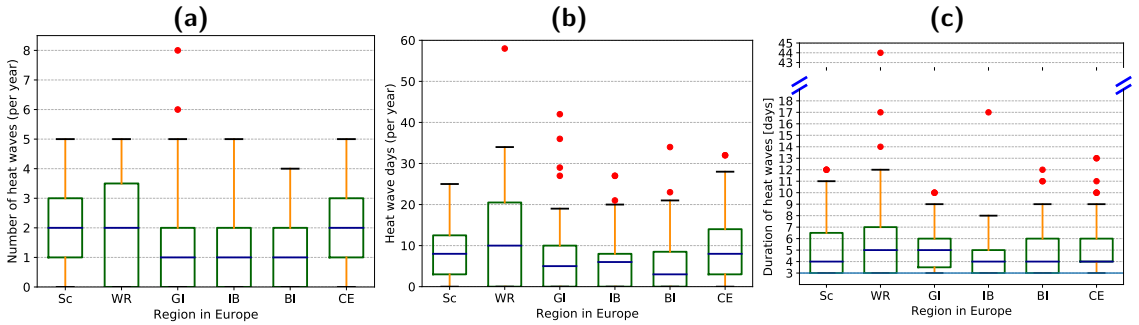

Figure 6.2: A statistical overview of the identified heat waves in Scandinavia (Sc), western Russia (WR), Greece/Italy (GI), Iberian Peninsula (IB), British Isles (BI) and Central Europe (CE). The boxplots in (a) depict the numbers of heat waves per year, (b) shows the number of heat wave days per year and (c) illustrates the duration of the heat waves. Note the cutted y-axis in (c). Blue horizontal lines denote the median, the boxes the interquartile range, the whiskers 1.5·IQR and the red dots the outliers. Figure taken from Zschenderlein et al. (2019). © The authors and John Wiley & Sons Ltd, CC-BY.

Throughout the different regions, on average five to ten heat wave days occur per year (Fig. 6.2b). The annual maxima of heat wave days ranges between 25 days for Scandinavia and nearly 60 days for western Russia. Similar to the heat wave occurrence, the highest variability is found for western Russia. The maximum numbers of heat wave days of about 60 in western Russia and 30 in Central Europe concur with the extreme heat waves in 2010 (Grumm, 2011; Quandt et al., 2017) and 2003 (Fink et al., 2004), respectively (Figs. A1.1 and A1.2).

Fig. 6.2c presents the typical duration of heat waves in Europe. By construction, the minimum duration is three days, the median duration ranges between four and five days. The median duration is similar to the typical minimum duration of atmospheric blocking, which often coincides with high temperatures in summer (Pfahl and Wernli, 2012). Most of the heat waves last between three and seven days, while durations above ten days are rare. A maximum duration of 44 days in western Russia is noteworthy because of its extreme length. In fact, the 44 days refer to the 2010 extreme heat wave in Russia, which had large impacts. The maximum duration of heat waves in Central Europe is 13 days, over the British Isles and Scandinavia 12 days, over the Iberian Peninsula 17 days and in

Greece/Italy 10 days, respectively.

The heat wave durations are similar to Stefanon et al. (2012) and Perkins et al. (2012). Fischer and Schär (2010) defined heat waves with a minimum duration of six days and obtained generally longer heat waves, but with a decreased occurrence probability compared to our results.

The HWMId can be used for a ranking of the most intense heat waves in the different regions. As a result, the two most intense heat waves in Central Europe occurred in 2003 and 2015 (Tab. A1.1), in Scandinavia in 1991 and 2014 (Tab. A1.2), in western Russia in 2010 and 1981 (Tab. A1.3), in Greece/Italy in 2007 and 1988 (Tab. A1.4), in the Iberian Peninsula in 1982 and 2015 (Tab. A1.5), and in the British Isles in 1990 and 2006 (Tab. A1.6). Interestingly, no year features the most intense heat wave in more than one region, indicating that extreme heat waves rarely extend over our defined regions.

6.3 Onset pattern

This section analyses composites of 500-hPa geopotential height patterns during the onset of heat waves in Europe. Onsets are defined as the first day of a heat wave.

In all regions, upper-level ridges are co-located with the onset of heat waves (Fig. 6.3), corroborating the findings of Pfahl and Wernli (2012) and Sousa et al. (2018). The variability of the geopotential height in the area of the ridges is low compared to the regions upstream, polewards and downstream of the heat waves. Although the ridge pattern is similar for the individual heat waves, the amplitude of the upstream trough is more variable.

The shape of the ridge over Scandinavia resembles an omega-like blocking structure associated with a dominant interruption of the westerlies (Fig. 6.3b), whereas ridges over Central Europe (Fig. 6.3c), the British Isles (Fig. 6.3a) and western Russia (Fig. 6.3d) do not have this pronounced omega shape. Ridges in southern Europe over Greece/Italy (Fig. 6.3f) and the Iberian Peninsula (Fig. 6.3e), however, are much less pronounced. In fact, those ridges are comparably flat. Thus heat waves in southern Europe occur while other regions in Europe are under influence of nearly zonal weather regimes. Composites by definition average over many patterns, which means that individual cases can have different trough-ridge configurations. Sousa et al. (2018) emphasized that it is important to differentiate between classical high-latitude blocking and sub-tropical ridges when investigating the relationship to heat events in Europe. The authors argued that classical European blocking configurations are not associated with heat waves over more southerly latitudes, which often experience negative temperature anomalies during blocking episodes. Those negative temperature anomalies can be explained by the troughs at

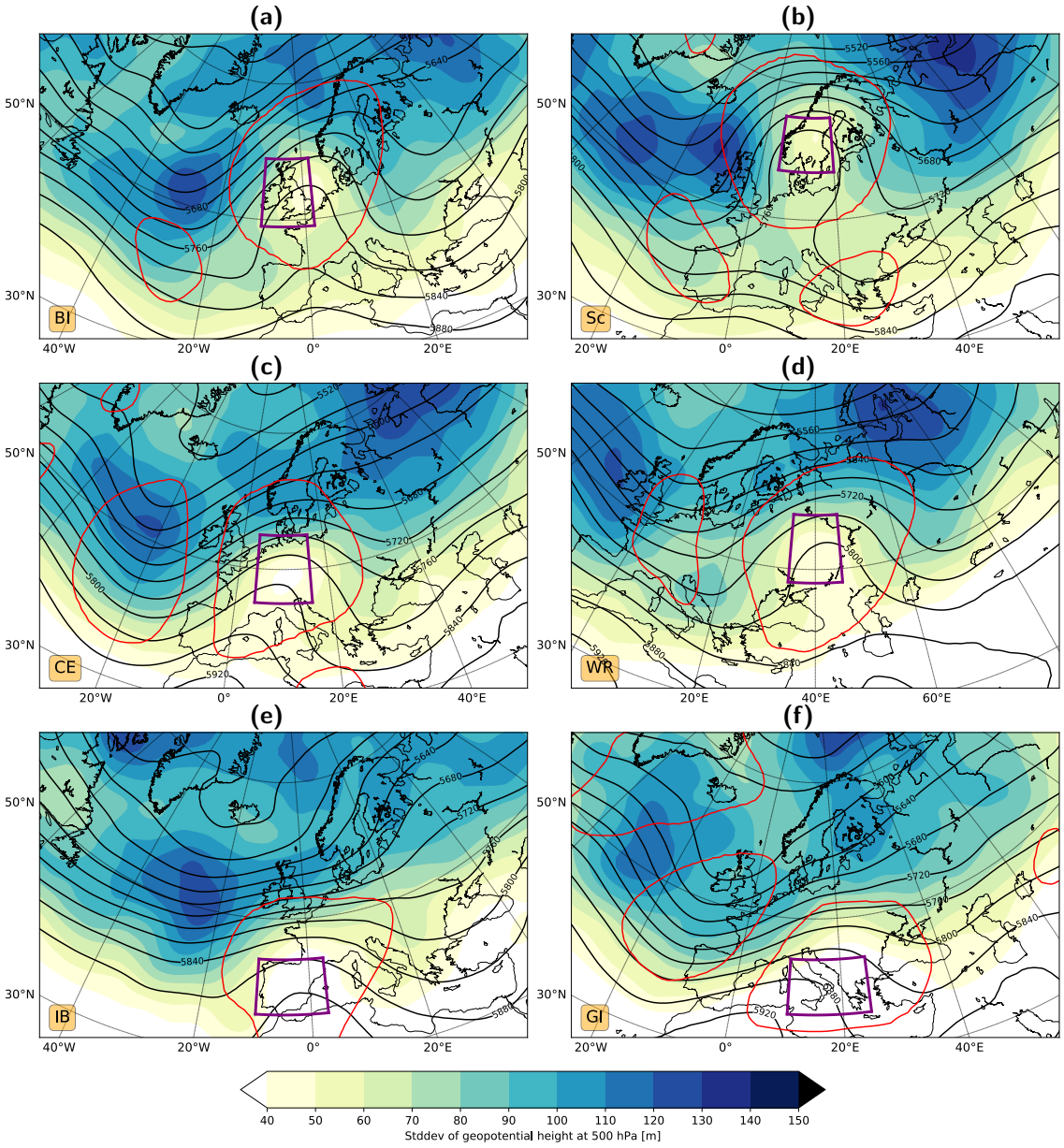

Figure 6.3: Geopotential height patterns during the onset of heat waves in different regions in Europe: (a) British Isles (BI, see box in bottom left corner), (b) Scandinavia (Sc), (c) Central Europe (CE); (d) western Russia (WR), (e) Iberian Peninsula (IB) and (f) Greece/ Italy (GI). The contours depict the mean and colours the standard deviation over all events of the 500-hPa geopotential height (in m). Areas surrounded by the red lines indicate significance at the 1% level based on a Student's t-test. Figure taken from Zschenderlein et al. (2019). © The authors and John Wiley & Sons Ltd, CC-BY.

the eastern and western flanks of the blocking over Scandinavia (Fig. 6.3b).

Comparing the synoptic patterns for the European regions reveal some interesting inter-regional relations. A simultaneous heat wave over the British Isles and Scandinavia is improbable because the ridges are too narrow (Fig. 6.3a,b), although it should be noted

that during the strong heat wave in 2018 both regions featured a simultaneous heat wave (not shown). Furthermore, the synoptic patterns are nearly zonal in most parts of Europe under heat wave conditions in western Russia (Fig. 6.3d). This is also the reason why during the extreme heat wave in 2010 over western Russia the rest of Europe was hardly affected by heat waves (Fig. A1.2). Of course, these patterns are very variable from case to case, but overall, it can be concluded that heat waves in Europe are affected by upper-level ridges with a zonal extension of < 2000 km and a varying amplitude, depending on the latitude of the affected region.

6.4 Trajectory clusters

After applying the method described in section 6.1 (see also Fig. 6.1) to the heat wave trajectories in each region, each trajectory, according to its values of ΔT_{max}, $\Delta\theta_{\mathrm{max}}$ and Δp_{max}, can be associated with one of the five different clusters (see Tab. 6.1 for the definition of the clusters). As an example, the outcome of this procedure is shown for Central Europe in Fig. 6.4a. The diagrams of ΔT_{max}, $\Delta\theta_{\mathrm{max}}$ and Δp_{max} for the other European regions are shown in Figs. A1.3-A1.7. Obviously, no trajectories can be found on or near the axes, because the maximum changes of both T and θ were calculated. A trajectory on the axes would imply that either T or θ would be strictly constant throughout the whole 10-day period, which does not exist in the real atmosphere.

About one quarter of all trajectories creating a heat wave in Central Europe belong to cluster *A* (upper left quadrant in Fig. 6.4a). Air parcels in this cluster experience an overall diabatic cooling of up to -20 K and in the same time a temperature increase of up to +80 K during the 10-day period. This is possible due to subsidence, which leads to adiabatic warming overcompensating the diabatic cooling of the air parcels. Hence, stronger subsidence is accompanied by higher temperature increases. The diabatic cooling during the subsidence in the free atmosphere is presumably due to radiative cooling (Bieli et al., 2015; Binder et al., 2017; Raveh-Rubin, 2017).

Trajectories in the upper right quadrant of Fig. 6.4a comprise roughly three quarters of all trajectories establishing a heat wave in Central Europe. Similar to cluster *A*, air parcels experience a maximum temperature increase of up to +80 K, but contrary to cluster *A*, air parcels are diabatically heated by up to +40 K. The trajectories in the upper right quadrant of Fig. 6.4a can be subdivided into two clusters: air parcels descending more than 100 hPa in 48 h (red colours in Fig. 6.4a and defined as cluster B_{sd} for strong descent) and less than 100 hPa in 48 h (blue colours in Fig. 6.4a and defined as cluster B_{wd} for weak descent). Compared to B_{sd}, trajectories in cluster B_{wd} exhibit lower temperature increases, but to some extent higher maximum diabatic heating. As a result, air parcels in B_{wd} are mainly

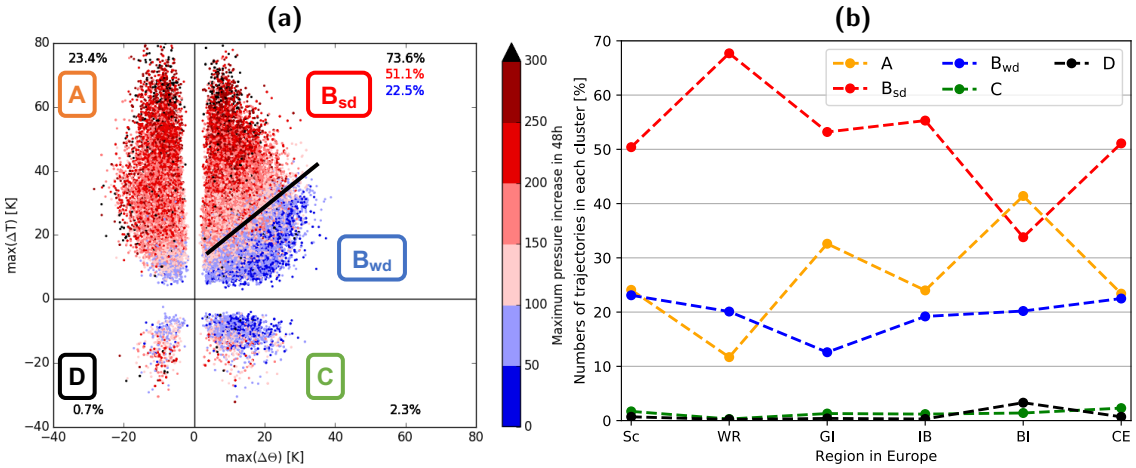

Figure 6.4: Thermodynamic changes for the trajectory clusters. (a): Maximum temperature (ΔT_{max}, in K) and maximum potential temperature ($\Delta\theta_{\text{max}}$, in K) changes along the trajectories for heat waves in Central Europe. The colours indicate the maximum pressure increase in a 48-hour window. The numbers in the quadrants denote the fraction of trajectories in each cluster: in black (irrespective of descend rate), in blue (descent $\leq$ 100 hPa in 48 h, only upper right quadrant), in red (descent $>$ 100 hPa in 48 h, only upper right quadrant). Additionally, the letters in boxes indicate the names of the clusters and the black sloping line denotes the approximate border between clusters B_{sd} and B_{wd}. (b): Fraction of trajectories in the clusters for all investigated regions in Europe (Sc: Scandinavia, WR: western Russia, GI: Greece/Italy, IB: Iberian Peninsula, BI: British Isles, CE: Central Europe). Figure taken from Zschenderlein et al. (2019). © The authors and John Wiley & Sons Ltd, CC-BY.

warmed due to diabatic heating in absence of strong vertical motion, whereas air parcels in B_{sd} are warmed due to the combination of strong subsidence and diabatic heating near the surface.

Trajectories in the lower right quadrant of Fig. 6.4a experience an overall temperature decrease and diabatic heating (cluster C) and trajectories in the lower left quadrant of Fig. 6.4a are also overall cooled but they are diabatically cooled (cluster D). Comparing the numbers of trajectories of clusters C and D to the above mentioned clusters A, B_{sd} and B_{wd} it is found that they are negligible and are therefore not discussed further.

As it has been shown, mainly three trajectory clusters with coherent thermodynamic characteristics and vertical motions create heat waves in Central Europe. In the other European regions, clusters C and D are negligibly small (Fig. 6.4b) as well. But the other three clusters A, B_{sd} and B_{wd} all contribute to heat waves, with varying importance depending on the region. In most of the regions, 50 % of the trajectories are in cluster B_{sd}, but the largest difference are found for western Russia and the British Isles. Western Russia is strongly influenced by cluster B_{sd} (about 70 %), i.e. a combination of subsidence and diabatic heating and less influenced by cluster A (about 10 %), hence the majority

of the air parcels are diabatically heated. The British Isles have the largest portion of trajectories in cluster *A* (about 40 %) compared to the other regions, where between 25 and 30 % of the trajectories fall into cluster *A*. The fraction of cluster B_{wd} does not vary that much between the regions, only Greece/Italy show a smaller fraction. Possible causes for the inter-regional differences are discussed in the next sections.

6.5 Physical processes along the trajectory clusters

Figure 6.5 depicts the source regions three and seven days prior to the heat waves. Seven days prior to the heat waves, air parcels often originate from the west, i.e. above the North Atlantic Ocean, which is reasonable given the climatic westerly flow towards Europe. Western Russia is the only exception because it is partly beyond the direct reach of the Jet Stream and the systems of North Atlantic origin. Here, trajectories originate mostly over the Eurasian continent and less over the North Atlantic Ocean. For heat waves in Scandinavia, nearly no trajectory originates in the Mediterranean, which suggests that warm air advection from typically warm regions is of minor importance for heat waves in Scandinavia. It is therefore also possible that air parcels originate from climatologically cold areas polewards of the polar circle and later contribute to the heat wave. The results are in marked contrast to the view that heat waves in Europe are associated with warm air advection from southerly regions, e.g. Perkins (2015), Miralles et al. (2014). Hence the (Lagrangian) processes in the air parcels seem to be very important for establishing high temperatures near the surface, as discussed in the following.

Air parcels in trajectory cluster *A* originate from the highest altitudes (Fig. 6.6a) and descend with a similar rate ten to five days prior to the heat waves. In the second five days the rate of descent increases, particularly for Greece/Italy, western Russia and the Iberian Peninsula, before the air parcels are entrained into the planetary boundary layer. The subsidence in the free atmosphere concurs with radiative cooling in all regions (Fig. 6.6c). Although the air parcels are diabatically cooled, their temperature increases (Fig. 6.6c) because the subsidence leads to adiabatic warming, which overcompensates the diabatic cooling. Interestingly, temperatures in the source region of cluster *A* arriving in Greece/Italy, Central Europe, western Russia and the Iberian Peninsula are colder than those for the British Isles, but the temperatures near the surface are higher for the four former regions highlighting the importance of subsidence. As mentioned by Bieli et al. (2015), temperature extremes develop on a time-scale between two and three days. Figure 6.5 therefore shows the position of the three clusters three days prior to the heat waves. Most of the trajectories in cluster *A* are already located in the target region in the last three days. Western Russia is the only exception, where cluster *A* is located to the east of the

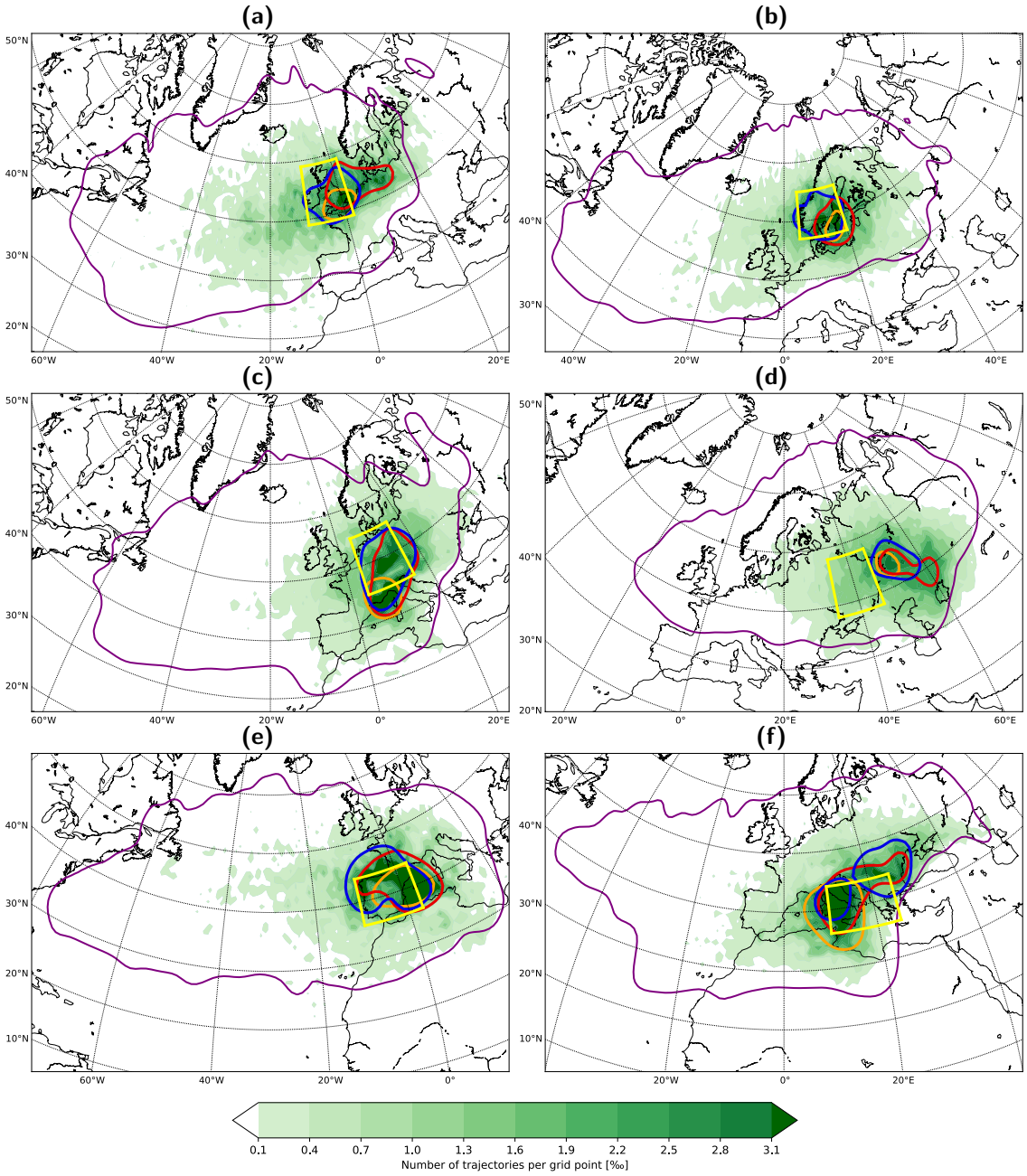

Figure 6.5: Spatial distribution of trajectories. The purple line represents the fraction of air parcels per grid point of at least 0.1‰ seven days prior to the heat waves irrespective of the clusters. The green colour shading represents the position of air parcels three days prior to the arrival in the heat wave regions: (a) British Isles, (b) Scandinavia, (c) Central Europe, (d) western Russia, (e) Iberian Peninsula and (f) Greece/Italy. The orange line represents the fraction of trajectories per grid point of at least 2.2 ‰ for cluster A, the red line for cluster B_{sd} and the blue line for cluster B_{wd} three days prior to the heat waves. Figure taken from Zschenderlein et al. (2019). © The authors and John Wiley & Sons Ltd, CC-BY.

target area. Air masses seem to be trapped in the target regions while descending. Hence subsidence above the target area or in the vicinity is essential in determining the extreme

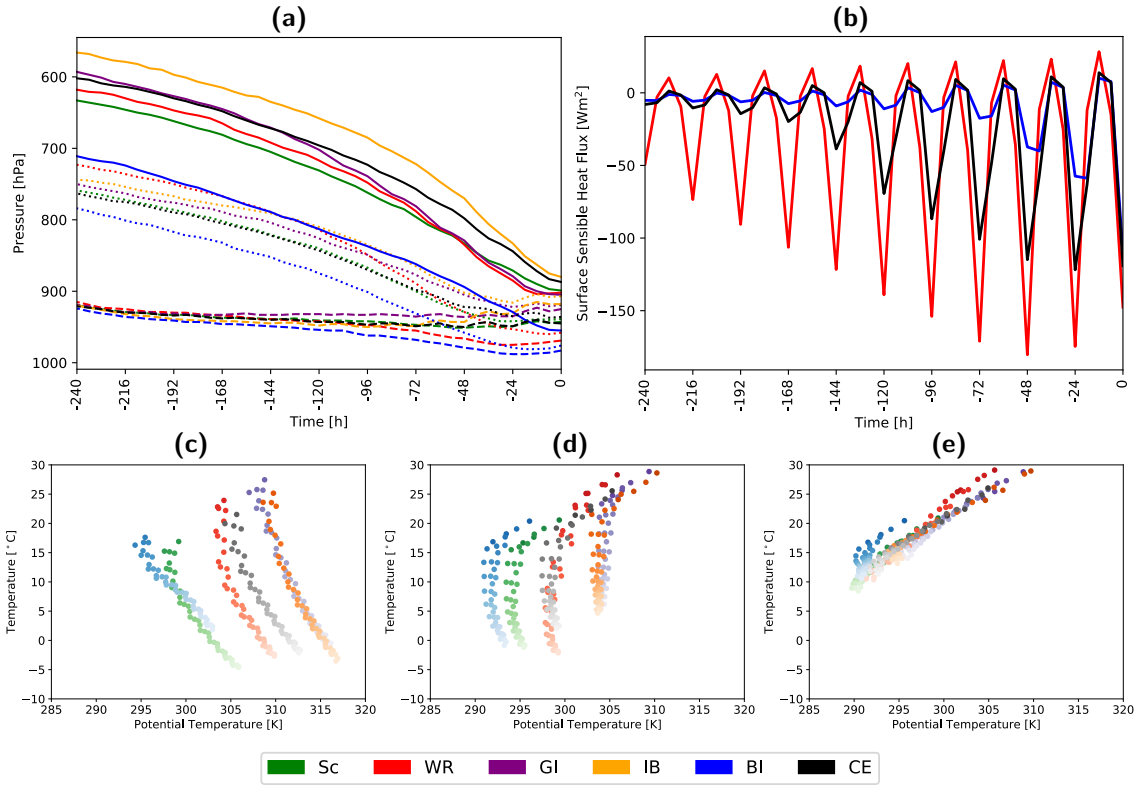

Figure 6.6: Processes along the trajectories for Scandinavia (Sc), western Russia (WR), Greece/Italy (GI), Iberian Peninsula (IB), British Isles (BI) and Central Europe (CE). (a): Temporal evolution of the median of pressure for the three trajectory clusters: A (solid); B_{sd} (dotted) and B_{wd} (dashed). (b): surface sensible heat fluxes (median) for trajectories in cluster B_{sd} and B_{wd} together, but with the additional constraint to be located between the surface and 850 hPa. For better visibility, only three regions that represent the typical characteristics are shown. (c-e): T-θ diagrams (cf. section 4.5) illustrating the temporal evolution of (median) temperature and potential temperature for the three trajectory clusters A (c), B_{sd} (d) and B_{wd} (e). Darker colours denotes time steps closer to the heat wave. Figure taken from Zschenderlein et al. (2019). © The authors and John Wiley & Sons Ltd, CC-BY.

temperatures near the surface for cluster A.

Air parcels in trajectory cluster B_{sd} descend ten to two days before their arrival in the heat wave regions similar to cluster A, but with the difference that B_{sd} trajectories enter the planetary boundary layer earlier (Fig. 6.6a). In the free atmosphere, subsidence is associated with weak radiative cooling or is nearly adiabatic for B_{sd} trajectories arriving in Greece/Italy and the Iberian Peninsula (Fig. 6.6d). During the last 72 h, B_{sd} trajectories are warmed diabatically near the surface (Fig. 6.6d). Air parcels in trajectory cluster B_{wd} remain in the lower troposphere around 950 hPa over the whole ten days (Fig. 6.6a) and are continuously warmed diabatically (Fig. 6.6e). The quasi linear relationship between temperature and potential temperature increase in this cluster suggests that the air parcels

are warmed only due to diabatic processes. While the origin temperatures of cluster B_{wd} are higher compared to the other two clusters, the overall temperature increase is smaller due to the missing subsidence.

Increased solar radiation during clear-sky conditions leads to an increase of surface sensible heat fluxes (Alexander, 2011), thus warming the air parcels near the surface diabatically. It is therefore interesting to look at the trajectories that are heated diabatically and located near the surface. Figure 6.6b illustrates the temporal evolution of the median of the surface sensible heat fluxes for the clusters B_{sd} and B_{wd} together. Because surface sensible heat fluxes are by definition only effective in the lower troposphere, the surface sensible heat fluxes in Fig. 6.6b are only shown for trajectories located between the surface and 850 hPa.

Air parcels contributing to a heat wave in western Russia are strongly influenced by surface sensible heat fluxes in the last three days before the onset of the heat wave with maximum values around 175 $\mathrm{W\,m^{-2}}$. Even up to seven days prior to the heat waves, air parcels located near the surface are influenced by a diabatic heating above 100 $\mathrm{W\,m^{-2}}$. Indeed, trajectories in clusters B_{sd} and B_{wd} are located to the east of western Russia and above land surfaces (Fig. 6.5d). Consequently, remote surface conditions are important in determining high temperatures near the surface in western Russia. The smallest influence of surface sensible heat fluxes is visible for trajectories arriving in the British Isles (blue line in Fig. 6.6b). Both the daily magnitude and the number of days with notable surface fluxes is decreased compared to the other regions. Although some trajectories in cluster B_{sd} reaching the British Isles are located above parts of Germany, Denmark, Poland and the Netherlands (Fig. 6.5a), the influence of surface sensible heat fluxes over these countries is negligible and local surface heating over the British Isles is more important. Surface fluxes for Central Europe are in between the two mentioned cases, i.e. increased surfaces fluxes five days before arrival with a median maximum daily heating around 125 $\mathrm{W\,m^{-2}}$ (Fig. 6.6b). As shown in Fig. 6.5c, most air parcels of clusters B_{sd} and B_{wd} are already located over Central Europe three days prior to the heat waves, highlighting the importance of local soil conditions and in situ warming, in agreement with Bieli et al. (2015). The Iberian Peninsula shows a similar temporal development of the surface sensible heat fluxes to the British Isles, but higher in magnitude (not shown). Because most of the trajectories are situated above the Mediterranean Sea and the Gulf of Biscay three days before the heat waves in the Iberian Peninsula (Fig. 6.5e), the influence of surface fluxes is only present one to two days before the events. Surface sensible heat fluxes for Greece/Italy are similar to western Russia and for Scandinavia they are similar to Central Europe, but trajectories for Greece/Italy and Scandinavia experience lower absolute surface fluxes (not shown). However, an interesting feature emerges for the position of the three clusters three days before heat waves in Greece/Italy (Fig. 6.5f). While cluster

A is located mostly in the western half or slightly west of the target area, clusters B_{sd} and B_{wd} trajectories are also located to the northeast of Greece/Italy. Remote surface conditions are therefore important for high near-surface temperatures in Greece/Italy, similar to western Russia. Hence, not only local but also remote surface conditions seem to play an important role in establishing high surface temperatures for some regions in Europe.

The evolution of the relative and specific humidity of air parcels for the two contrasting regions western Russia and the British Isles are depicted in Fig. 6.7. Specific humidities near the origin of clusters A and B_{sd} are low with values of about $2\,\mathrm{g\,kg^{-1}}$ (Fig. 6.7b) due to the high altitudes. Throughout the descent, specific humidity steadily increases up to values around $8\,\mathrm{g\,kg^{-1}}$. Due to the location in the lower troposphere, specific humidities of cluster B_{wd} are considerably higher and reveal a diurnal cycle for trajectories arriving in western Russia (Fig. 6.7b). This strong diurnal cycle is not found for trajectories in cluster A because they are located at higher altitudes. Compared to the specific humidity, the diurnal cycle is more pronounced for the relative humidity due to the higher correlation with temperature. Although the specific humidity increases, the relative humidity decreases substantially especially during the second half of the trajectories (Fig. 6.7a). This highlights the pronounced warming in the last days, as mentioned by Santos et al. (2015) for heat waves in the Iberian Peninsula. The strong reduction of the relative humidity is marked for clusters B_{sd} and B_{wd} and stronger for western Russia compared to the British Isles.

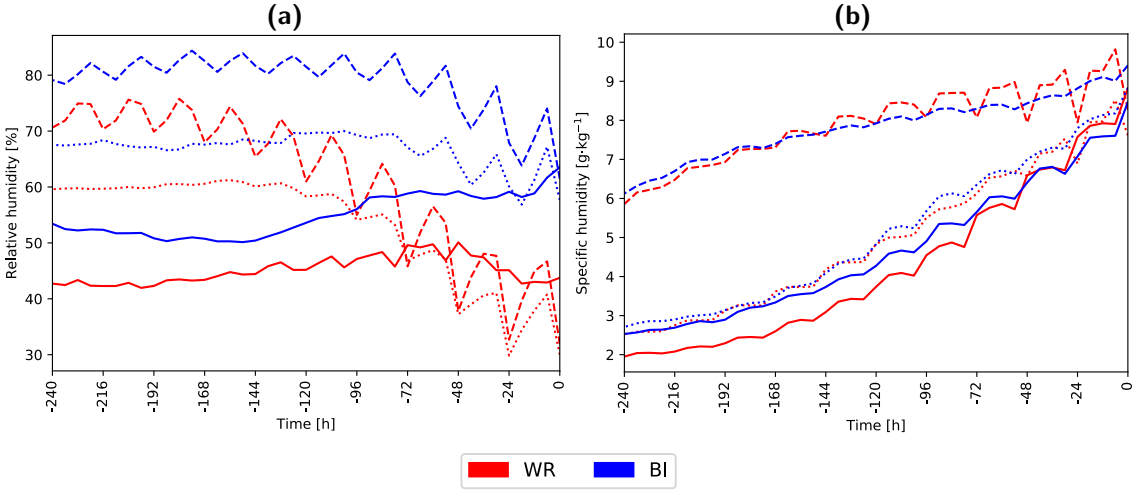

Figure 6.7: Temporal evolution of the median relative humidity (a) and specific humidity (b) for heat wave trajectories from the British Isles (BI) and western Russia (WR). Solid lines: trajectory cluster A, dotted lines: B_{sd} and dashed lines: B_{wd}. Figure taken from Zschenderlein et al. (2019). © The authors and John Wiley & Sons Ltd, CC-BY.

To summarise, most of the trajectories are already in the target regions three days prior their arrival. Additionally, not only local, but also remote surface conditions are

important in determining high temperatures near the surface. Interestingly, the origin of air parcels forming a heat wave are very diverse. The geographic origin - and therefore the original temperature - is of minor importance. Rather more important are the pathway and the processes, i.e. subsidence and diabatic heating, along the trajectories. In all regions, three air streams with different thermodynamic characteristics and vertical motions are converging in the heat wave regions: (i) air parcels originating from pressure levels around 600 hPa with temperatures mostly below the freezing level, which are warmed due to subsidence only (cluster *A*), (ii) air parcels originating from around 750 hPa, experiencing subsidence in the first eight days and being strongly heated diabatically near the surface in the last two days prior to the heat wave (cluster B_{sd}) and (iii) air parcels located in the lower troposphere during the whole ten-day period that are strongly influenced by surface sensible heat fluxes (cluster B_{wd}).

6.6 Quantification of processes

In order to quantify the most dominant process contributing to heat waves, the horizontal temperature advection at 850 hPa is derived for all heat wave days and the daily temperature change of air parcels due to vertical motion and diabatic processes for the three clusters (Lagrangian processes). The latter two processes are quantified following Eq. 2.12 (section 2.2.4).

Figure 6.8 depicts the temperature increases for the three trajectory clusters and two time periods: (i) 72 h (3 days) prior to the arrival of the air parcels in the target area (Figs. 6.8a-c) and (ii) between ten and three days prior to their arrival (Figs. 6.8d-f). This separation is motivated by Bieli et al. (2015) because they determined that extreme temperature events develop on a two to three day time scale.

Adiabatic warming due to vertical motion is much stronger than the diabatic processes for the air parcels in cluster *A* (Figs. 6.8a,d). The mean diabatic cooling rates between ten and three days before the heat waves are around -1 K per day (Fig. 6.8d), which is common for radiative cooling (e.g. Wallace and Hobbs, 2006). The warming due to subsidence strongly increases 72 h before the extreme events with a maximum over the Iberian Peninsula of around 5 K per day in the mean and even up to 8 K per day along individual trajectories. The least warming due to subsidence occurs for the British Isles (around 3 K per day). Although the warming due to subsidence appears to be modest for the British Isles, it has been shown before that cluster *A* contains the largest fraction of trajectories for this region (Fig. 6.4b).

Air parcels in cluster B_{sd} are mainly warmed due to adiabatic processes in the first seven days (Fig. 6.8e). However, the influence of diabatic processes, i.e. surface sensible

heat fluxes, increases 72 h before the heat waves (Fig. 6.8b). Therefore, the temperature increase 72 h before the heat waves is due to subsidence and diabatic warming in equal parts at a rate of about +1.5 K per day each.

In cluster B_{wd} the daily temperature increase is comparably weak in the first seven days due to the weak subsidence and diabatic warming (Fig. 6.8f). Thus, those air parcels are transported near the surface without any notable temperature changes. But 72 h before the heat events, the diabatic warming increases greatly, especially over the Iberian Peninsula at a rate of about +4 K per day, sometimes even up to 6 K per day (Fig. 6.8c). Interestingly, air parcels typically ascend during this period, which may be induced by a heat low that establishes during extremely high temperatures over the Iberian peninsula (Santos et al., 2015). Due to the ascent, air parcels cool adiabatically by up to -2 K per day, but due to the strong diabatic warming near the surface, the warming of the air parcels predominates.

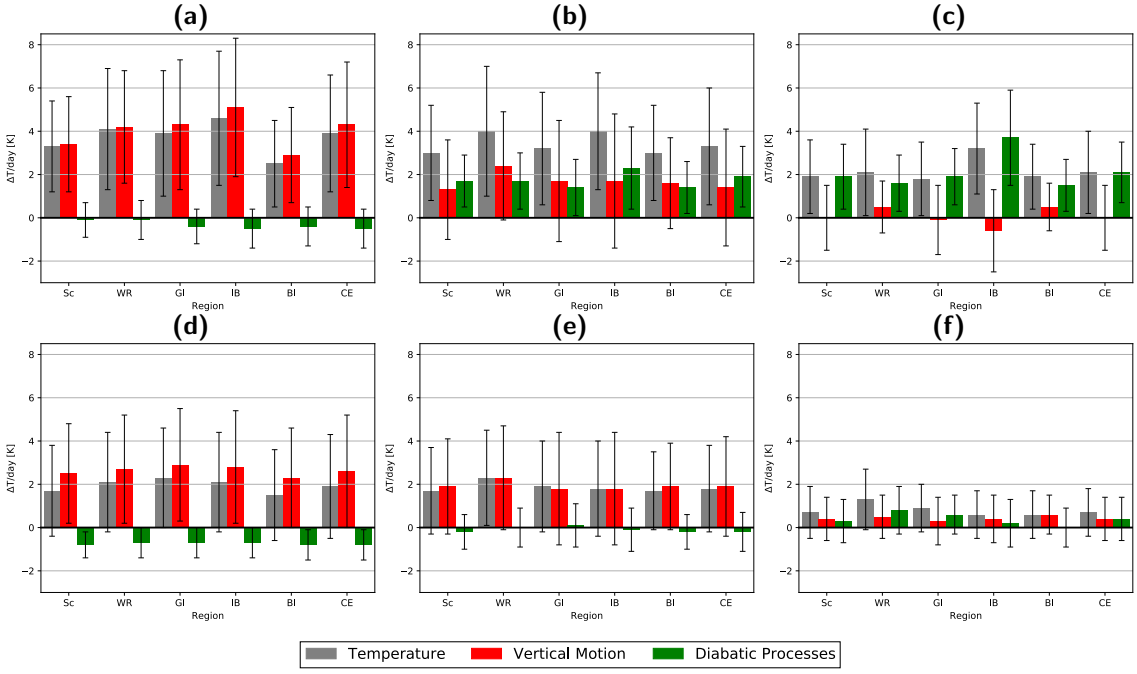

Figure 6.8: Daily Lagrangian temperature changes in K (grey: total temperature tendency, red: adiabatic temperature change due to vertical motion, green: diabatic temperature changes) for Scandinavia (Sc), western Russia (WR), Greece/Italy (GI), Iberian Peninsula (IB), British Isles (BI) and Central Europe (CE). Top row: temperature changes three days before the heat waves, bottom row: temperature changes between day ten and three before the heat waves. Left: Trajectory cluster *A*, Middle: Trajectory cluster B_{sd} and right: Trajectory cluster B_{wd}. The bars denote the mean, the errors bars the standard deviation. Figure taken from Zschenderlein et al. (2019). © The authors and John Wiley & Sons Ltd, CC-BY.

The third process, namely horizontal temperature advection is illustrated in Fig. 6.9. The Eulerian horizontal temperature advection $\vec{v} \cdot \vec{\nabla}_h T$ is calculated at a pressure level

of 850 hPa at grid points that are affected by a heat wave. For calculating the temperature advection, all available time steps from ERA-Interim at 00, 06, 12 and 18 UTC are used. Figure 6.9 shows that, although some warm air advection occurs for the British Isles and western Russia, generally local horizontal temperature advection is not important to elevate near-surface temperatures during heat waves. The warm air advection over the British Isles may be related to the fact that the ridge axis is not exactly located above the region (Fig. 6.3a). This is also the reason why some air parcels originate from the west and southwest (Fig. 6.5a). However, comparing the temperature tendencies between the advection and the two Lagrangian processes, it is obvious that the latter are pivotal.

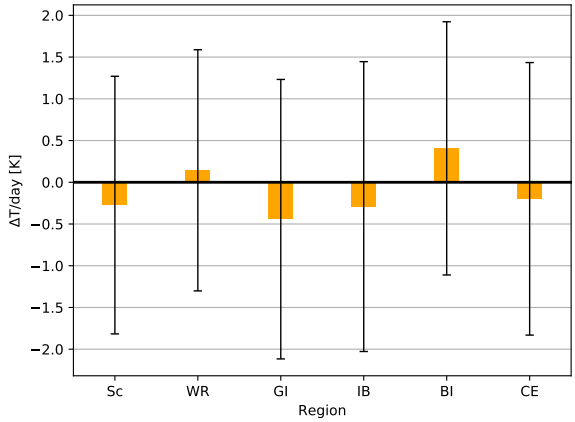

Figure 6.9: Horizontal temperature advection at 850 hPa at 00, 06, 12 and 18 UTC for heat waves in Scandinavia (Sc), western Russia (WR), Greece/Italy (GI), Iberian Peninsula (IB), British Isles (BI) and Central Europe (CE). The bars denote the mean, the error bars the standard deviation. Figure taken from Zschenderlein et al. (2019). © The authors and John Wiley & Sons Ltd, CC-BY.

6.7 Residence time of air parcels

In order to quantify how long the air parcels, which lead to the high near-surface temperatures, are stalled in the target region (circles with 500 km radius as described in section 6.1), forward trajectories are calculated for the heat waves and it is determined when the trajectories exit the region. The longer the air parcels are located in the lower troposphere, the higher is the potential influence of land-atmospheric feedbacks. During mega-heat waves, previous studies suggested that the heat can be stored over several days resulting in a progressive accumulation of heat (Miralles et al., 2014). The authors highlighted the multi-day memory of land-surface feedbacks in the planetary boundary layer. With the help of forward trajectories it is tried to quantify how often trajectories are being trapped in the heat wave area for multiple days. Figure 6.10 shows the residence time of the trajectories. The shortest (median) residence time is found for western Russia and the

British Isles, while the longest is found for Central Europe and Scandinavia (around 1.5 days). Although there are also cases of longer residence times in all regions, most of the trajectories are in the target region between 0.5 and 2.5 days only. Due to the minimum duration of three days for heat waves, air masses are therefore steadily descending into the heat wave areas (presumably trajectory cluster A) or transported horizontally from adjacent regions (presumably trajectory clusters B_{sd} and B_{wd}). Hence, hot air masses are mostly not stagnant over a time period longer than a few days. For the extreme heat waves in Central Europe in 2003 and western Russia in 2010, similar median residence times of 30 h for Central Europe (Fig. A1.8) and 24 h for western Russia (Fig. A1.9) are found, underlying the importance of the Lagrangian processes mentioned above. It is generally possible that air parcels can re-enter the target area after exiting the region which may happen in a blocking anticyclone with recirculating air masses. About 10-15 % of the trajectories are re-entering the target area within a ten-day period. Hence, although the synoptic pattern is nearly stationary during heat wave periods due to the low variability of the associated ridges above the areas (Fig. 6.3), the involved air masses leading to extreme temperatures are mostly not stationary. In that sense, new air masses that experience subsidence in the free atmosphere and diabatic heating near the surface replace the old air mass.

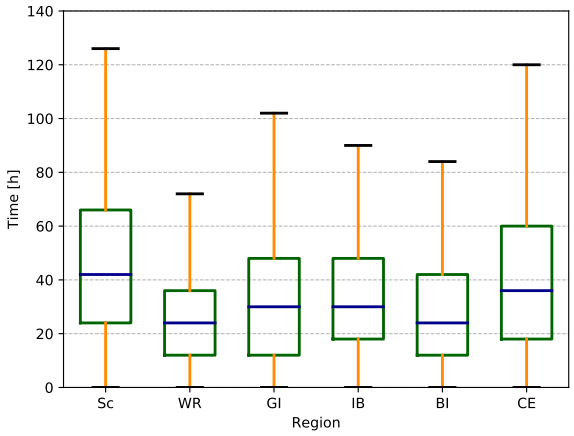

Figure 6.10: Residence time of the trajectories in the target regions for heat waves in Scandinavia (Sc), western Russia (WR), Greece/Italy (GI), Iberian Peninsula (IB), British Isles (BI) and Central Europe (CE). The blue lines depict the median, the boxes the interquartile range (IQR) and the whiskers 1.5·IQR. Figure taken from Zschenderlein et al. (2019).

Chapter 7

Processes leading to upper-tropospheric anticyclones

This chapter analyses the processes leading to the formation and maintenance of upper-tropospheric anticyclones associated with heat waves at the surface in different European regions. Section 7.1 provides an overview of the methods employed in this study. Then, section 7.2 presents the origin of trajectories reaching upper-tropospheric anticyclones. Subsequently, section 7.3 discusses, for different regions in Europe, the influence of diabatic heating on these trajectories. Furthermore, locations of strong diabatic heating and their synoptic environments are presented in section 7.4. The last results section 7.5 describes the influence of diabatic heating during the life cycle of the heat wave anticyclone.

7.1 Methods

This section firstly describes the identification of upper-tropospheric anticyclones and their connection to the heat waves at the surface. Secondly, the calculation of the trajectories and the identification of diabatic processes are outlined. To be consistent with the last chapter, the period between 1979 and 2016 is used.

7.1.1 Identification of upper-tropospheric anticyclones

We aim to assign the surface heat waves in the six European regions (dashed boxes in Fig. 7.1b) used in the previous Chapter to upper-tropospheric anticyclones. As an example, 73 heat waves were identified for Central Europe. In order to define upper-tropospheric anticyclones, a PV-approach introduced by Schwierz et al. (2004) that is based on the anomaly of the instantaneous, vertically averaged PV between 500 and 150 hPa with respect to the monthly climatology is used. To be identified as an upper-

tropospheric anticyclone, the PV anomaly at a grid point must fall below -0.7 PVU (1 PVU = 10^{-6} K kg^{-1} m^2 s^{-1}). Pfahl and Wernli (2012) used this threshold for the definition of weak blocking and demonstrated that the link between weak blocking and northern hemispheric warm temperature extremes is particularly robust. We therefore choose the -0.7 PVU threshold for defining upper-tropospheric anticyclones. Note that our definition of upper-tropospheric anticyclones requires no temporal persistence in contrast to Schwierz et al. (2004) and is only constrained by the duration of the surface heat waves (at least 3 days).

In a second step, upper-tropospheric anticyclones are assigned to the respective region. Exemplarily for Central Europe, Fig. 7.1a depicts a composite of the vertically averaged PV anomaly for all heat wave days. The composite shows a negative upper-tropospheric PV anomaly with small standard deviations over Central Europe. In order to study the formation of the corresponding anticyclones, a rectangular box enclosing the -0.5 PVU contour line in the composite (black solid box in Fig. 7.1a) is defined and we assign all upper-tropospheric negative PV anomalies in this box to heat waves in Central Europe. The respective boxes for the other regions are shown in Fig. 7.1b. All grid points with PV anomalies below -0.7 PVU in the respective box during heat wave days in the corresponding region (dashed boxes in Fig. 7.1b) are identified as upper-tropospheric anticyclones.

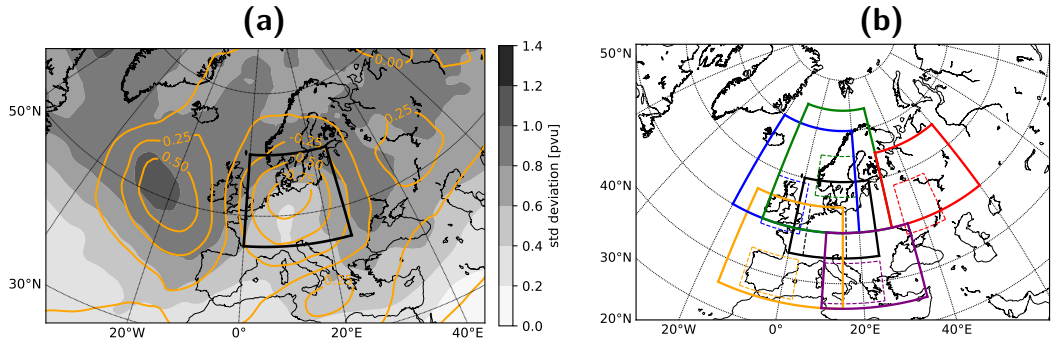

Figure 7.1: Identification of upper-tropospheric anticyclones. (a): Composite of the instantaneous, vertically averaged PV anomalies (VIPa) for all heat wave days in Central Europe. The contours show the mean of VIPa (in PVU) and the shading shows the standard deviation of VIPa. (b): The solid boxes depict the regions where the upper-tropospheric PV anomalies are assigned to heat waves at the surface and the dashed boxes show the regions of the heat waves as defined in Chapter 6: Scandinavia (green), western Russia (red), Greece/Italy (purple), Iberian Peninsula (orange), Central Europe (black, also in (a)) and the British Isles (blue). Figure taken from Zschenderlein et al. (2020).

7.1.2 Backward trajectories

Seven-day backward trajectories, driven by three-dimensional ERA-Interim wind fields on 60 vertical model levels, are calculated at each six-hourly time step with LAGRANTO (Sprenger and Wernli, 2015) for every heat wave day. Trajectories are initialised in the upper-tropospheric anticyclone and started from an equidistant grid (Δx=100 km horizontally) and vertically between 500 and 150 hPa every 50 hPa with the additional criterion that the PV at the respective level must be less than 1 PVU. The latter excludes starting points in the stratosphere, similar to Steinfeld and Pfahl (2019). Physical parameters traced along the trajectories include temperature and potential temperature. The total number of trajectories is between 700,000 for Greece/Italy and nearly 2,000,000 for Scandinavia.

In order to quantify diabatic processes along the trajectories, it has to be evaluated whether diabatic heating or cooling dominates. For that, we calculate the highest (θ_{max}) and lowest potential temperature (θ_{min}) along the backward trajectories over a three or seven day period. Diabatic heating is calculated as the difference ($\Delta\theta$) between θ_{max} and the preceding, i.e. closer to the origin, potential temperature minimum, whereas diabatic cooling is quantified as the difference ($\Delta\theta$) between θ_{min} and the preceding potential temperature maximum. If the diabatic heating exceeds the absolute value of the diabatic cooling, the trajectory belongs to the heating branch and vice versa. If the magnitude of diabatic cooling and heating are equal, the trajectory will be sorted in the cooling branch. This approach is similar to Steinfeld and Pfahl (2019), with the difference that in their study all trajectories heated by more than 2 K are categorised as "diabatically heated", no matter how large the diabatic cooling is.

Figure 7.2 shows an example for a three-day period: the backward trajectory in Fig. 7.2a experiences stronger diabatic heating (red arrow in Fig. 7.2a) than cooling (blue arrow in Fig. 7.2a) and therefore belongs to the heating branch, whereas in Fig. 7.2b the diabatic cooling dominates and the trajectory is consequently sorted in the cooling branch.

7.1.3 Feature composites

To explore in which synoptic environment the air parcels in the heating branch are diabatically heated, composites of various features centred around the location of maximum diabatic heating are created. PV at 330 K, wind at 800 hPa, mixed-layer convective available potential energy (ML CAPE) and convective and large-scale precipitation are shown. Whereas convective precipitation in ERA-Interim comes from the parameterised shallow, mid-level and deep convection, large-scale, i.e. stratiform, precipitation denotes the con-

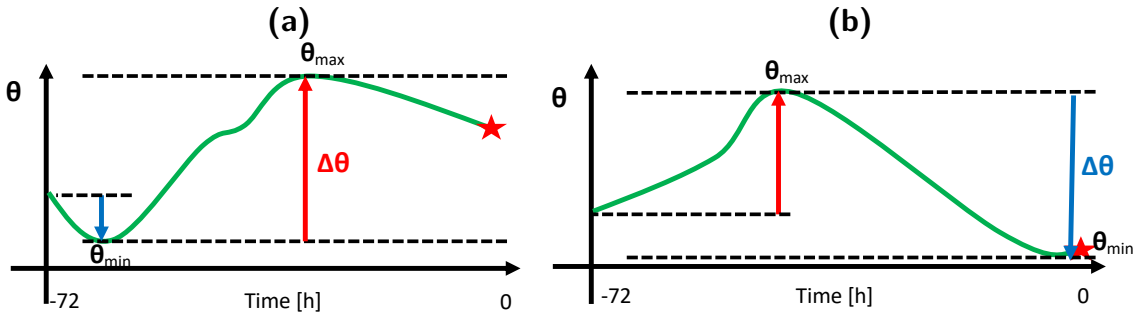

Figure 7.2: This schematic depicts the potential temperature change $\Delta\theta$ for a three-day period. The red star indicates the starting point of the backward trajectory. (a): Diabatic heating (red arrow) exceeds diabatic cooling (blue arrow). (b): diabatic cooling exceeds diabatic heating. Figure taken from Zschenderlein et al. (2020).

tribution coming from the cloud scheme (Dee et al., 2011). Flow features, i.e. blocks, cyclones and warm conveyor belts, are taken from Sprenger et al. (2017). In their climatology, weak atmospheric blocking is defined as a region where the anomaly of vertically averaged PV between 500 and 150 hPa is lower than -0.7 PVU and persists for at least five days (Schwierz et al., 2004; Croci-Maspoli et al., 2007). Hence, temporal persistence is required in addition to our definition of upper-level anticyclones. The region affected by a cyclone is defined as the region within the outermost closed sea level pressure isoline surrounding one or several local sea level pressure minima (Wernli and Schwierz, 2006). Warm conveyor belts are air parcel trajectories ascending more than 600 hPa in two days associated with a midlatitude cyclone (Madonna et al., 2014). A more detailed description of the three features is given in Sprenger et al. (2017). To assess, whether the occurrence of blocks, cyclones and WCBs is anomalous, the frequencies of the three features during diabatic heating are compared with their climatological frequencies. The anomaly is then defined as the difference between the observed frequency during heat wave days and the climatological frequency.

7.2 Source regions of low-PV air masses

This section focuses on the origin of trajectories started from the upper-tropospheric anticyclones. To this end, density maps of trajectory locations at specific time steps are created, which show relative frequencies and are normalised such that the spatial integral over the whole distribution yields 100%. Only the density maps for heat waves in Central Europe, western Russia and Greece/Italy are presented because they exhibit the largest differences. Results for the other three regions, viz. Iberian Peninsula, British Isles and Scandinavia are shown in the Appendix (Figs. A2.1-A2.2).

Three days prior to the arrival of the trajectories in the upper-tropospheric anticyclone over Central Europe, one part of the heating branch is located over the western North Atlantic and the other part over northwestern Africa in the middle and partly lower troposphere (Fig. 7.3a). The western North Atlantic is a typical source region of diabatically heated trajectories for the formation of atmospheric blocking, although the main source region in summer is shifted towards North America (Pfahl et al., 2015). In the blocking study by Pfahl et al. (2015), most of the backward trajectories were initialised over the North Atlantic to the west of Central Europe, which explains the westward shift of the source regions of diabatically heated trajectories compared to our study. Additionally, the western North Atlantic is the entrance region of the summer storm tracks (Dong et al., 2013) and therefore a region prone to diabatic heating. The second major source region over northwestern Africa (Fig. 7.3a) is not known as a source region for air parcels influencing the formation of blocking, presumably due to the stronger influence of oceanic blocks in other studies (e.g. Pfahl et al., 2015; Steinfeld and Pfahl, 2019), but appears to be important for the formation of summertime upper-tropospheric anticyclones in association with heat waves. Due to this separation of the heating branch into two distinct regions, trajectories in the heating branch located west and east of 30°W three days prior to the arrival in the upper-tropospheric anticyclone are analysed separately in the following and are hereafter denoted as the remote and nearby heating branch, respectively.

Air parcels in the cooling branch related to upper-tropospheric anticyclones above Central European heat waves are located in the upper troposphere at around 300-400 hPa and mostly above northwestern Africa, but also over the North Atlantic and already within the upper-level anticyclone area three days prior to their arrival (Fig. 7.3b). These air parcels are then transported northwards to Central Europe along the western flank of the ridge associated with the heat wave. Pfahl et al. (2015) showed that the majority of the air parcels not influenced by diabatic heating (comparable to our cooling branch) are, three days prior to the arrival in the block, located to the east of the diabatically heated trajectories. This is also the case here when comparing the location of the cooling with the remote heating branch (Figs. 7.3a,b).

Seven days prior to the arrival of the air parcels in the heating branch to Central Europe, most of them are located above North America and the western North Atlantic and to some extent above northwestern Africa. Compared to the three-day period, air parcels are located at lower altitudes (Fig. 7.4a). Generally, air parcels in the subtropics over the North Atlantic and Gulf of Mexico are located at lower altitudes compared to air parcels above the North American continent and towards the East Pacific. Air parcels in the cooling branch are at similar pressure levels compared to the three-day period, but more widely distributed compared to the heating branch with a maximum density above the North Atlantic (Fig. 7.4b). Similar to the three-day timescale, the major part of the

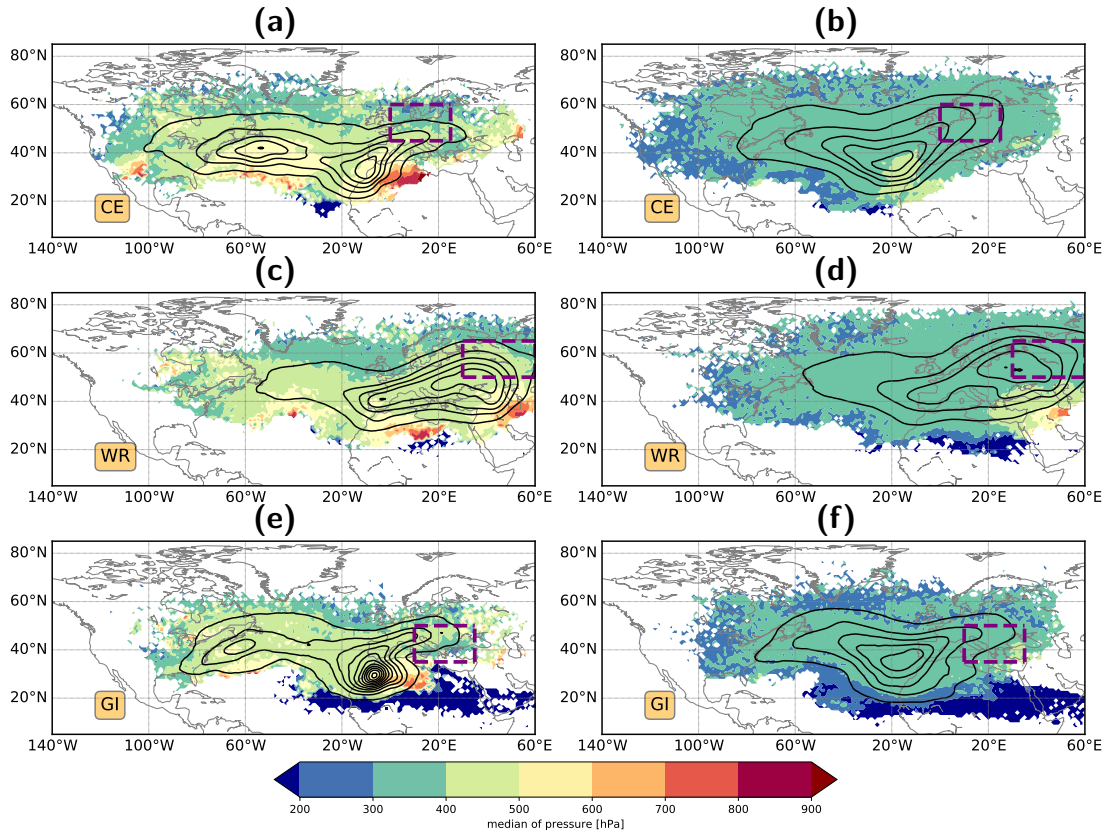

Figure 7.3: Spatial distribution of diabatically heated (left) and cooled (right) trajectories three days prior to arrival in the upper-tropospheric anticyclones for (a,b) Central Europe (CE), (c,d) western Russia (WR) and (e,f) Greece/Italy (GI). The colours indicate the median pressure of air parcels and contours display the air parcel density (starting from 1‰ per 10^5 km^2 in 2‰ increments). The dashed purple boxes represent the area in which upper-tropospheric anticyclones are associated with heat waves (cf. section 7.1.1 and Fig. 7.1b). Figure taken from Zschenderlein et al. (2020). © The authors and Copernicus Publications, CC-BY.

cooling branch is found east of the remote heating branch.

The density maps for air parcels in the heating branch reaching western Russia exhibit two distinct differences compared to Central Europe. Firstly, the source regions of the heating branch do not show two clearly separated geographical maxima on the three-day timescale (Fig. 7.3c). In fact, the major part of this branch is located above the European continent and in the middle troposphere. However, on the seven-day timescale, a pattern of two geographical maxima emerges with the highest densities over the western North Atlantic and in the Mediterranean area (Fig. 7.4c). Secondly, more air parcels are already located in the vicinity of the target upper-level anticyclone indicating that the diabatic heating can occur more locally. The overall pattern of the cooling branch, however, does not reveal substantial differences compared to the pattern for Central Europe, although the maximum densities are generally shifted to the east (Figs. 7.3d and 7.4d).

Air parcels in the heating branch reaching the upper-troposphere above Greece/Italy

predominantly originate from northwestern Africa during the last three days, in particular from the Atlas Mountains (Fig. 7.3e). Therefore, these anticyclones are strongly influenced by the nearby heating branch, whereas on the seven-day timescale, most of the diabatically heated trajectories originate from the western Atlantic and North America (Fig. 7.4e). The majority of the air parcels in the cooling branch are located above the North Atlantic three and seven days prior to the heat wave, but some trajectories are located in the tropics south of 20°N at around 200 hPa (Figs. 7.3f and 7.4f) - an area which is climatologically influenced by upper-level easterly winds in summer (Fink et al., 2017). In this region and during this time of the year, organised convection in the form of huge mesoscale convective systems occurs in the ITCZ (Inter-Tropical Convergence Zone) over the West African monsoon region. Their upper-level poleward outflow turns eastward to feed the subtropical jet over Northern Africa and the Mediterranean (cf. Fig. 1 in Lafore et al., 2010).

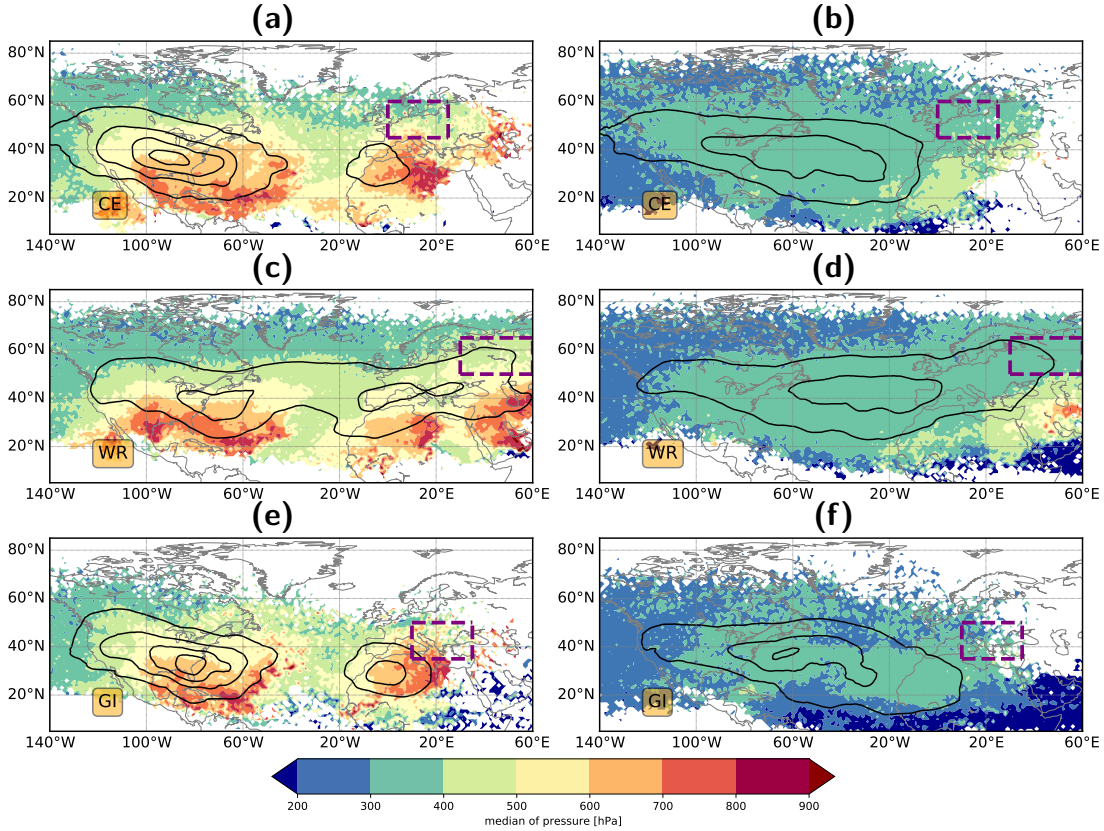

Figure 7.4: Same as Fig. 7.3, but for seven days prior to arrival. Figure taken from Zschenderlein et al. (2020). © The authors and Copernicus Publications, CC-BY.

Three days prior to the arrival of the air parcels in the heating branch over the Iberian Peninsula and the British Isles, most of them are located above the western North Atlantic in the middle and lower troposphere, but also over northwestern Africa and Spain (Figs. A2.1a,c). For Scandinavia, air parcels are located over the western North At-

lantic and southern/central Europe in nearly equal parts (Fig. A2.1e). On the seven-day time scale, air parcels of the heating branch are distributed between North America and the western Atlantic (Figs. A2.2a,c), although the dichotomy in the trajectory origin for Scandinavia still exists (Fig. A2.2e). The results for the cooling branches are qualitatively similar to the other regions (Figs. A2.1b,d and A2.2b,d,f), while for Scandinavia, a large fraction of diabatically cooled air parcels is already located in the target area three days prior to arrival (Fig. A2.1f).

7.3 Two diabatic regimes

We now compare the statistical distributions of the potential temperature changes in the heating and cooling branch. Changes in potential temperature during the last three and seven days prior to reaching upper-tropospheric anticyclones over Central Europe are shown as probability density distributions. For both the three- and seven-day period, the shape of the cooling branch features a Gaussian normal distribution, whereas the heating branch is more skewed (Fig. 7.5a). This skewness increases for the seven-day period, implying an overall higher magnitude of diabatic heating along the trajectories on this timescale. During the last three days, about 29% of the trajectories are influenced by diabatic heating and, consequently, 71% belong to the cooling branch (Fig. 7.5b). On the seven-day timescale, 42% of the trajectories are in the heating branch (Fig. 7.5b). Hence, diabatic heating along trajectories substantially influences the formation of upper-tropospheric anticyclones above Central Europe.

The majority of trajectories in the cooling branch slightly descend and are radiatively cooled in the free atmosphere, while most of the trajectories in the heating branch ascend (not shown). Overall, the diabatic heating is a more rapid process compared to the diabatic cooling (not shown). Therefore, the heating branch can be interpreted as a strongly cross-isentropic branch transporting low-PV air from the lower to the upper troposphere, whereas the cooling branch is a quasi-adiabatic process that advects low-PV air towards the upper-tropospheric anticyclone, in line with the analysis of Pfahl et al. (2015) and Steinfeld and Pfahl (2019) for blocks.

The cross-isentropic transport of low-PV air from the lower to the upper troposphere in the heating branch is stronger for western Russia. During the last three days, about 44% of the air parcels reaching upper-tropospheric anticyclones above western Russia are affected by the heating branch, which is the highest fraction among the different European regions (Fig. 7.5b). For Scandinavia and the British Isles, about 35% of the air parcels are influenced by diabatic heating, which is slightly more than for Central Europe. The Mediterranean area, i.e. Greece/Italy and the Iberian Peninsula, however, is less in-

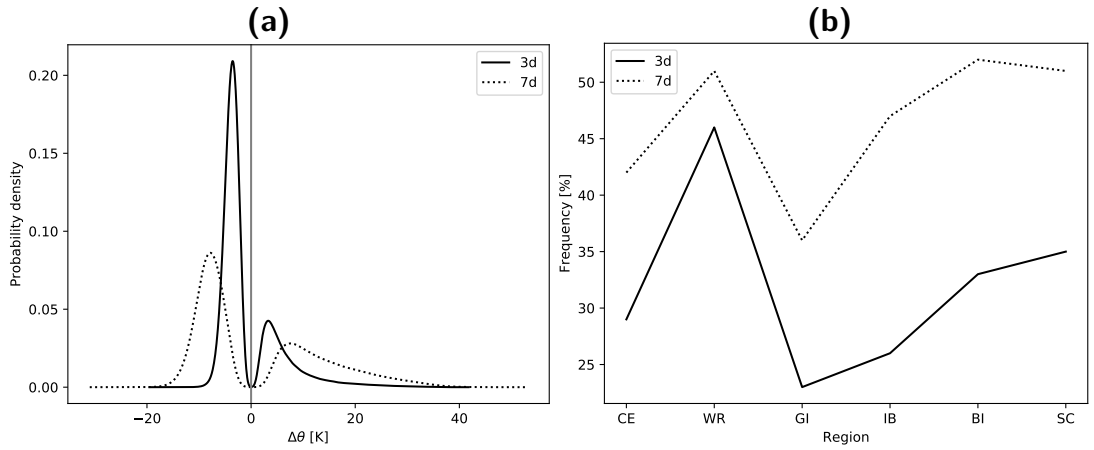

Figure 7.5: Diabatic processes in the heating and cooling branches three (solid line) and seven days (dashed line) before reaching upper-tropospheric anticyclones. (a): Probability density distribution of the potential temperature changes for air parcels reaching Central European heat wave anticyclones. The grey line denotes the 0 K border separating the heating and cooling branch. (b): Fraction of diabatically heated trajectories for all regions (CE: Central Europe, WR: western Russia, GI: Greece/Italy, IB: Iberian Peninsula, BI: British Isles and SC: Scandinavia). Figure taken from Zschenderlein et al. (2020). © The authors and Copernicus Publications, CC-BY.

fluenced by the heating branch with only about 25% of the trajectories in this branch on the three-day timescale. During the last seven days, the relevance of the heating branch increases for all regions (Fig. 7.5b). The highest influence of the heating branch (about 50%) is found for trajectories reaching upper-tropospheric anticyclones above the British Isles, Scandinavia and western Russia. Interestingly, the increase of the fraction of diabatically heated air parcels from the three- to the seven-day period is smallest for western Russia, indicating that heat wave anticyclones in western Russia are less influenced by remote diabatic heating beyond three days prior to their arrival in the anticyclone.

Comparing the fraction of diabatically heated air parcels contributing to the formation of atmospheric blocks (Pfahl et al., 2015) with our findings, we conclude that the fraction is lower in our study. This can be explained by three main reasons: firstly, weather systems that are associated with diabatic heating such as extratropical cyclones and warm conveyor belts are climatologically less frequent during summer (Madonna et al., 2014). Secondly, Pfahl et al. (2015) defined blocking with a more pronounced negative PV anomaly, and because more intense negative PV anomalies are associated with stronger latent heating in WCBs (Madonna et al., 2014), the influence of diabatically heated trajectories is reduced in our study. Thirdly, the quantification of diabatic heating along trajectories of Pfahl et al. (2015) is slightly different, because they only quantified the contribution of diabatic heating to the formation of blocking and did not account for diabatic cooling.

7.4 Two geographically separated heating branches

In the remainder of this study, we further analyse the heating branches for heat wave anticyclones in three regions. Remember that heated trajectories located west (east) of 30°W three days prior to the arrival in the heat wave anticyclone belong to the remote (nearby) heating branches. We focus on Central Europe and Greece/Italy, which are affected by the nearby and remote heating branches (Figs. 7.3a,e), and on western Russia, which is affected predominantly by the nearby heating branch (Fig. 7.3c).

The spatial distributions of the locations of maximum diabatic heating along the trajectories for the nearby and remote heating branches are shown in Fig. 7.6. These locations are defined as the geographical positions at the end of the maximum 6-h increase of potential temperature in the last three days prior to reaching the upper-level anticyclones. The remote heating branch associated with anticyclones above Central Europe accounts for 50% of the whole heating branch. Most of its diabatic heating occurs over the central North Atlantic between 40°-50°N and 20°-40°W (Fig. 7.6a). Air parcels in the nearby heating branch are diabatically heated over the European continent in a similar latitude band (Fig. 7.6b). For western Russia, only 8% of the heated trajectories are in the remote branch and the strongest diabatic heating occurs over the North Atlantic, but also over Central Europe (Fig. 7.6c). The dominant heating branch reaching western Russia is the nearby heating branch (92%, Fig. 7.6d). Most of the diabatic heating in this branch occurs over the European continent and mostly in the target area between 50° and 60°N. For Greece/Italy, 69 (31)% of the heated trajectories are assigned to the nearby (remote) heating branch. Air parcels in the remote heating branch experience diabatic heating over the western North Atlantic (Fig. 7.6e). Local maxima of diabatic heating in the nearby heating branch occur above the Atlas Mountains and the Alps (Fig. 7.6f), suggesting the importance of orographic ascent for the formation of upper-tropospheric anticyclones in this region. Overall, most of the diabatic heating in the nearby heating branch occurs close to the target region, whereas the remote heating branch is associated with more remote diabatic heating. Most of the trajectories are diabatically heated at around 400 hPa (Fig. 7.7a), indicating that the air parcels are mostly heated due to latent heat release in clouds, as opposed to surface fluxes.

The dominant remote branch associated with anticyclones above the Iberian Peninsula and the British Isles is diabatically heated above the central North Atlantic (Figs. A2.3a,c), similar to anticyclones over Central Europe. Scandinavia is slightly more influenced by the nearby branch (Figs. A2.3e,f) and air parcels in this branch are diabatically heated above central and western Europe (Fig. A2.3f).

Although the remote and nearby heating branches are geographically separated, it may be possible that the maximum diabatic heating occurs at the same time before arrival

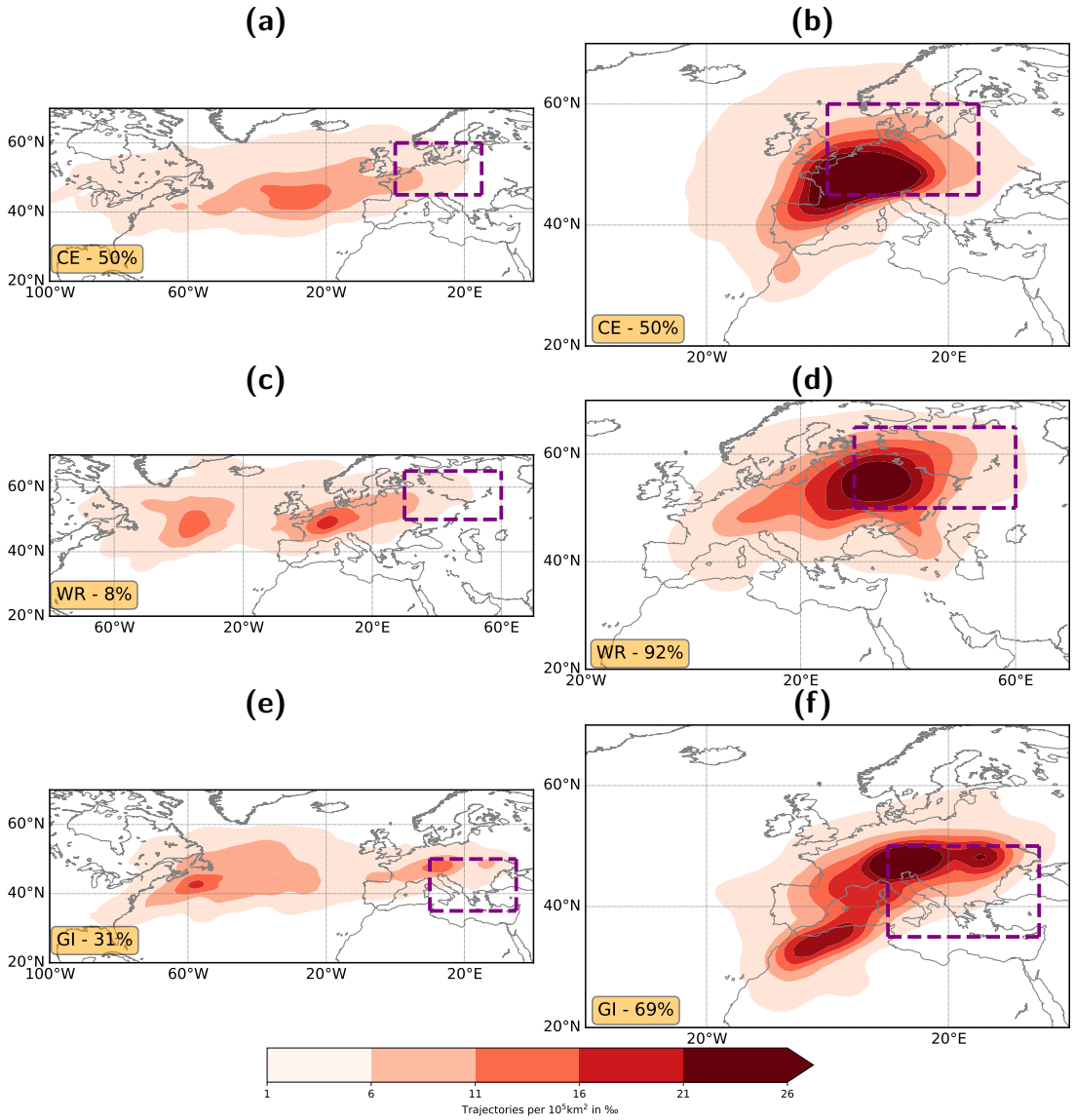

Figure 7.6: Geographic location of the maximum diabatic heating along trajectories for the remote (left column) and nearby heating branch (right column) during the last three days prior to reaching upper-tropospheric anticyclones above Central Europe (CE), western Russia (WR) and Greece/Italy (GI). The percentages in the orange boxes denote the fraction of the remote/nearby heating branch with respect to the whole heating branch. Figure taken from Zschenderlein et al. (2020).

in the upper-tropospheric anticyclone. Around 42 to 54 h prior to arrival, the remote heating branch experiences the strongest diabatic heating (Fig. 7.7b). On the contrary, trajectories in the nearby heating branch are strongly heated between 24 and 36 h prior to arrival (Fig. 7.7b). Hence, air parcels in the remote branch are heated earlier compared to the nearby branch.

To explore which synoptic systems lead to the ascent and latent heat release in the two different heating branches, composites of different fields and frequencies of blocks, cy-

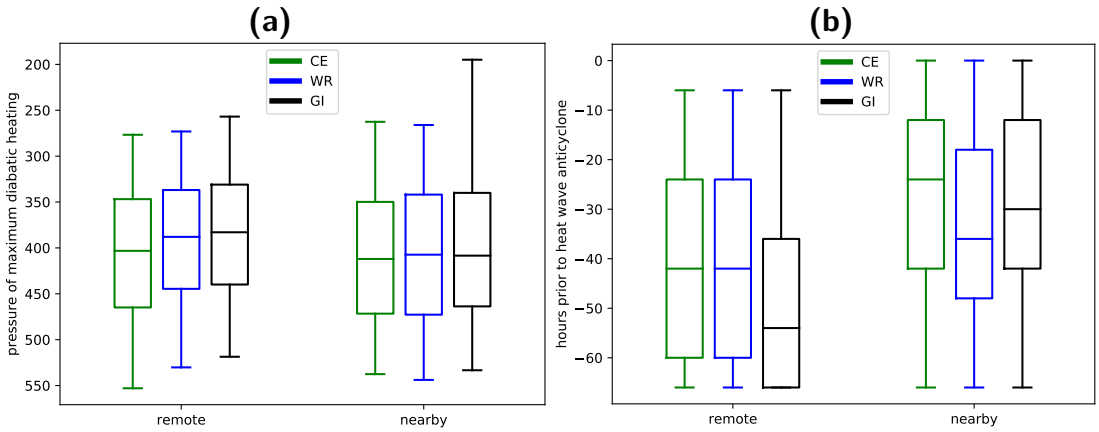

Figure 7.7: Pressure (a) and time (b) of maximum diabatic heating of trajectories in the two heating branches of the heat wave anticyclone over Central Europe (green, CE), western Russia (blue, WR) and Greece/Italy (black, GI). Horizontal lines denote the median, the boxes the interquartile range and the whiskers the 5th and 95th percentile, respectively. Figure taken from Zschenderlein et al. (2020). © The authors and Copernicus Publications, CC-BY.

clones and warm conveyor belts centred around the location of maximum diabatic heating are created. To emphasise the structure of the most pronounced heating, we only considered trajectories in the composites that are diabatically heated by more than 5 K during the last three days.

The composite for the air parcels within the remote heating branch reaching Central Europe is presented in Fig. 7.8. The upper tropospheric circulation, represented by PV at 330 K, is characterised by a trough upstream of the maximum diabatic heating (Fig. 7.8a). At the surface, extratropical cyclones are frequently located west and north of the diabatic heating maximum. The position of the extratropical cyclones west of the heating maximum is slightly east of the upper-level PV trough, which corresponds to the canonical configuration of cyclogenesis at the leading edge of an upper-tropospheric trough. In the warm sector of these cyclones, where southwesterly winds prevail (Fig. 7.8a), lifting occurs according to quasi-geostrophic forcing (Holton and Hakim, 2013). Hence, it is meaningful that warm conveyor belts are found centred around the diabatic heating maximum and downstream of the extratropical cyclones (Fig. 7.8a). These ascending air streams release latent heat and lead to an increase of potential temperature. Therefore, the remote heating branch is often influenced by cyclones in the North Atlantic storm track and latent heating in their warm conveyor belts.

Above the diabatic heating maximum, an upper-level ridge evolves and blocking frequencies are enhanced downstream (Fig. 7.8a). ML CAPE values are usually low in this branch. To the southwest of the diabatic heating maximum, ML CAPE values strongly increase due to climatologically higher sea surface temperatures in the western North Atlantic south of 30°N.

To assess, whether the occurrence of the three features in the North Atlantic region is anomalous for this time of the year, the frequencies of the three features during the diabatic heating are compared with their climatological frequencies. In general, the anomalies of all three features attain their highest values in the vicinity of or at the position of the diabatic heating maximum (Fig. 7.8b). To the west and southwest of the diabatic heating maximum, the observed cyclone frequency is about 15 percentage points higher than the climatology, which is an increase by a factor of about 1.5. In contrast, the anomalies of the cyclone frequency to the north are smaller, although the observed frequency is similar (Fig. 7.8a). As a result of the enhanced cyclone occurrence, also the existence of warm conveyor belts is anomalously high (Fig. 7.8b). In accordance with the anomalously high cyclone frequency north and northwest of the diabatic heating maximum, the blocking frequency is anomalously low in this region. Downstream of the diabatic heating maximum, the blocking frequencies are higher and the cyclone frequencies lower than climatologically expected.

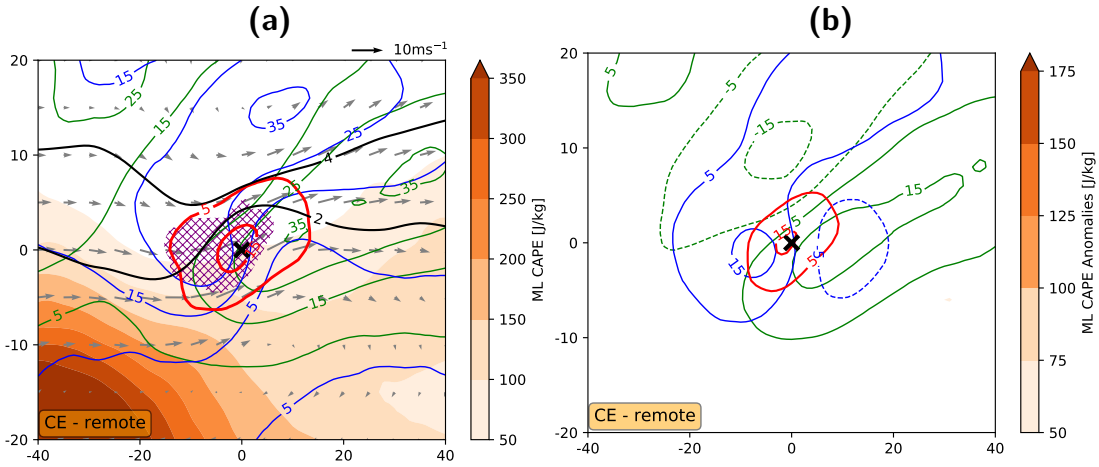

Figure 7.8: Composites centred around the position of maximum diabatic heating for the remote heating branch reaching upper-tropospheric anticyclones above Central Europe. (a): Frequencies of extratropical cyclones (blue), blocks (green) and warm conveyor belts (red) starting from 5% in 10% increments. The orange shading shows the ML CAPE (in J kg^{-1}) and the arrows the wind at 800 hPa. Black contours indicate PV (2 and 4 PVU contours) at 330 K. The purple hatching marks the region where the stratiform precipitation exceeds the convective precipitation (only for areas with total precipitation $\geq 2\,\mathrm{mm\,d^{-1}}$). (b) Anomalies of cyclone (blue), blocking (green) and warm conveyor belt (red) frequency. Figure taken from Zschenderlein et al. (2020). © The authors and Copernicus Publications, CC-BY.

Steinfeld and Pfahl (2019) performed a similar composite analysis for the latent heating associated with blocks and found a more pronounced upper-level ridge pattern due to similar reasons as discussed at the end of section 7.3. Overall, the latent heating in the warm conveyor belts of extratropical cyclones is important for the formation of both at-

mospheric blocks and upper-tropospheric ridges associated with heat waves. Also Quinting and Reeder (2017) highlighted the role of cloud-diabatic processes and ascending air streams for upper-level anticyclones during heat waves in southeastern Australia. This is similar to the warm conveyor belts in our remote branches.

After discussing the synoptic conditions of the remote heating branch, we now focus on the conditions of the nearby heating branch. In this branch, the diabatic heating maximum is located below the western part of an upper-tropospheric anticyclone, which is much more pronounced compared to the remote heating branch (Figs. 7.9a,b). In contrast, the frequency of both cyclones and WCBs at the position of maximum diabatic heating is reduced (WCBs are not visible in Figs. 7.9a,b; they occur with frequencies of less than 3%). Hence, the driving mechanisms of the latent heating differs between the two branches. The circulation at 800 hPa is more anticyclonic and much weaker in the nearby compared to the remote heating branch. The most substantial difference between the two heating branches is the enhanced ML CAPE in the nearby heating branch (Figs. 7.9a,b), indicating the potential for convection. The absolute values of ML CAPE are, however, not extremely high, which may indicate that convection is efficiently depleting the ML CAPE. Additionally, according to ERA-Interim, most of the precipitation in the nearby heating branch is indeed convective (Fig. 7.9a; more clear for western Russia in Fig. 7.9b), whereas precipitation in the remote heating branch is predominantly stratiform (Fig. 7.8a). Cloud top temperatures derived from infrared satellite imagery are between -5 and -9 °C at the location of maximum diabatic heating (not shown). Hence, it is assumed that in the nearby branch latent heating is driven by mid-level convection or deep convection that reaches from lower into mid levels.

The anomalies underline the importance of the enhanced blocking frequencies and ML CAPE values for the nearby heating branch (Figs. 7.9c,d). Although the anomalies show also a small positive anomaly of cyclone frequencies (Figs. 7.9c,d), the absolute frequency (Figs. 7.9a,b) is lower compared to the remote heating branch (Fig. 7.8a). Comparing the two regions, western Russia shows slightly higher anomalies of blocking frequencies and ML CAPE at the location of maximum diabatic heating (Fig. 7.9d). The nearby heating branch has not yet been discussed in the literature on the formation of European blocking, but it appears to be relevant for the formation of upper-tropospheric anticyclones in association with heat waves in summer.

Trajectory-centred composites for the remote branch reaching anticyclones over western Russia, as well as for both heating branches arriving over the Iberian Peninsula, British Isles, Scandinavia and Greece/Italy can be found in the Appendix (Figs. A2.4-A2.8). Overall, the composites are qualitatively similar to the already discussed ones, especially for the remote branches (panels a and b in Figs. A2.4-A2.8), and only differ with respect to the magnitudes of ML CAPE in the nearby branch. ML CAPE val-

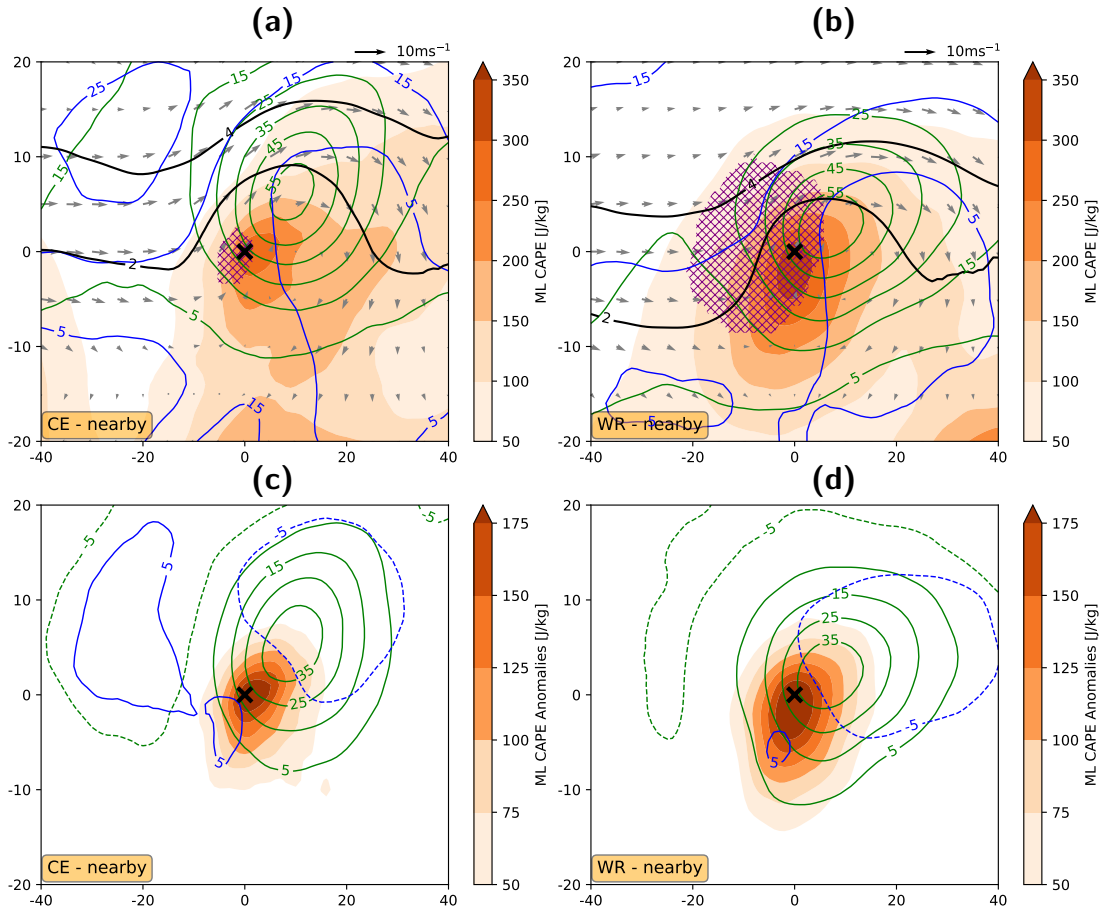

Figure 7.9: Same as Fig. 7.8, but for the nearby heating branch reaching Central Europe (a,c) and western Russia (b,d). Note that WCB frequencies are not shown because they are negligible in the nearby branch. The top row shows the full fields and the bottom row the anomalies. The purple hatching marks, in contrast to Fig. 7.8, the area where the convective precipitation exceeds the stratiform precipitation (only for areas with total precipitation $\geq 2\,\mathrm{mm\,d^{-1}}$). Figure taken from Zschenderlein et al. (2020). © The authors and Copernicus Publications, CC-BY.

ues for Greece/Italy are comparable to those for western Russia, albeit in a smaller area (Figs. A2.8c,d), but generally lower for trajectories of the nearby branch reaching anticyclones over Scandinavia (Figs. A2.7c,d) or the British Isles (Figs. A2.6c,d). In addition, the upper-level ridge of the nearby branch reaching Scandinavia (Fig. A2.7c) is more pronounced compared to Greece/Italy (Fig. A2.8c). A similar difference in the magnitude of the upper-level ridge is found for the remote branches (Figs. A2.7a and A2.8a).

7.5 Diabatic heating during the life cycle of heat waves

Here, the life cycle of the upper-tropospheric anticyclones associated with heat waves is investigated, i.e. the temporal sequence of the occurrence of the different heating branches. The contributions of the nearby and remote heating branches and their relative

importance with respect to the whole heating branch is quantified as a function of the duration of the heat waves. We concentrate on the results for Central Europe, because this region is equally affected by both branches. Due to the definition of the heat waves (cf. section 4.3), all events have a minimum duration of three days (Fig. 7.10). 73 events have a duration of at least three days, but only two of them last 13 days. We therefore start with the discussion of the results for the heat waves with a duration up to six days and then elucidate the findings for the longer-lived heat waves. For the latter category, the results are likely less robust due to the small number of events.

During the onset of a heat wave, the remote heating branch is of primary importance (Fig. 7.10). The formation of the upper-tropospheric anticyclone is therefore strongly affected by air masses that are diabatically heated in extratropical cyclones in the North Atlantic region. After the first two days of the heat waves, the nearby heating branch with air masses originating from northwestern Africa and heated diabatically due to convection below the western part of the ridge gains relevance (Fig. 7.10), thus supporting the maintenance of the upper-tropospheric anticyclone. The fraction of trajectories in the whole heating branch, i.e. remote and nearby heating branch together, with respect to all trajectories slightly increases during the maintenance of the upper-tropospheric anticyclone (black line in Fig. 7.10). Hence, the influence of latent heating increases during the life cycle of the events mainly due to an intensification of the nearby heating branch. At first sight, this result is contradictory to the findings of Pfahl et al. (2015) and Steinfeld and Pfahl (2019), who showed that the influence of latent heating reduces during the maintenance phase of atmospheric blocks. However, the heating relevant for atmospheric blocking mainly occurs in trajectories similar to our remote heating branch, and this branch loses relevance for the maintenance (up to day five) of upper-tropospheric anticyclones also here (Fig. 7.10).

Overall, the formation of upper-tropospheric anticyclones depends mainly on the latent heating within extratropical cyclones in the North Atlantic storm track, whereas the maintenance is related to air masses that are diabatically heated due to convection above western and central Europe. Although this pattern seems to be relevant for most of the heat waves, longer lasting heat waves show a different behaviour.

The maintenance of heat waves beyond six days duration is more influenced by the remote heating branch compared to the maintenance of shorter lasting heat waves (Fig. 7.10). Note that these longer lasting heat waves occur only rarely, therefore results are variable from case to case and less robust. However, it seems that the remote heating branch revives and has a comparable influence as during the onset of the heat wave. It is therefore hypothesised that long-lived upper-tropospheric anticyclones cannot be sustained by the nearby heating branch alone. Rather, cyclones over the North Atlantic and the associated latent heat release are relevant to maintain the negative PV anomalies in

the upper troposphere above the heat wave areas. In addition, the fraction of the heating branch related to all trajectories increases for longer-lasting heat waves up to nearly 50%.

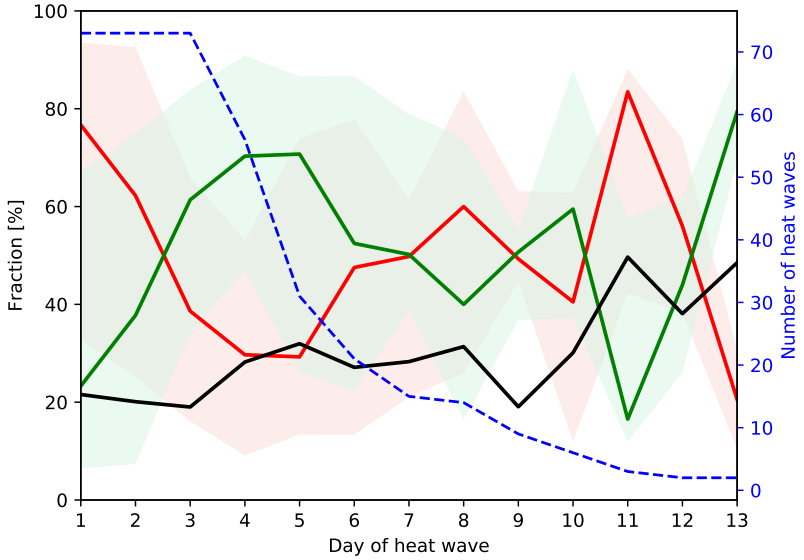

Figure 7.10: Latent heating during the life cycle of upper-tropospheric anticyclones connected to heat waves in Central Europe. The red (green) line shows the median contribution of the remote (nearby) heating branch to the whole heating branch, the shading represents the range between the 25th and 75th percentile. The median fraction of the heating branch relative to all trajectories is represented by the black line and the number of heat waves is indicated by the blue dashed line. Figure taken from Zschenderlein et al. (2020). © The authors and Copernicus Publications, CC-BY.

Chapter 8

Predictability of the 2018 heat wave in Central Europe

This chapter presents a trajectory-based analysis on the predictability of the Central European heat wave in 2018. Firstly, subsection 8.1.1 describes the identification of heat waves and is followed by the presentation of the trajectory-approach in subsection 8.1.2. Secondly, errors from 2-m temperature predictions with 3- and 7-day lead time are quantified for the heat wave days in section 8.2. Then, section 8.3 relates prediction errors to physical processes along trajectories and section 8.4 analyses whether forecast errors are limited to the planetary boundary layer.

8.1 Methods

8.1.1 Identification of heat waves

Heat waves are identified as periods, where 2-m temperatures at 1200 UTC exceed the local 90th percentile for at least three days in at least 10% of the Central European land area, which is defined as the area bounded by the purple lines in Figs. 8.4a,b. The 90th percentile is calculated based on Eq. 2.1 (cf. section 2.1), with the difference that the reference period is 1979–2017. Figure 8.1 depicts the fraction of the Central European land area exceeding the 90th percentile in May to September 2018. Several heat waves affect Central Europe, especially between mid July and mid August. For many days during this period, more than 50% of Central Europe exhibits 2-m temperatures exceeding the 90th percentile. The main focus of this study is on the most prolonged heat wave in 2018, which lasts from 24 July to 09 August 2018 (red shading in Fig. 8.1).

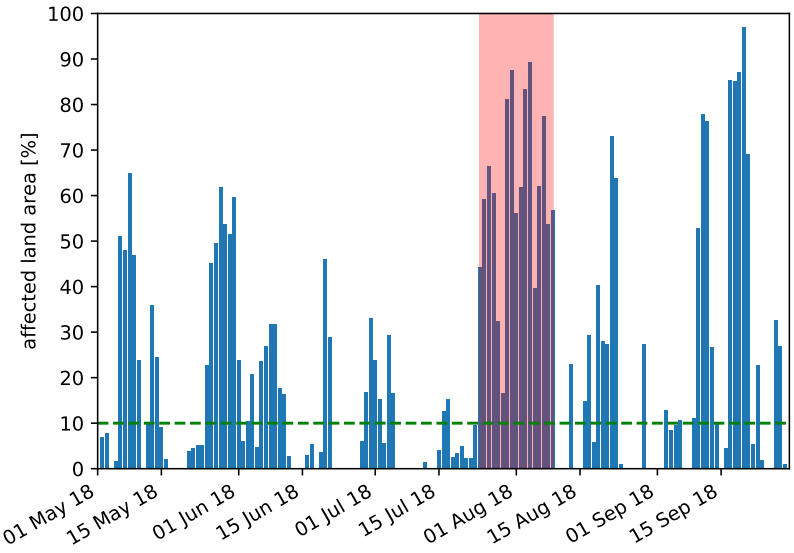

Figure 8.1: Fraction of Central European land area exceeding the local 90th percentile of 2-m temperature between 01 May and 30 September 2018 (blue bars). The green line marks the threshold (10%) for the heat wave identification and the red shading the heat wave from 24 July to 09 August 2018.

8.1.2 Causes of forecast errors

The quantification of the predictive skill is based on errors of 2-m temperature and 500-hPa geopotential height with 3- and 7-day lead time. For each heat wave day, the difference between predicted and observed values is determined and averaged over the heat wave area for each ensemble member. ERA-Interim is used as the verifying observation and the 51 members of the operational ECMWF forecasting system as predictions.

A two-step approach is applied that allows to quantify the processes leading to 3-day forecast errors in 2-m temperature in a Lagrangian framework. First, 3-day backward trajectories, driven by three-dimensional ERA-Interim wind fields on 60 vertical model levels are calculated. The trajectories are initialised at heat wave grid points on every day at 12 UTC and in the lower troposphere at 10, 30, 50, 70 and 90 hPa above ground level. Second, the endpoints of these 3-day backward trajectories (blue circles in Fig. 8.2) serve as starting points for 3-day forward trajectories (green lines Fig. 8.2) that are driven by three-dimensional wind fields on 63 vertical levels from the ECMWF ensemble forecasts. Both forward and backward trajectories are calculated with LAGRANTO (Sprenger and Wernli, 2015) and physical parameters traced along trajectories include temperature and potential temperature.

The relation between forecast error and trajectories is based on the comparison of the two sets of trajectories. In a perfect forecast, the pathway and physical parameters of the two trajectory sets would be nearly identical. But the parameters along trajectories are sensitive to small differences in the three-dimensional wind field and non-conservative

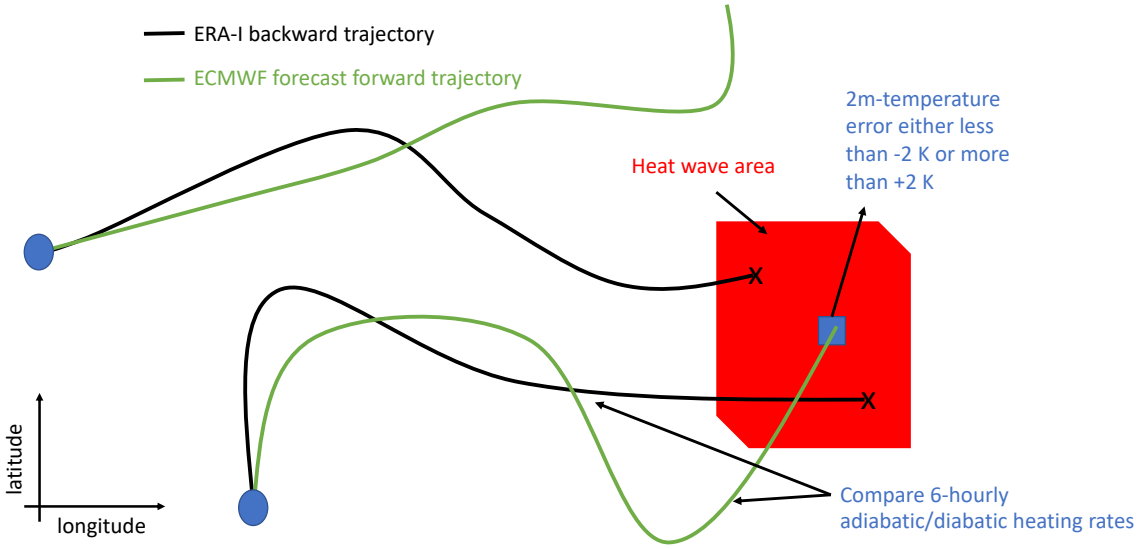

Figure 8.2: Schematic of backward (black, based on reanalysis) and forward trajectories (green, based on forecasts) that illustrates the method of studying the predictability of heat waves (two-dimensional heat wave area is marked in red). Black crosses indicate the starting point and blue circles the endpoint of 3-day backward trajectories. The latter points serve as starting points for 3-day forward trajectories. Forward trajectories missing the two-dimensional heat wave area are discarded from the analysis, as well as associated backward trajectories (e.g. green and black trajectory at the top), while the rest is separated according to the 2-m temperature error at the endpoint of the forward trajectories in the heat wave area (blue square). Along these trajectories, 6-hourly adiabatic and diabatic heating rates are compared.

processes such as diabatic heating. Therefore, predicted (i.e. forward) trajectories deviate from observed trajectories (i.e. backward trajectories) at some point (Fig. 8.2) and geographic location, altitude and physical properties of the trajectories can be compared. Only forward trajectories reaching the heat wave area are considered and trajectories missing the heat wave area are discarded from the analysis, as well as associated backward trajectories. In the example of Fig. 8.2, only the forward trajectory at the bottom reaches the two-dimensional heat wave area (red area in Fig. 8.2). For trajectories reaching the heat wave area, 6-hourly diabatic and adiabatic heating rates along trajectories from forecast and reanalysis are compared, based on the Lagrangian temperature tendency equation (Eq. 2.12 in subsection 2.2.4). More specifically, temperature changes (ΔT) and the terms $\frac{d\theta}{dt}\left(\frac{p}{p_0}\right)^{\kappa}$ (diabatic processes, Δ_{diab}) and $\frac{T\kappa\omega}{p}$ (adiabatic processes, Δ_{adiab}) are calculated along both trajectory sets for every 6 hours. In order to relate forecast errors to physical processes along trajectories, 6-hourly changes of the three properties from predicted trajectories are subtracted from analysed trajectories:

$$\Delta \mathrm{T}_{\mathrm{diff}} = \Delta \mathrm{T}_{\mathrm{f}} - \Delta \mathrm{T}_{\mathrm{a}} \tag{8.1}$$

$$\Delta_{\mathrm{diab,diff}} = \Delta_{\mathrm{diab,f}} - \Delta_{\mathrm{diab,a}} \tag{8.2}$$

$$\Delta_{\mathrm{adiab,diff}} = \Delta_{\mathrm{adiab,f}} - \Delta_{\mathrm{adiab,a}} \tag{8.3}$$

The indices *f* and *a* in Eqs. 8.1-8.3 stand for forecast and reanalysis, respectively.

In order to understand, why predictions over- or underestimate the observed 2-m temperature, trajectories are separated as follows: firstly, endpoints of forward trajectories are re-gridded by means of the nearest neighbour method on a 1°x1° regular latitude-longitude grid to match the horizontal grid spacing of reanalysis and forecasts. Secondly, 2-m temperature errors at the re-gridded endpoints of these trajectories are calculated and divided into two groups. One group underestimates the observed 2-m temperature (error ≤ -2 K) and the other group overestimates the observed 2-m temperature (error $\geq$ 2 K). Note that other thresholds of the error have been tested and results are qualitatively similar.

8.2 Forecast errors

Figure 8.3 illustrates the 2-m temperature error of ensemble predictions with 3- and 7-day lead time. 7-day ensemble predictions typically underestimate the averaged 2-m temperature in the heat wave area (Fig. 8.3a). However, predictive skill varies within the heat wave. The onset is not well predicted, but predictive skill slightly increases towards 28 July. Afterwards, predictive skill again deteriorates and is worst for 7 August with underestimations mostly between 3 and 7 K. The last two days of the heat wave shows slightly higher predictive skill, at least for the ensemble median. However, predictions are very uncertain due to the high spread of the members. In comparison, 3-day prediction errors are considerably reduced, but still predicting too low temperatures (Fig. 8.3b). The underestimation of 2-m temperature was also discovered in the case study of the 2016 heat wave in Chapter 5 and in Magnusson et al. (2018) for 2-day forecasts between 07 May and 12 August 2018 in Europe.

The working hypothesis for this study is that errors on the 7-day time scale are related to errors in upper-tropospheric dynamics, e.g. phase speed and amplitude of Rossby wave packets, while errors on the 3-day time scale are related to vertical motion and diabatic processes in the air masses closer to the location of the heat wave. As an illustration for this, Fig. 8.4a shows the geopotential height error of the worst 7-day forecast for 07 August 2018. For this day, predicted temperatures are about 9 K too cold, averaged over the

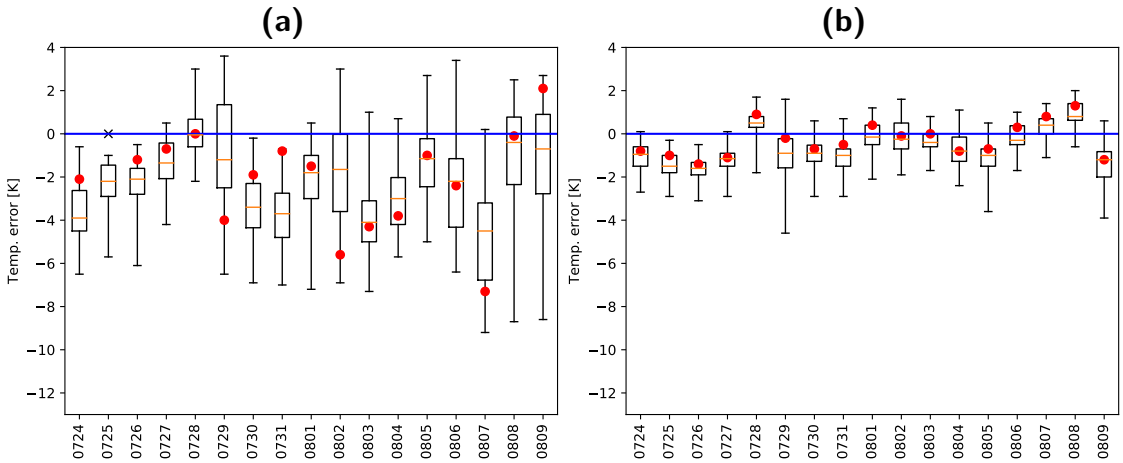

Figure 8.3: 2-m temperature errors of ECMWF ensemble 7-day (a) and 3-day (b) forecasts for heat wave days between 24 July and 09 August 2018. The dates on the x-axis show the valid day of the forecast (the first two digits denote the month, the latter two the day, always 12 UTC). In the boxplots, the orange line denotes the median, boxes the interquartile range and whiskers the minimum and maximum error. The red circles represent the temperature error of the control forecast. Crosses on the blue line indicate that not all ensemble members are available for this day and lead time[1].

heat wave area (Fig. 8.3a). The underestimation is associated with errors in the 500-hPa geopotential height. Upstream of Central Europe, the upper-level trough is missing and instead, an upper-level ridge is predicted (Fig. 8.4a). Over and downstream of Central Europe, a trough is predicted instead of a ridge (Fig. 8.4a). Hence, upper-tropospheric dynamics play a dominant role, because upper-level ridges provide conditions conducive to heat waves (cf. Chapter 6). The northwesterly flow in Fig. 8.4a transports presumably colder air masses from the North Sea to Central Europe and the ensemble member therefore underestimates the observed 2-m temperature. In contrast, 3-day geopotential height predictions for 26 July are comparably small (Fig. 8.4b, shown for the ensemble member with the largest 2-m temperature error), although averaged 2-m temperatures errors are about -3 K for the ensemble member with the largest 2-m temperature error (Fig. 8.3b). As a surrogate for the role of upper-tropospheric dynamics, errors of 500-hPa geopotential height, averaged over the heat wave area, are determined for both 3- and 7-day lead time. Both the amplitude error, as well as the uncertainty of the ensemble, is considerably higher for 7-day forecasts compared to 3-day forecasts (Figs. 8.4c,d). It seems that 7-day forecasts consistently underestimate the 500-hPa geopotential height and therefore the amplitude of the upper-level ridge, especially during the onset (24 July) and during the maintenance (e.g. 30 July to 05 August). These errors are connected to 2-m temperature errors. During the onset, both 500-hPa geopotential height and 2-m

[1]The reason is that the connection between the LSDF server (at KIT) and ECMWF got lost due to sporadic down times of the LSDF server.

temperature are underestimated. In the next days of the heat wave, until 29 July, errors in both 500-hPa geopotential height and 2-m temperature decrease, while afterwards, forecasts of both parameters deteriorate again. The potential causes of 3-day forecast errors in 2-m temperature is analysed with trajectories in the next section.

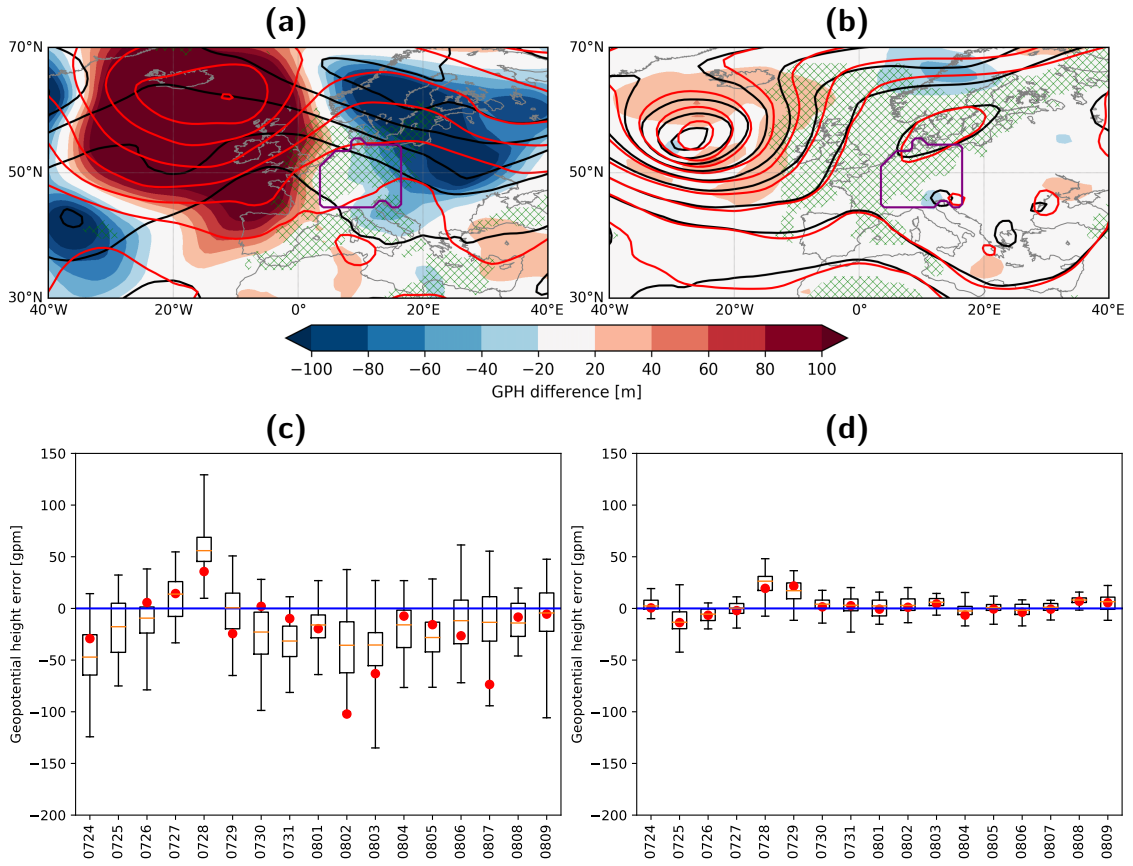

Figure 8.4: 500-hPa geopotential height errors. The panels at the top show a 7-day forecast for 07 August 2018 (a) and a 3-day forecast for 26 July 2018 (b) for the ensemble member with the largest 2-m temperature error. Colour shading denotes the difference between forecast and reanalysis. Black (red) contours represent 500-hPa geopotential height of the forecast (reanalysis). The green hatching represents the area exceeding the local 90th percentile and the purple polygon Central Europe. Panels at the bottom depict the 500-hPa geopotential height errors for 7-day (c) and 3-day forecasts (d). The dates on the x-axis show the valid day of the forecast (the first two digits denote the month, the latter two the day, always 12 UTC). In the boxplots, orange lines denotes the median, the boxes the interquartile range and the whiskers the minimum and maximum error. The red circles represent the control forecast.

8.3 Forecast errors related to trajectories

The trajectory-approach is at first presented for one day and a single member (the member with the largest 2-m temperature error), and later for the whole heat wave period

between 24 July and 09 August. All ensemble members in the 3-day forecasts for 26 July underestimate the 2-m temperatures (Fig. 8.3b). According to ERA-Interim, most trajectories reach the heat wave area on an anticyclonic pathway and originate mostly from the north, i.e. the British Isles, Denmark or the Baltic States (Fig. 8.5a). Trajectories originating from the British Isles experience the strongest subsidence, while others have their origin in the lower troposphere. Using the endpoints of 3-day backward trajectories as starting points for forward trajectories (cf. Fig. 8.2), an overall similar pattern emerges, but around 50% of the trajectories miss the heat wave area (Fig. 8.5b). A comparison of the pressure along observed and predicted trajectories leads to the conclusion that most forward trajectories are too high and do not descend deep enough (Fig. 8.5c). Too weak subsidence leads to a reduced temperature increase and therefore reduced surface temperatures. However, not all trajectories reach the heat wave area (Fig. 8.5b) and, therefore, the comparison between the two trajectory sets not always reasonable, because predicted and observed trajectories can be far apart (Fig. 8.5d).

To avoid this drawback, only trajectories reaching the heat wave area are considered for a systematic analysis. In the following, 6-hourly temperature changes, as well as diabatic and adiabatic heating rates along the two trajectory sets are compared for predictions overestimating (error $\geq$2 K) and underestimating 2-m temperatures (error ≤ -2 K), respectively. Figure 8.6 illustrates the difference between forecast and analysis of the 6-hourly temperature changes ($\Delta \mathrm{T}_{\mathrm{diff}}$, Eq. 8.1) due to diabatic ($\Delta_{\mathrm{diab,diff}}$, Eq. 8.2) and adiabatic processes ($\Delta_{\mathrm{adiab,diff}}$, Eq. 8.3). A positive (negative) difference implies a higher (lower) temperature change or adiabatic/diabatic heating rate of the forecast compared to the observation. 23,598 trajectories are associated with too low 2-m temperatures, whereas only 11,276 are connected to predictions overestimating 2-m temperatures (Fig. 8.6).

Figure 8.6a shows the difference of the heating rates between forecast and analysis for predictions underestimating 2-m temperatures. Subsidence is underestimated and therefore, the temperature increase is less than observed (orange line in Fig. 8.6a), especially from hour 36 after initialisation. This can also be inferred from the increasing pressure difference between predicted and observed trajectories (green dashed lines in Fig. 8.6a). However, incorrect representation of diabatic processes dominates the error of the temperature prediction (purple line in Fig. 8.6a). During the day and especially between 12 and 18 UTC (red shading in Fig. 8.6a), diabatic heating is underestimated. As shown in Chapter 6, surface sensible heat fluxes are an important diabatic process in the lower troposphere, therefore, it is argued that these fluxes are underestimated in the forecast, leading to reduced temperature increases compared to the observation.

Figure 8.6b shows the heating rates for predictions with 2-m temperature errors above 2 K. Similar to predictions underestimating 2-m temperature, diabatic heating between

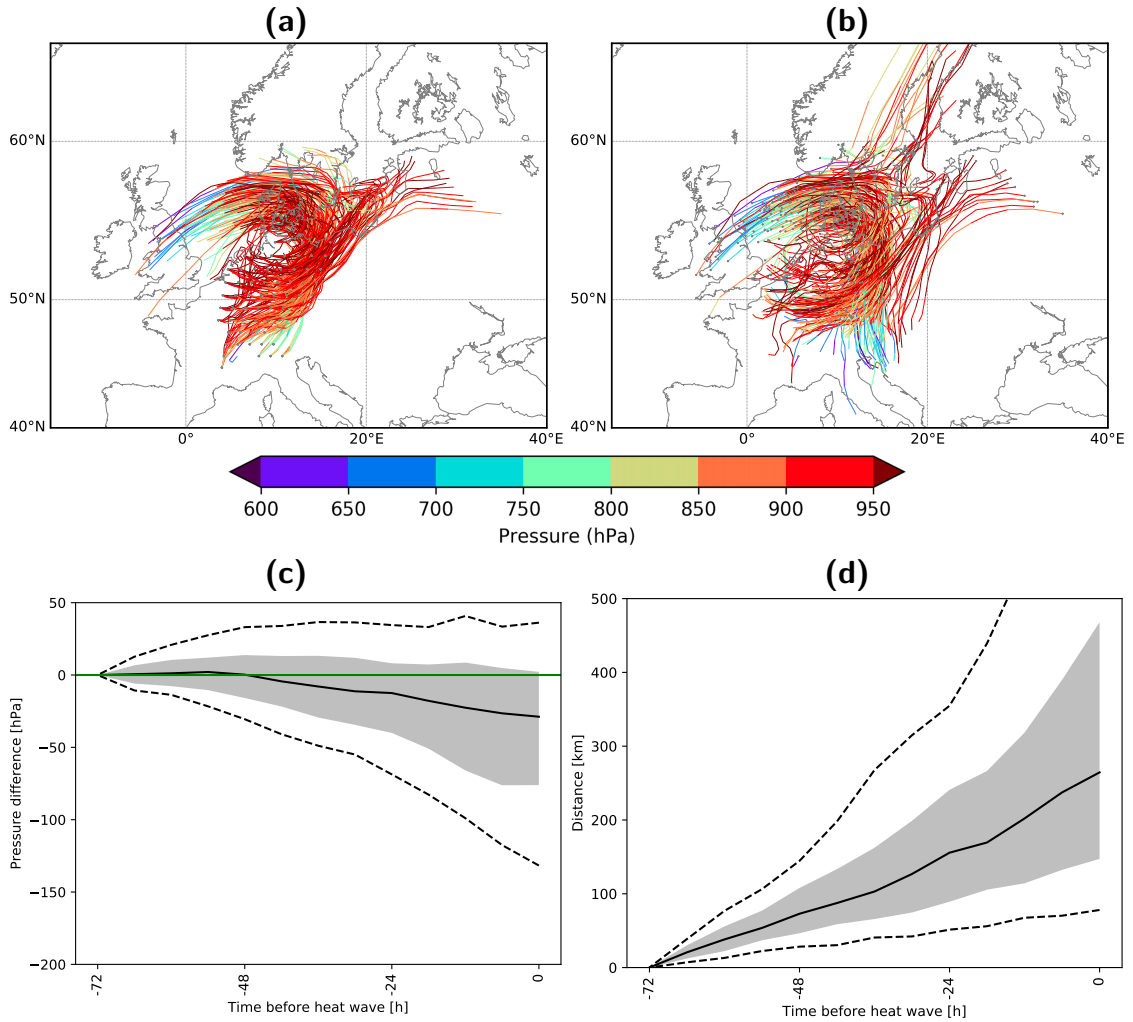

Figure 8.5: Example of the trajectory-approach for the ensemble member that underestimates the 2-m temperature the most on 26 July 2018. (a) 3-day backward trajectories initialised in the heat wave area (grey points), (b) 3-day foreward trajectories initialised at the endpoints of the backward trajectories (grey points). The coloured lines represent the height of the trajectory (in hPa). The lower panels illustrate the pressure difference (c), where a negative pressure difference indicates that the predicted trajectory is too high, and distance (d) between predicted and analysed trajectories. In the lower panels, the solid black line denotes the median, the grey shading the interquartile range and the dashed lines the 10^{th} and 90^{th} percentile of the parameters, respectively.

12 and 18 UTC is underestimated. But in contrast, diabatic heating during 06 and 12 UTC is considerably overestimated. Therefore, the influence of surface sensible heat fluxes and radiative effects in the morning and around noon is likely too high, leading to a general overestimation of 2-m temperature. It is hypothesised that in reality clouds develop and reduce the incoming solar radiation, which in turn lowers the surface sensible heat fluxes and the near-surface temperatures. Therefore, forecasts seem to predict clear-sky conditions instead of cloudy conditions. In addition, diabatic processes during night

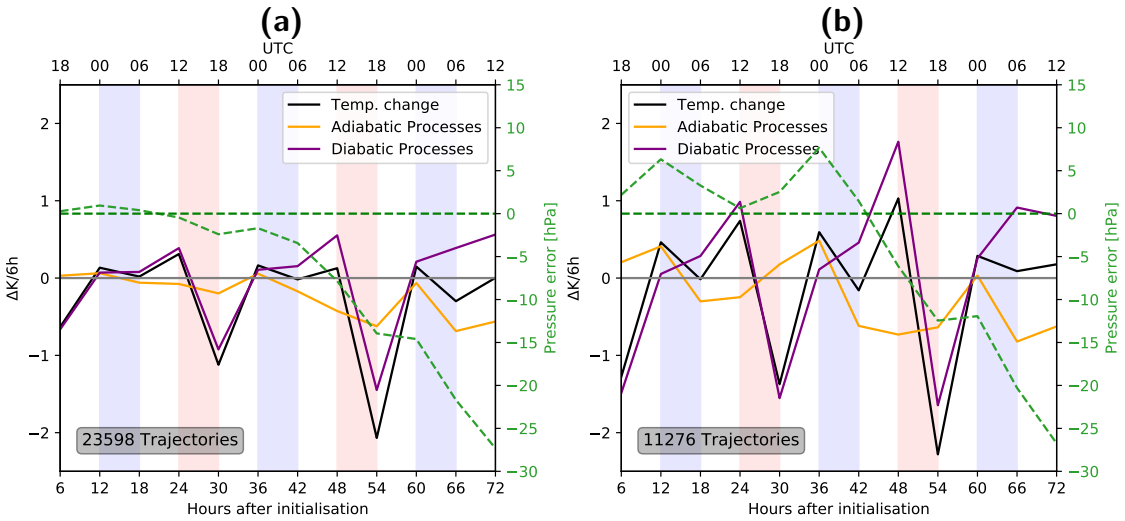

Figure 8.6: Difference between forecast and reanalysis of 6-hourly temperature changes ΔT_{diff} (black line, Eq. 8.1) and associated heating rates due to adiabatic processes $\Delta_{\mathrm{adiab,diff}}$ (orange line, Eq. 8.3) and diabatic processes $\Delta_{\mathrm{diab,diff}}$ (purple line, Eq. 8.2). The grey line is the corresponding zero line, i.e. everything below (above) this line implies that temperature change and corresponding adiabatic and diabatic processes are underestimated (overestimated). ΔK/6h is plotted at the end of the 6-h period. Time goes from 6 to 72 h after initialisation of the forward trajectory and time (in UTC) is indicated at the top. Blue/red vertical shadings indicate 6-hour time windows, in which diabatic cooling (blue, between 00 and 06 UTC) and diabatic heating (red, between 12 and 18 UTC) is usually strongest. The green dashed line shows the difference between the pressure of predicted and analysed trajectories and the horizontal green dashed line shows the corresponding zero line. Everything above (below) this line means that predicted trajectories have a higher (lower) pressure than analysed trajectories and are therefore too low (high).

are slightly overestimated. Note that an overestimation of diabatic processes during night implies that diabatic cooling is too weak. As an example, diabatic cooling is $-1\,\mathrm{K\,6h^{-1}}$ in the forecast, but $-2\,\mathrm{K\,6h^{-1}}$ in the verifying analysis. In this case, $\Delta_{\mathrm{diab,diff}}$ is $+1\,\mathrm{K\,6h^{-1}}$ (cf. Eq. 8.2). The insufficient nighttime diabatic cooling results in an overestimated night temperature. This overestimation occurs in particular shortly before the arrival of the trajectory in the heat wave area (blue shading 60 to 66 h after initialisation, Fig. 8.6b).

8.4 Vertical structure of forecast errors

The trajectory analysis reveals that temperature errors are mostly due to diabatic processes close to the surface. This suggests that the temperature errors are confined to the planetary boundary layer (PBL) and are not tropospheric deep. To test this hypothesis, Fig. 8.7 illustrates the temperature errors at 950, 900, 850, 800 and 700 hPa for all heat wave grid points, where predictions either underestimate (error $\leq -2\,\mathrm{K}$, Fig. 8.7a) or

overestimate 2-m temperatures (error $\geq$2 K, Fig. 8.7b).

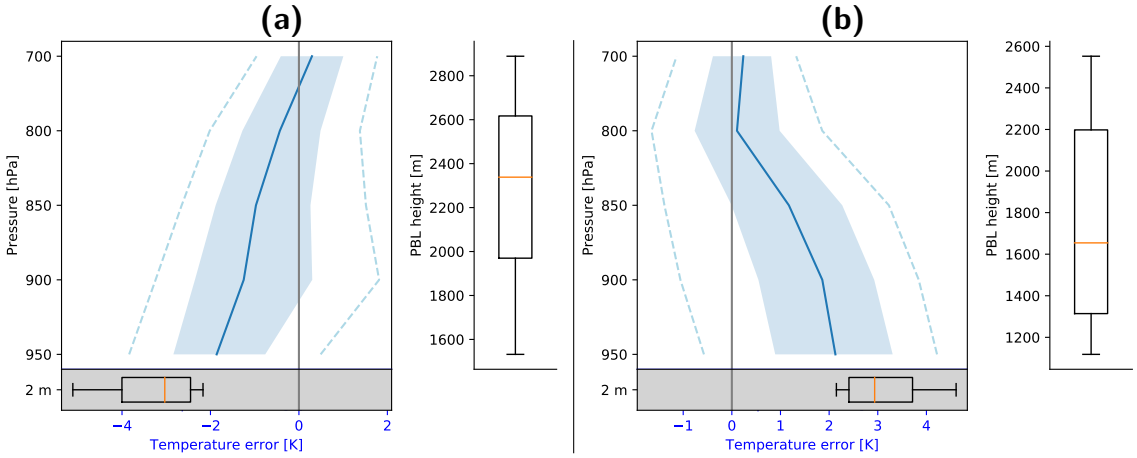

Figure 8.7: Temperature errors at pressure levels (blue colours) and at 2-m height (boxplot with grey background) for 3-day forecasts with 2-m temperature errors ≤ -2 K (a) and $\geq$2 K (b). Boxplots on the respective right side illustrate the planetary boundary layer (PBL) height. The latter is derived from ERA-Interim 12 h forecast fields. In the boxplots, orange lines represent the median, boxes the inter-quartile range and whiskers the 10$^{\text{th}}$ and 90$^{\text{th}}$ percentile, respectively.

In forecasts underestimating 2-m temperature, the lower troposphere up to about 800 hPa is also colder than observed, but above, temperatures are well predicted or even too high (Fig. 8.7a). The PBL height, derived from ERA-Interim 12 h forecasts, is predominantly located at 2300 m height, which corresponds to roughly 750 hPa. Hence, temperature errors are limited to the planetary boundary layer. In the other case, when predictions overestimate temperature, temperatures up to roughly 800 hPa are too high, while temperatures above are well predicted (Fig. 8.7b). And often, PBL height is located at 1700 m. In both cases, i.e. over- and underestimated 2-m temperatures, forecast errors are limited to the planetary boundary layer. This is an indication that entrainment at the boundary layer top is a source of uncertainty in the forecasts. Another possible error can be the misrepresented vertical mixing in the boundary layer or erroneous surface sensible heat fluxes.

Chapter 9

Conclusions

Heat waves are meteorological extreme events with health and socio-economic impacts. In a changing climate, these events are expected to increase. However, basic understanding of the processes leading to heat waves is still incomplete and the thesis aimed at reducing this gap. The main research aim of this thesis has been to improve the understanding of the processes leading to heat waves. As such, two main research aims have been to investigate processes leading to high near-surface temperatures during the heat wave and to analyse processes leading to upper-tropospheric anticyclones associated with heat waves. Furthermore, the predictability and predictive skill of heat waves have been analysed for two case studies. Chapter 2 reviewed the current scientific knowledge on these three aspects, and deduced from that, research questions were addressed in Chapter 3.

Chapter 5 analysed the planetary- and synoptic-scale developments that led to the 2016 European late summer/early autumn heat wave, and following research questions were addressed:

A1 How intense is this heat wave? Central, western and southwestern Europe are the most affected regions, with record-breaking maximum temperatures in some places. The highest September temperatures since their respective records began are reported at both Seville (44.8°C; records started in 1951) and Trier (34.2°C; records started in 1941).

A2 How can high temperatures during the heat wave be related to upper-tropospheric Rossby wave packets? The three peaks are all accompanied by pronounced 500-hPa ridges. The first two peaks show larger areas with the highest values of geopotential height for that time of the year since at least 1979. The ridges are embedded in eastward-propagating, high-amplitude Rossby wave packets arriving over western Europe. The packets

have their origins over western North America.

A3 Which physical processes lead to high temperatures during the event? Though it has not been discussed here, it is worth noting that local temperature advection does not play a noticeable role in local temperature changes at Bordeaux, Seville or Trier. On the contrary, the adiabatic compression term due to subsidence exhibit exceptionally high values for the Bordeaux and Seville cases. Changes in the temperatures of subsiding parcels arriving at the lower troposphere at these locations are substantial – of the order of 20–30 K – in the 2–3 days prior to the peak of the heat waves. Diabatic processes (such as surface sensible heat fluxes due to enhanced insolation) and dry convection in the boundary layer appear to be the major explanation for the occurrence of the Trier heat wave event, where hardly any subsidence occurs.

C1 How accurate are the predictions for this event? Predictions of the hottest day, with respect to station observations, at a few days' lead time, are best for Bordeaux, followed by Seville and Trier. However, with respect to the model climatology, the ensemble prediction system shows the highest probabilities for extreme temperatures for Trier first, followed by Seville and Bordeaux.

The results presented in this study have potential ramifications for the investigation of the predictability of heat waves. While dry soils are a prerequisite for heat waves, an understanding of Rossby wave dynamics may allow for the development of early alerts for imminent heat wave events (cf. Magnusson et al., 2015). For the three peaks discussed in this study, the ECMWF ensemble prediction system indicated an enhanced likelihood of heat waves up to 5 days in advance, related to the discussed origin of the Rossby wave packets thousands of kilometres upstream. However, the final magnitude of the heat wave seems to be related to the details of the (thermo-)dynamics associated with the ridge embedded in the Rossby wave packet.

Chapter 6 presented a comprehensive analysis of processes determining heat waves across European regions representing different climates for the period 1979–2016. Heat waves were defined using the percentile-based HWMId (Russo et al., 2015). Different statistical properties of heat waves (frequencies and duration), their associated synoptic patterns, and physical processes along trajectories that led to high near-surface temperatures were investigated. The processes quantified along the trajectories were adiabatic warming by subsidence and diabatic processes. This quantification was complemented by an Eulerian calculation of horizontal temperature advection. Following research ques-

tions were addressed in this study:

A4 How often is Europe affected by a heat wave and how long do these events last? Heat waves persist four to five days and occur usually one or two times per year.

A5 What synoptic patterns are associated with heat waves? Upper-level ridges accompany high surface temperatures, corroborating the findings of Pfahl and Wernli (2012) and Sousa et al. (2018). The amplitude of the ridges are generally lower in Greece/Italy and the Iberian Peninsula compared to Scandinavia. Upstream of the ridges, the amplitudes of the troughs over the North Atlantic Ocean are highly variable.

A6 What are typical source regions, pathways and physical processes along trajectories reaching heat wave areas? Horizontal transport of (already) warm air, i.e. temperature advection, appears not to be an important factor in establishing heat waves. In contrast, subsidence, entrainment of warm air into the lower troposphere and diabatic heating due to surface sensible heat fluxes are crucial in determining high temperatures near the surface. This corroborates the findings of Bieli et al. (2015). In all regions, three trajectory clusters are associated with high near-surface temperatures. All these clusters experience an increase in the temperature of air parcels, however with differences in diabatic heating and vertical motions (see Table 6.1 for the definition of the clusters). The increase of temperatures of the trajectories is accelerated in the last three days prior to the heat waves. Most of the trajectories are already near or in the target area three days prior to the heat waves. The trajectory cluster A is overall diabatically cooled due to radiative cooling in the free atmosphere. During the last three days, air parcels in this cluster are strongly descending in the vicinity of the heat wave area, leading to a heating rate between 3 and 5 K per day. Cluster B_{sd} experience overall diabatic heating and descends strongly. In the last three days, the warming of the air parcels are due to both subsidence (1.5 K per day) and surface fluxes (1.5 K per day). The third cluster, B_{wd}, is located near the surface and diabatically heated at a rate of about 2 K per day with a maximum for the Iberian Peninsula of about 4 K per day three days before a heat wave.

About 50 % of all trajectories fall into cluster B_{sd} and 25 % fall into clusters A and B_{wd} respectively, with some inter-regional differences. Although subsidence is a very important driving factor, surface sensible heat fluxes are

also important for western Russia, whereas the British Isles are less influenced by surface fluxes. With respect to the role of the diabatic heating near the surface in addition to the local influence of surface sensible heat fluxes, e.g. in western Russia, also remote surface fluxes in regions to the east of the target region play an important role. Similar results are found for Greece/ Italy, where the influence of surface fluxes to the northeast is also important. Quinting and Reeder (2017) found a similar result for heat waves in southeastern Australia. They argued that local effects of soil moisture are of minor importance, whereas the transport above remote dry soils has a larger impact. The inflow of heat and moisture from remote regions to the heat wave area was named ”event self-propagation” by Miralles et al. (2019), which seems to be important for western Russia and to a lesser extent for Greece/ Italy. However, as noted by Miralles et al. (2019), these remote interactions are still not well understood and provide avenues for further research.

A8 Are heat waves steadily influenced by new air masses or are the air parcels being stalled in the lower troposphere over a longer time period? Throughout the life cycle of a heat wave, new air masses are steadily imported into the heat wave regions, either due to subsidence from higher levels or air coming from adjacent areas heated by surface fluxes. The results therefore suggest that the discussed Lagrangian processes are crucial in determining the high near-surface temperatures, whereas the stagnation of air masses longer than a few days is of minor importance for European heat waves. Stagnant air masses are more important for air parcels in cluster B_{wd} which are located in the target area near the surface and are diabatically heated with nearly no vertical motion.

The analysis reveals that pure horizontal temperature advection of already warm air is not important for creating high near-surface temperatures in the considered European regions. A similar result was found by Quinting and Reeder (2017) for heat waves in Australia. The results here are likely influenced by the heat wave definition, because heat episodes below three days duration are excluded. Shorter heat episodes can be a result of horizontal temperature advection ahead of an upper-level trough near an extratropical cyclone. In such a situation, warm air advection may be able to elevate the temperatures near the surface for one day, however the passage of the cyclone’s cold front typically leads to a temperature decrease shortly after. Additionally, the impact of such short heat periods is comparably small.

Chapter 7 analysed the contribution of latent heating to the formation and mainte-

nance of upper-tropospheric anticyclones associated with heat waves in different parts of Europe. Based on heat waves identified in Chapter 6, backward trajectories are calculated from the anticyclones and separated according to their potential temperature changes. The heating branch was further subdivided according to the location of the air parcels three days prior to the arrival in the upper-tropospheric anticyclone into a nearby and remote heating branch. Air parcels located west (east) of 30°W three days prior to the arrival belong to the remote (nearby) heating branch. Following research questions were addresses in this study:

B1 What are typical source regions of low-PV air masses that constitute the upper-tropospheric anticyclones associated with European summer heat waves? For Central European heat wave anticyclones, mainly two geographic source regions exist. Three days prior to reaching the upper-tropospheric anticyclones, air parcels in the cooling branch are located in the upper troposphere southwest of the target region, mainly distributed between Central Europe and the central North Atlantic, peaking over the northwest coast of Africa (Fig. 9.1, label 1). Air parcels assigned to the nearby heating branch are located mainly between Central Europe and the northwest coast of Africa in the mid- to lower troposphere (Fig. 9.1, label 3), while air parcels in the remote heating branch culminate between eastern North America and the western North Atlantic (Fig. 9.1, label 2) at similar altitudes.

B2 Are there inter-regional differences in the contribution of diabatic heating to the formation of these anticyclones? Around 25-45% (35-50%) of the air parcels are diabatically heated during the last three (seven) days prior to the arrival in upper-tropospheric anticyclones. The influence of diabatic heating increases towards northern Europe and western Russia and decreases towards southern Europe. While most regions in Europe are - with varying magnitude - influenced by both the nearby and remote heating branch, western Russia is only influenced by one diabatic heating branch. The contribution of diabatic heating increases substantially on the seven-day timescale except for western Russia.

B3 Where and in which synoptic environment does the diabatic heating occur in airflows entering the anticyclones? For most regions in Europe, the diabatic heating occurs in two geographically separated moist ascending air streams. But the air streams differ not only in location, also the processes responsible for the diabatic heating are different. The remote heating branch is influenced by an enhanced activity of extratropical cyclones and associated

warm conveyor belts over the North Atlantic. Diabatic heating in this branch is accompanied by stratiform precipitation, in contrast to the nearby heating branch, where convective-scale precipitation dominates. The moist ascent in the latter branch occurs closer to the target anticyclone in an environment of enhanced ML CAPE and is also aided by orographic lifting.

B4 Are there differences in the relevance of diabatic heating during the formation and maintenance of the anticyclones? The activity in the North Atlantic and the associated latent heat release in cyclones and warm conveyor belts are of primary importance for the onset of the upper-tropospheric anticyclones connected to the heat waves. Their maintenance is affected by the more local diabatic heating in the nearby heating branch. For longer lasting heat waves, the remote heating branch regenerates and becomes more relevant compared to days 3-5, implying that the ridge connected to the longer lasting heat wave cannot be sustained without the transport of low-PV air to the upper troposphere within extratropical cyclones.

One shortcoming of the approach in Chapter 7 is that the trajectory calculations are not able to resolve small-scale convective processes. Hence, we possibly underestimate the effect of convection especially in the nearby heating branch and therefore the associated diabatic heating. Recently, Oertel et al. (2020) showed that embedded convection in warm conveyor belts can influence the synoptic-scale circulation and increase the isentropic PV gradient at upper-levels in addition to the slantwise WCB ascent. However, it is assumed that for the climatological analysis presented in Chapter 7, the source regions will not substantially change, because also the convective ascending parcels are located in the vicinity of the slantwise ascending WCB (Oertel et al., 2020) and we argue that convective parameterisation is tuned to capture the climatological bulk effects of deep convection on rainfall and latent heat release. For the nearby branch, especially in the Greece/Italy case, the pathway of individual trajectories affected by deep convection over the Atlas Mountains and the Alps might be more uncertain due to the proximity of convection to the heat wave region. Weisheimer et al. (2011) noted that a revised formulation of the convective parameterisations in the ECMWF model improved the predictability of the 2003 European heat wave. Interestingly, air parcels arriving over Greece/Italy can originate from the upper-level easterlies over West Africa. Pante and Knippertz (2019) show that explicit convection over West Africa improves forecast of upper-level fields over Europe at 5-8 days lead time. Thus, it would be interesting to calculate online, convection-permitting trajectories in high-resolution model simulations (e.g. Miltenberger et al., 2013) to study the impact of convection over the North African

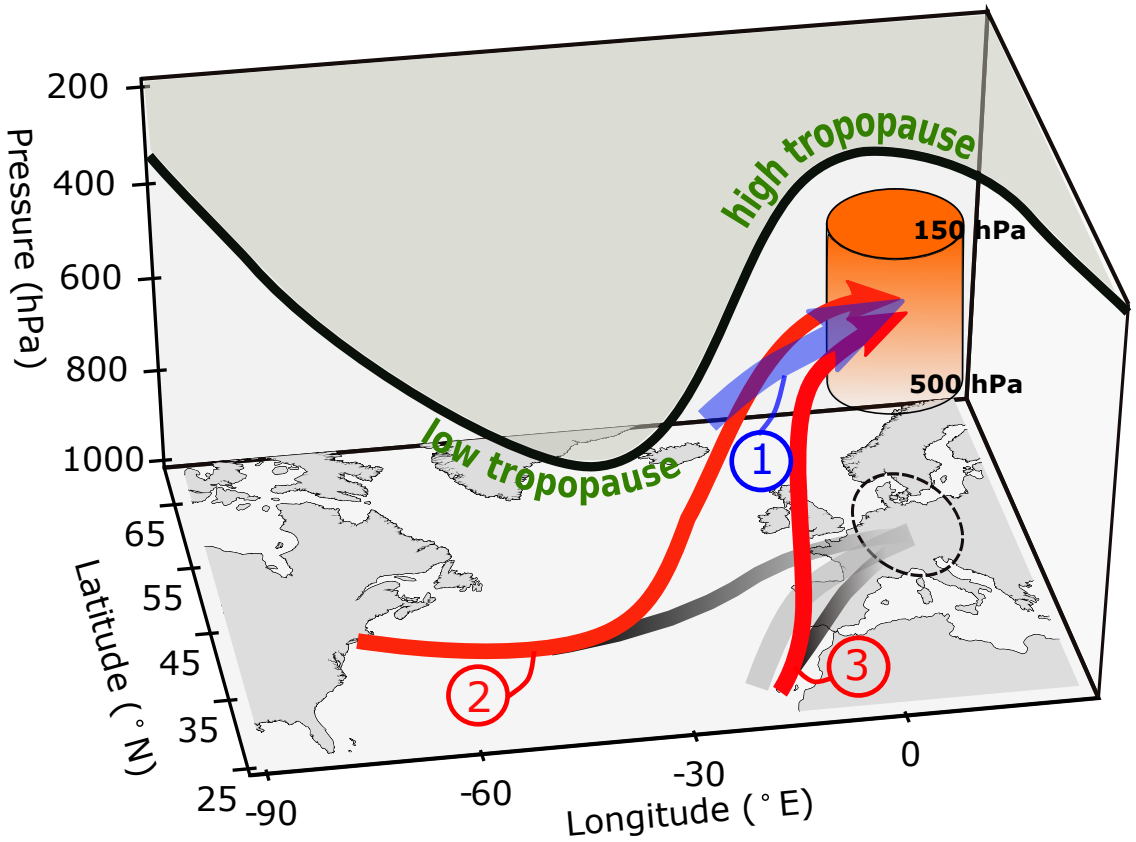

Figure 9.1: Schematic illustrating the pathway of the three air streams contributing to the upper-tropospheric anticyclone (red cylinder) above the heat wave in Central Europe (black dashed circle) during the last three days prior to arrival. Air stream 1 denotes the cooling branch and air streams 2 and 3 the remote and nearby heating branches, respectively. Grey-marked lines at the surface illustrate the projections of the arrows (lighter greys indicate a higher altitude of the associated air stream). The bold black line represents the dynamical tropopause. The arrow of air stream 1 is wider because this branch is less spatially coherent compared to air streams 2 and 3. Figure taken from Zschenderlein et al. (2020). © The authors and Copernicus Publications, CC-BY.

subtropics and over southern Europe on the formation of European heat waves.

Chapter 8 analysed the predictability of the 2018 heat wave with a new two-step trajectory-approach. Firstly, 3-day backward trajectories from the heat wave area are calculated. Secondly, endpoints of theses trajectories serve as initialisation points of forward trajectories with three-dimensional wind fields of operational ECMWF ensemble forecasts. This approach is unique and to the best of our knowledge has never been done before in connection with temperature forecasts, because ECMWF ensemble forecasts are normally not archived at such a high vertical resolution. Main research questions addressed in this study include:

C2 How accurately does the ensemble predict the 2 m temperature during heat waves? Predictions with lead times of seven and three days predominantly underestimate the observed temperature in the heat wave area. In general, predictions with seven days lead time show a higher underestimation of the observed temperature, as well as a higher uncertainty, which is mostly related to upper-tropospheric dynamics, as shown by larger errors of the 500-hPa geopotential height field. On the 3-day time scale, geopotential height errors are reduced, but temperatures are still mostly underestimated.

C3 How can the performance of predictions be related to air mass histories? Forecasts with three days lead time often underestimate the diabatic processes. As such, the diabatic heating between 12 and 18 UTC is largely underestimated, which is presumably due to a misrepresentation of surface sensible heat fluxes. This in turn often leads to an underestimation of observed 2-m temperatures. Temperature errors in the heat wave area are restricted to the planetary boundary layer. It is therefore assumed that entrainment at the top of boundary layer, vertical mixing, and erroneous surface fluxes contribute to the error.

Chapter 10

Outlook

Given the importance of heat waves due to their manifold impacts (WMO and WHO, 2015), it is crucial that the processes described in Chapters 5–8 are correctly modelled in state-of-the-art weather forecasting and climate models. For example, the Lagrangian trajectory analysis presented in Chapter 6 may be applied to an ensemble forecasting system to assess why some ensemble members perform better or worse. A first step in this direction is the method employed for the 2018 heat wave in Chapter 8. And from this analysis it turned out that diabatic processes in the planetary boundary layer are a major source of possible errors in the forecasting systems. For this reason, it would be interesting to perform sensitivity experiments how certain boundary layer processes, e.g. entrainment, vertical mixing, or the partition between latent and surface sensible heat fluxes, affect 2-m temperatures and therefore the severity of a heat wave. Currently, ECWMF is drawing much attention on the coupling between the lower troposphere and the underlying surface, since this is relevant for predictions of surface weather (Magnusson and Sandu, 2019). ECMWF plans measurement campaigns and better exploitation of existing datasets (Magnusson and Sandu, 2019), and therefore, results from Chapter 8 can contribute to this plans.

In addition to the analysis of high near-surface temperatures from Chapter 6, it would be interesting to find cases, where the large-scale setting (i.e. ridge) is conducive to a heat wave, but the surface temperatures were not high. A comparison of the Lagrangian processes leading to heat waves in other areas (e.g. tropics, polar regions) would complete the analysis on the development of high near-surface temperatures during heat waves. Furthermore, the results from Chapter 6 imply that future changes in heat waves, over and above the background thermodynamic warming, may be affected by potential changes in the associated dynamical processes, in particular in the strength of the subsidence. It is therefore worth applying the Lagrangian framework to climate models and to quantify the contributions of diabatic heating near the surface and subsidence to the formation of high

near-surface temperature extremes in different parts of the globe in a warmer climate. In addition, the results suggest that ”event-self propagation” may be important for western Russia and, to a lesser extent, for Greece/Italy. Recently, Schumacher et al. (2019) revealed that drought conditions upwind of heat waves can sharply increase the local temperature due to transport of air that was heated by remote surface sensible heat fluxes. It is well known that local surface conditions impact on near-surface temperatures during heat waves (subsection 2.2.5), but remote influences of surface conditions are still quite new in the literature. It should therefore be tested how remote surface conditions impact on local temperatures and whether this influence depends on the longevity, severity or other properties of heat waves.

The results from the analysis of upper-tropospheric anticyclones associated with heat waves in Chapter 7 have relevant implications for both weather and climate dynamics. Diabatic processes affect the life cycle of Rossby wave packets and a misrepresentation of these processes can lead to reduced predictability (Rodwell et al., 2013). Grams et al. (2018) showed that a misrepresented warm conveyor belt in an upstream trough led to misforecasts in the onset of blocking situations over Europe. Also, Rodwell et al. (2013) pointed out that convective situations in eastern North America led to a forecast bust over Europe. When considering a higher moisture content in the lower troposphere in a generally warmer world (Held and Soden, 2006), the latent heat release in cyclones or convective systems may increase. The stronger latent heat release stimulates the ascent of air streams that produce more significant negative PV anomalies in the upper troposphere (Madonna et al., 2014). Hence, model experiments quantifying the amplitude and the size of the upper-tropospheric anticyclones subject to a changing moisture content would be helpful to estimate the influence of global warming on the dynamics of European heat waves.

A

Appendix

A.1 Processes leading to high near-surface temperatures

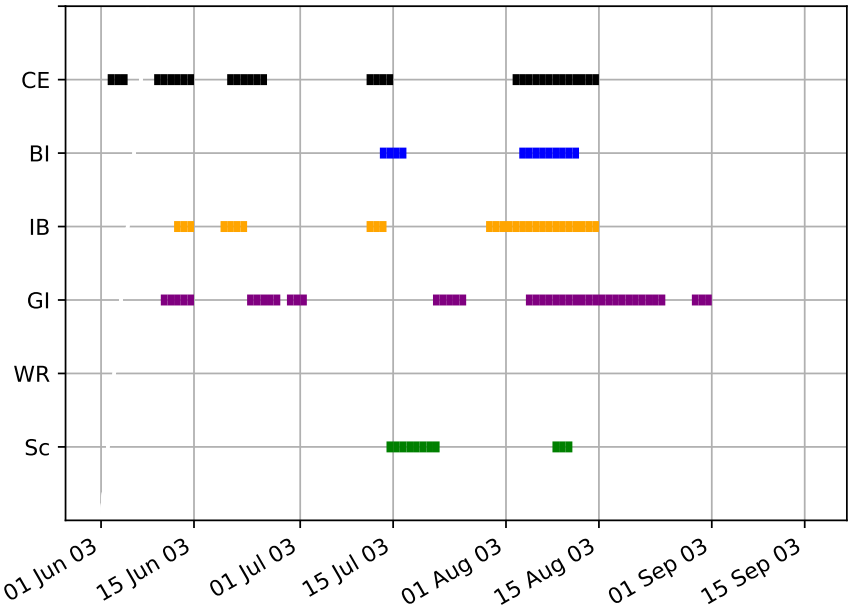

Figure A1.1: Heat wave occurrence in 2003. Colours represent the defined regions (CE: Central Europe; BI: British Isles; IB: Iberian Peninsula; GI: Greece/Italy; WR: western Russia; Sc: Scandinavia).

Table A1.1: Top 10 heat waves in Central Europe, sorted by magnitude. The area represents the daily average of the affected area during a heat wave, the magnitude represents the daily average of the summed magnitude as defined by the HWMId.

Onset			Decay			Characteristics		
Year	**Month**	**Day**	**Year**	**Month**	**Day**	**Duration [d]**	**Area [%]**	**Magnitude**
2003	8	2	2003	8	14	13	45.8	86.7
2015	6	30	2015	7	7	8	42.2	66.4
2010	7	8	2010	7	12	5	42.7	47.4
1998	8	8	1998	8	12	5	31.9	44.6
1992	8	6	1992	8	10	5	28.2	32.4
1994	7	22	1994	8	1	11	24.2	28.0
2013	7	25	2013	7	29	5	17.0	26.3
2006	7	16	2006	7	28	13	27.4	26.2
1994	8	3	1994	8	6	4	31.8	25.6
1983	7	5	1983	8	1	8	14.0	25.6

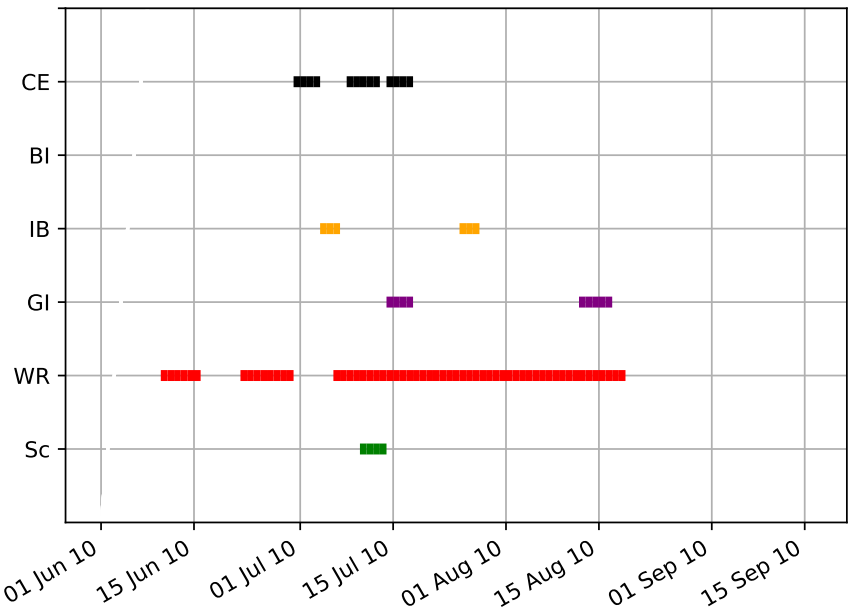

Figure A1.2: Heat wave occurrence in 2010. Colours represent the defined regions (CE: Central Europe; BI: British Isles; IB: Iberian Peninsula; GI: Greece/Italy; WR: western Russia; Sc: Scandinavia).

Table A1.2: Top 10 heat waves in Scandinavia, sorted by magnitude. The area represents the daily average of the affected area during a heat wave, the magnitude represents the daily average of the summed magnitude as defined by the HWMId.

Onset			Decay			Characteristics		
Year	**Month**	**Day**	**Year**	**Month**	**Day**	**Duration [d]**	**Area [%]**	**Magnitude**
1991	7	3	1991	7	9	7	30.4	46.7
2014	7	19	2014	7	29	11	32.3	43.2
1982	7	28	1982	8	8	12	29.1	41.9
2003	7	14	2003	7	21	8	27.8	40.6
1994	7	24	1994	7	29	6	24.3	35.6
1983	7	7	1983	7	12	6	30.4	31.9
2008	7	24	2008	8	1	9	24.8	31.5
1988	6	24	1988	6	29	6	20.8	27.7
2006	6	9	2006	6	13	5	23.6	22.7
1986	6	16	1986	6	18	3	25.7	20.9

Table A1.3: Top 10 heat waves in western Russia, sorted by magnitude. The area represents the daily average of the affected area during a heat wave, the magnitude represents the daily average of the summed magnitude as defined by the HWMId.

Onset			Decay			Characteristics		
Year	**Month**	**Day**	**Year**	**Month**	**Day**	**Duration [d]**	**Area [%]**	**Magnitude**
2010	7	6	2010	8	18	44	63.6	126.7
1981	7	20	1981	7	22	3	37.8	95.1
1998	6	9	1998	6	16	8	54.1	68.3
2010	6	22	2010	6	29	8	52.6	67.5
2008	8	12	2008	8	19	8	55.8	61.4
2016	7	13	2016	7	18	6	42.7	58.6
1996	7	7	1996	7	14	8	46.6	58.0
2007	8	11	2007	8	27	17	43.0	41.6
2007	5	30	2007	6	1	3	45.5	40.5
1991	6	24	1991	7	3	10	41.0	40.0

Table A1.4: Top 10 heat waves in Greece/Italy, sorted by magnitude. The area represents the daily average of the affected area during a heat wave, the magnitude represents the daily average of the summed magnitude as defined by the HWMId.

Onset			Decay			Characteristics		
Year	**Month**	**Day**	**Year**	**Month**	**Day**	**Duration [d]**	**Area [%]**	**Magnitude**
2007	7	16	2007	7	25	10	29.4	51.8
1988	7	4	1988	7	9	6	21.7	31.4
1987	7	18	1987	7	26	9	21.7	28.0
2000	7	2	2000	7	8	7	15.4	22.8
2012	8	18	2012	8	26	9	17.2	21.3
1982	6	23	1982	6	27	5	15.5	21.2
1985	7	28	1985	7	31	4	14.9	21.0
2012	8	3	2012	8	9	7	16.9	20.5
2007	6	21	2007	6	27	7	15.1	20.3
1998	7	31	1998	8	5	6	19.1	18.3

Table A1.5: Top 10 heat waves in the Iberian Peninsula, sorted by magnitude. The area represents the daily average of the affected area during a heat wave, the magnitude represents the daily average of the summed magnitude as defined by the HWMId.

Onset			Decay			Characteristics		
Year	**Month**	**Day**	**Year**	**Month**	**Day**	**Duration [d]**	**Area [%]**	**Magnitude**
1982	7	5	1982	7	8	4	23.4	27.1
2015	7	3	2015	7	9	7	18.6	26.2
2012	8	8	2012	8	12	5	16.4	26.0
2003	7	29	2003	8	14	17	20.6	23.3
2015	6	26	2015	6	30	5	17.7	20.1
1995	7	17	1995	7	24	8	14.8	19.5
2003	6	19	2003	6	22	4	14.3	18.4
1987	8	11	1987	8	16	6	15.1	15.5
2005	8	4	2005	8	7	4	12.7	13.8
2013	7	3	2013	7	9	7	14.0	13.6

Table A1.6: Top 10 heat waves in the British Isles, sorted by magnitude. The area represents the daily average of the affected area during a heat wave, the magnitude represents the daily average of the summed magnitude as defined by the HWMId.

Onset			Decay			Characteristics		
Year	**Month**	**Day**	**Year**	**Month**	**Day**	**Duration [d]**	**Area [%]**	**Magnitude**
1990	8	1	1990	8	4	4	15.0	41.4
2006	7	15	2006	7	21	7	20.4	32.5
1995	8	14	1995	8	22	9	21.8	24.8
1983	7	6	1983	7	16	11	16.7	24.8
2003	8	3	2003	8	11	9	15.2	23.0
2003	7	13	2003	7	16	4	15.7	19.1
1995	6	22	1995	6	30	9	14.2	17.7
1995	7	25	1995	8	5	12	15.1	17.5
1989	6	16	1989	6	20	5	14.9	14.7
1984	8	17	1984	8	22	6	15.7	14.6

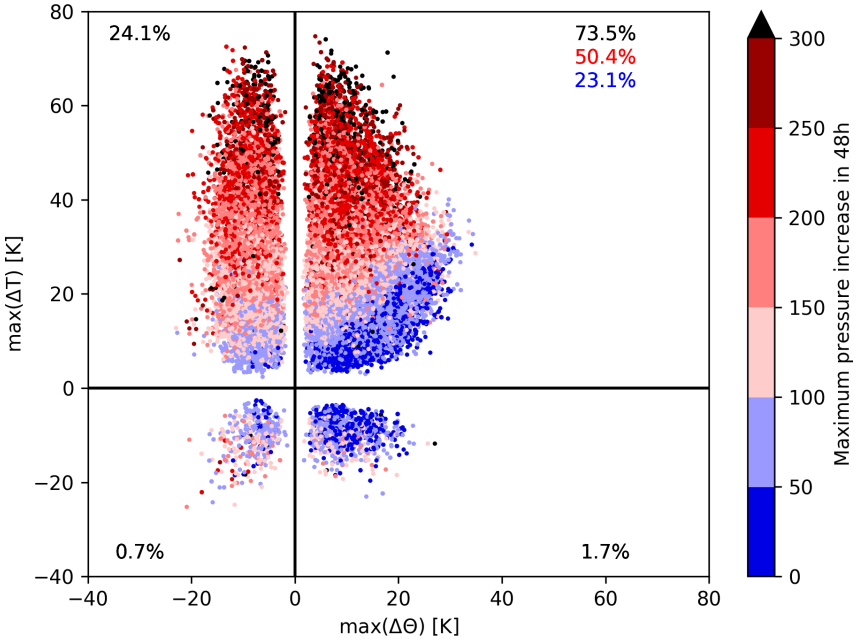

Figure A1.3: Maximum temperature (ΔT_{max}, in K) and maximum potential temperature ($\Delta\theta_{\text{max}}$, in K) changes along the trajectories for heat waves in Scandinavia. The colours indicate the maximum pressure increase in a 48-hour window. The numbers in the quadrants denote the numbers of trajectories of each cluster: in black (irrespective of descend rate), in blue (descent $\leq$ 100 hPa in 48 h, only upper right quadrant), in red (descent $>$ 100 hPa in 48 h, only upper right quadrant).

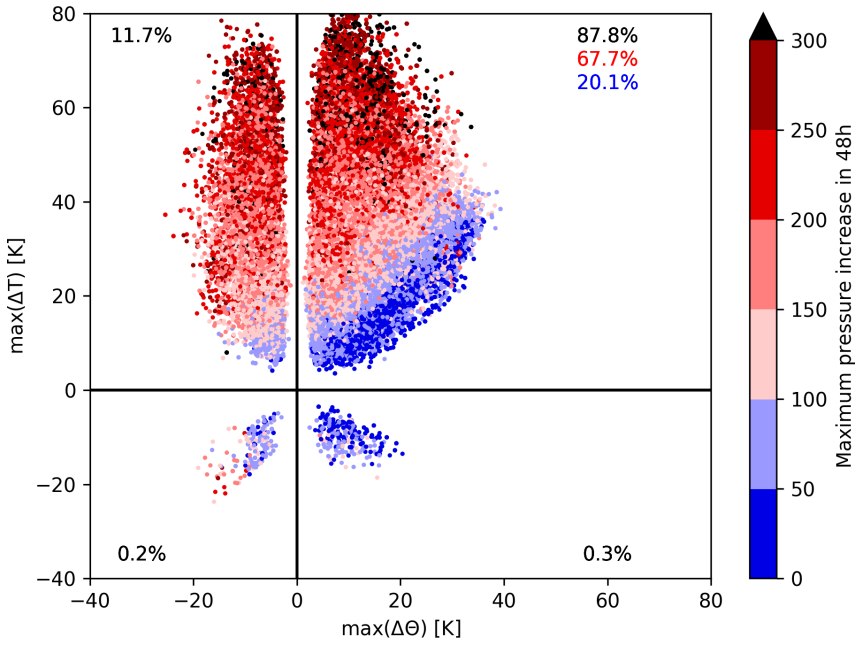

Figure A1.4: Same as Fig. A1.3, but for western Russia.

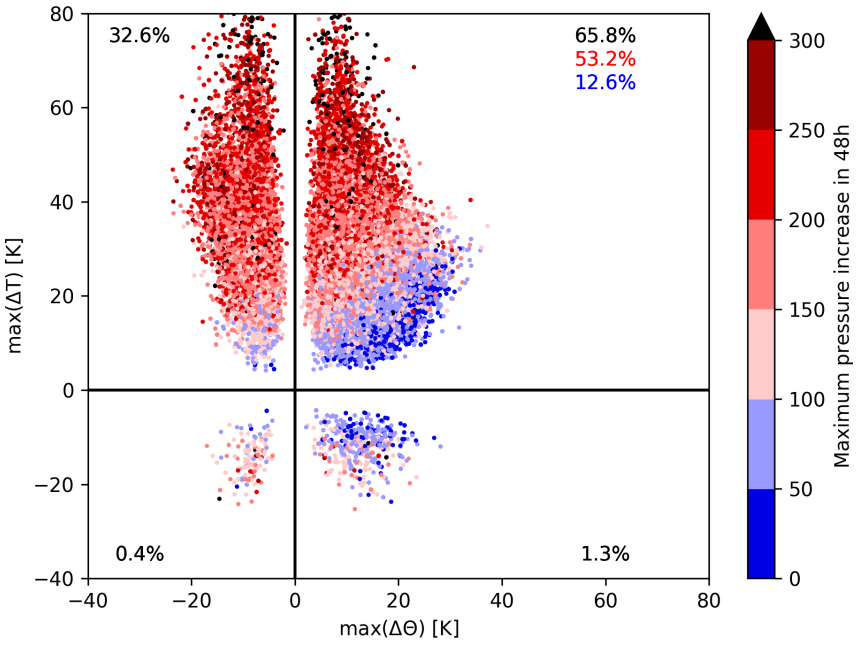

Figure A1.5: Same as Fig. A1.3, but for Greece/Italy.

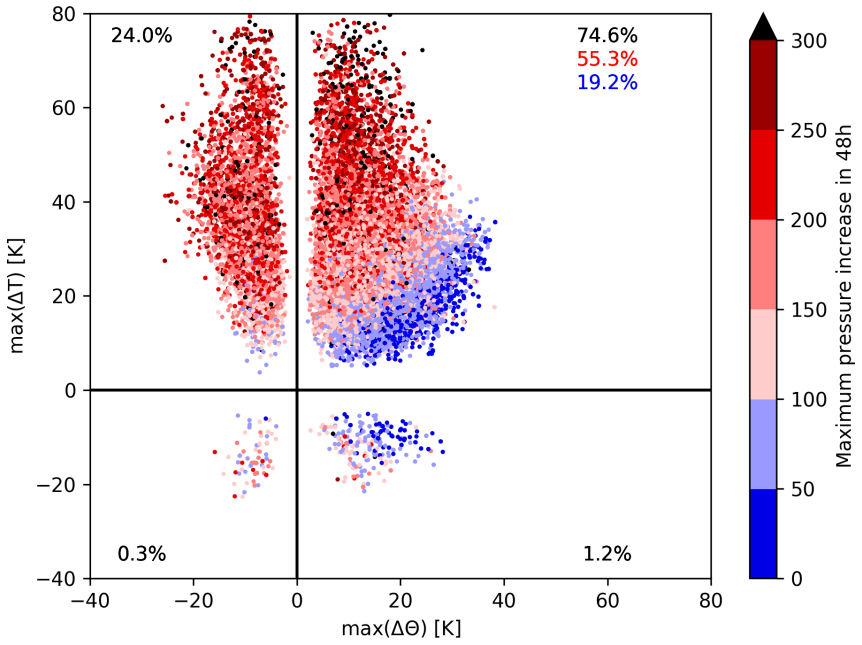

Figure A1.6: Same as Fig. A1.3, but for the Iberian Peninsula.

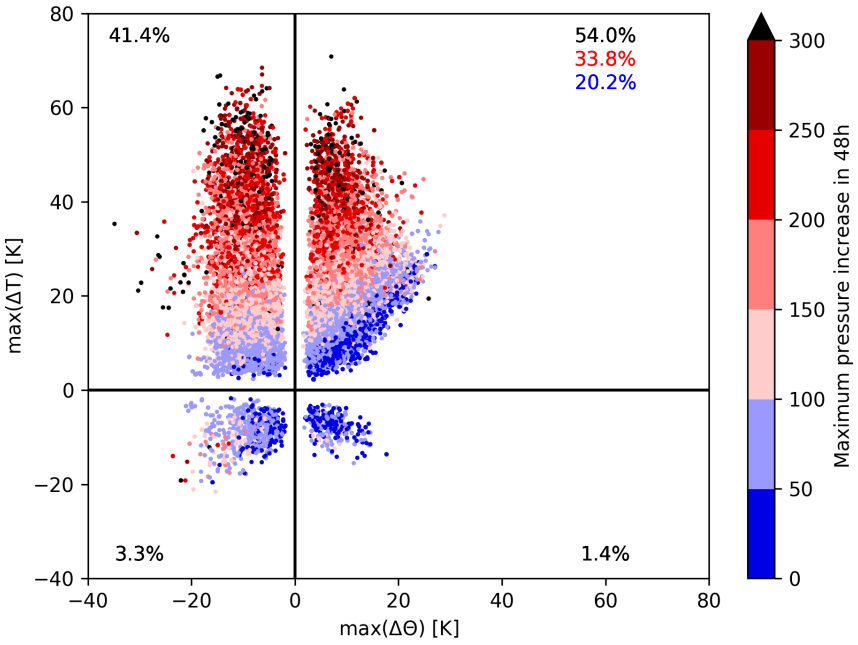

Figure A1.7: Same as Fig. A1.3, but for the British Isles.

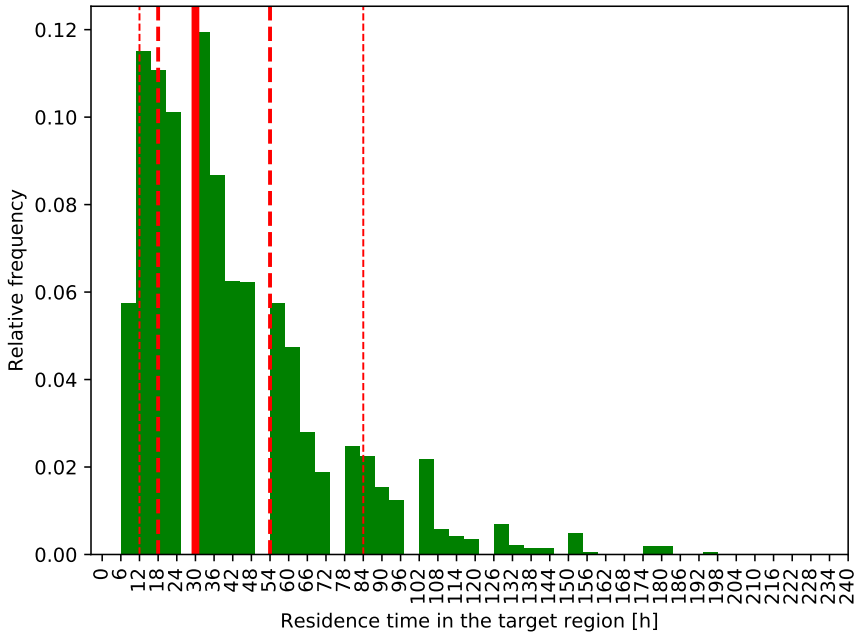

Figure A1.8: Residence time of trajectories during the extreme heat wave in the first to weeks of August 2003 over Central Europe. The solid line represents the median, the thick dashed line represents the 25th and 75th percentile, the thin dashed line the 10th and 90th percentile.

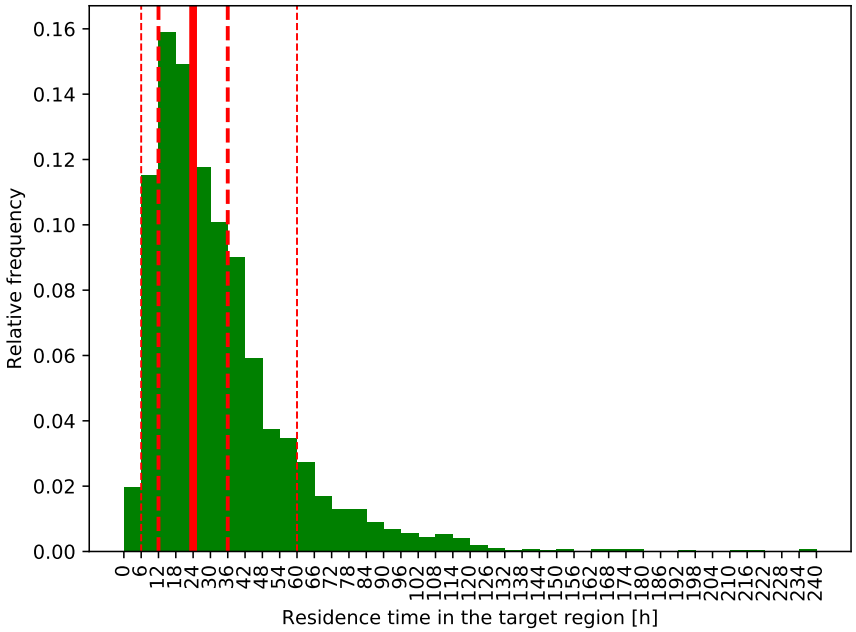

Figure A1.9: Residence time of trajectories during the extreme heat wave of 2010 over western Russia. The solid line represents the median, the thick dashed line represents the 25th and 75th percentile, the thin dashed line the 10th and 90th percentile.

A.2 Processes leading to upper-tropospheric anticyclones

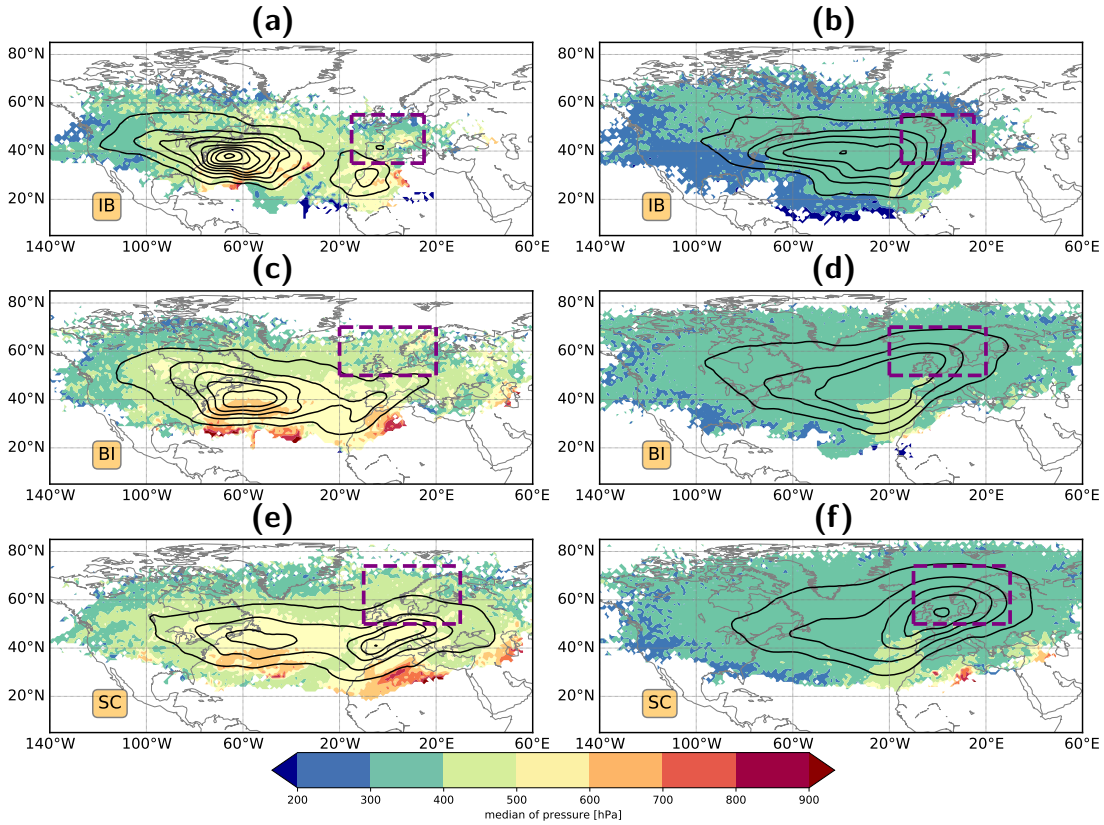

Figure A2.1: Spatial distribution of diabatically heated (left) and cooled (right) trajectories three days prior to arrival in the upper-tropospheric anticyclones for (a,b) Iberian Peninsula (IB), (c,d) British Isles (BI) and (e,f) Scandinavia (SC). The colours indicate the median pressure of air parcels and contours display the air parcel density (starting from 1‰ per 10^5 km^2 in 2‰ increments). The dashed purple boxes represent the area in which upper-tropospheric anticyclones are associated with heat waves (cf. section 7.1.1 and Fig. 7.1).

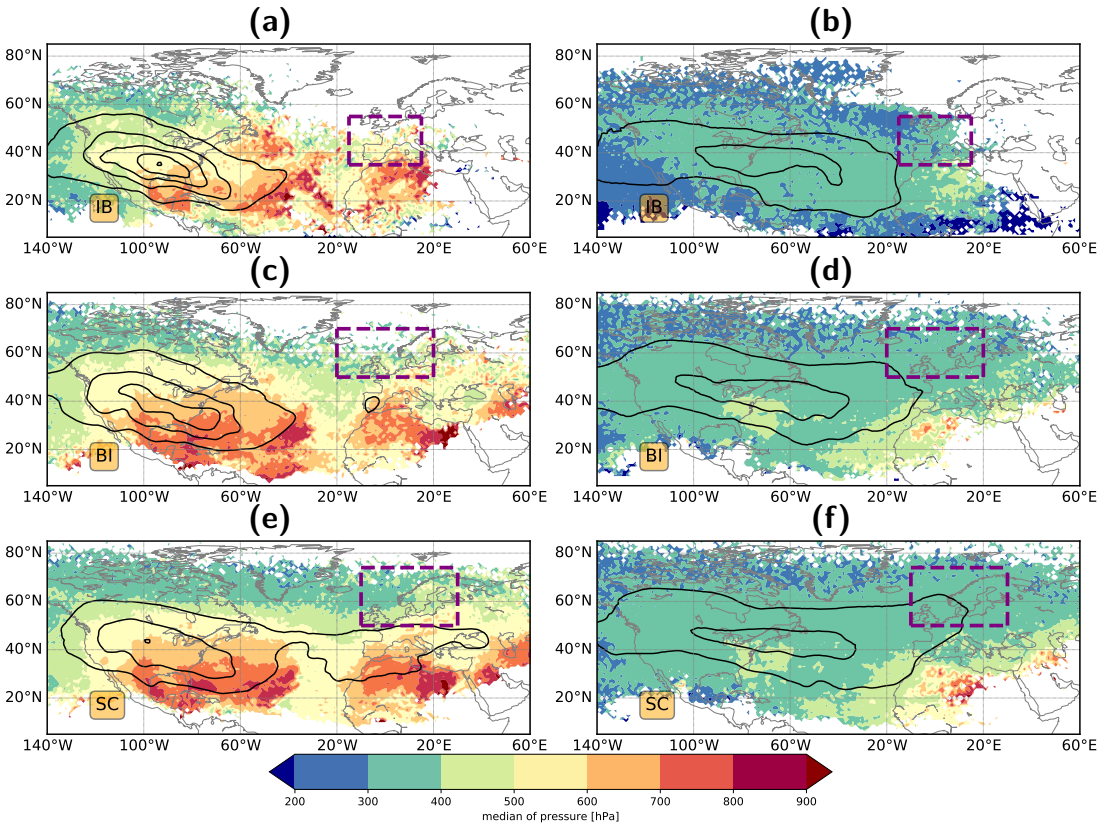

Figure A2.2: Same as Fig. A2.1, but seven days prior to arrival.

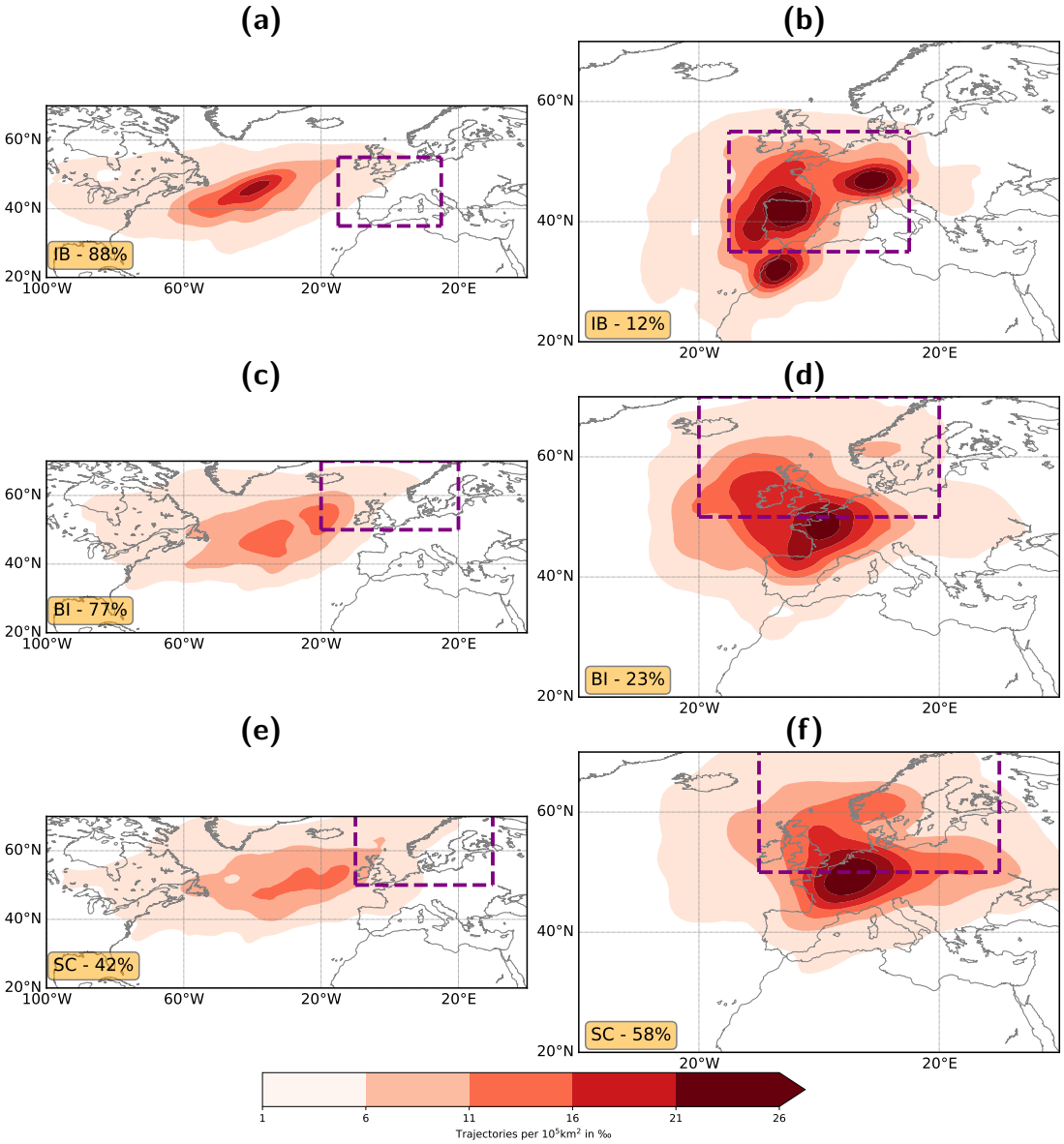

Figure A2.3: Geographic location of the maximum diabatic heating along trajectories for the remote (left column) and nearby heating branch (right column) during the last three days prior to reaching upper-tropospheric anticyclones above the Iberian Peninsula (IB), British Isles (BI) and Scandinavia (SC). The percentages in the orange boxes denote the fraction of the remote/nearby heating branch with respect to the whole heating branch. The dashed purple boxes are as in Fig. A2.1.

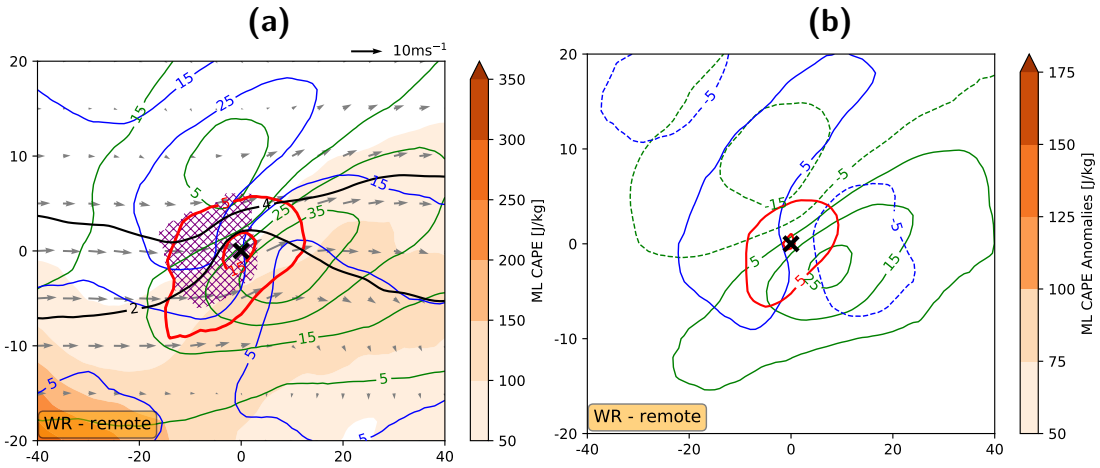

Figure A2.4: Composites around the position of maximum diabatic heating of the trajectories in the remote heating branch reaching upper-tropospheric anticyclones above western Russia. (a): Frequencies of extratropical cyclones (blue), blocks (green) and warm conveyor belts (red) starting from 5% in 10% increments. The orange shading shows the ML CAPE (in $\mathrm{J\,kg^{-1}}$) and the arrows the wind at 800 hPa. Black contours indicate PV (2 and 4 PVU contours) at 330 K. The purple hatching marks the region where the stratiform precipitation exceeds the convective precipitation (only for areas with total precipitation $\geq 2\,\mathrm{mm\,d^{-1}}$). (b) Anomalies of cyclone (blue), blocking (green) and warm conveyor belt (red) frequency.

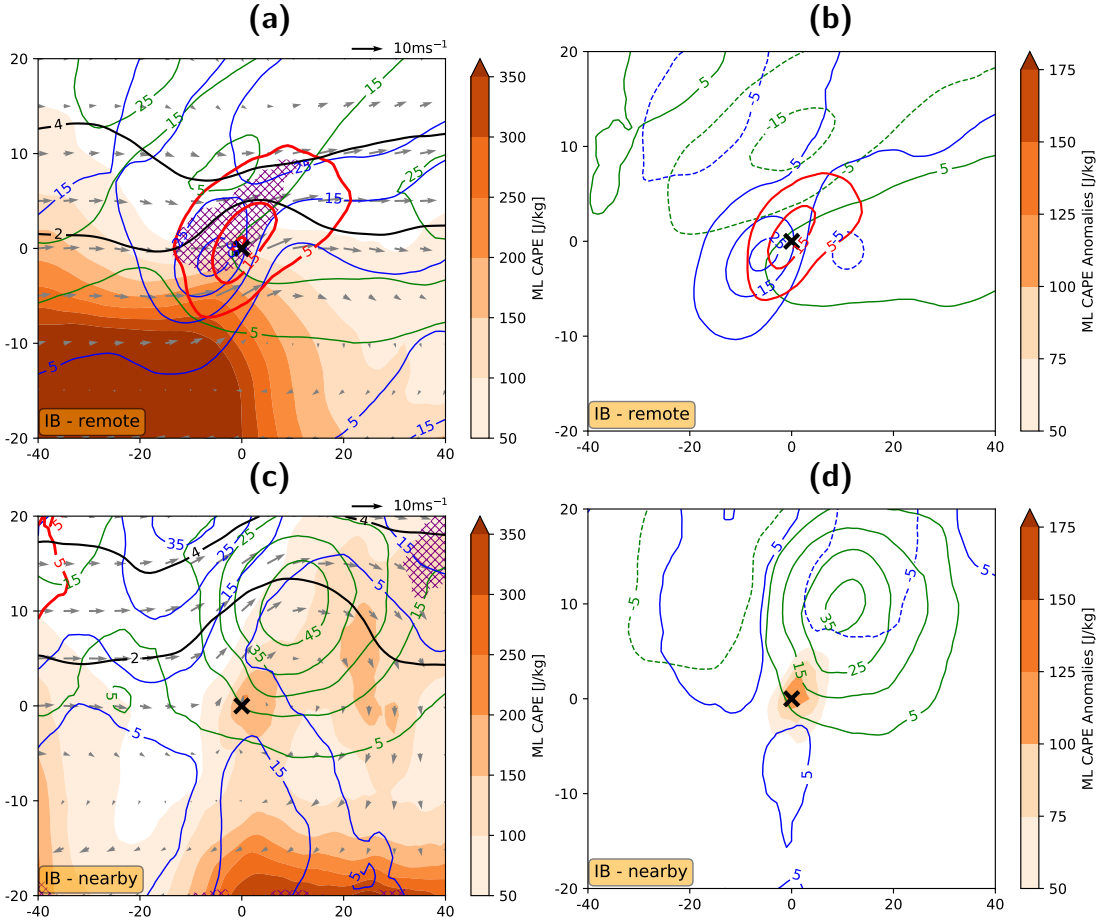

Figure A2.5: Same as Fig. A2.4, but for the remote (upper row) and nearby heating branch (lower row) reaching anticyclones over the Iberian Peninsula. Absolute frequencies are shown in (a) and (c); anomalies in (b) and (d). Note that the purple hatching in (a) marks the region where the stratiform precipitation exceeds the convective precipitation, in contrast to (c), where the purple hatching marks the region, where convective exceeds stratiform precipitation. Orange shading in (d) shows ML CAPE anomalies (in J kg^{-1}).

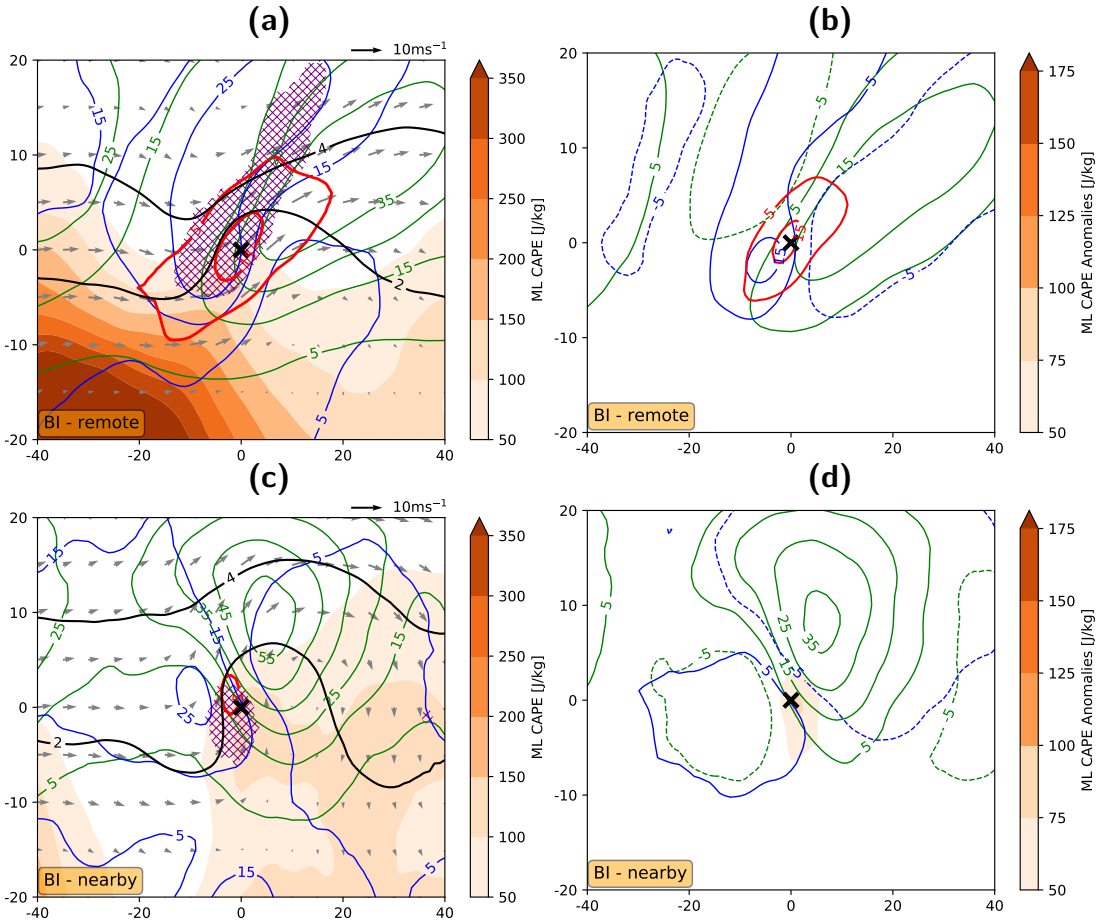

Figure A2.6: Same as Fig. A2.5, but for the British Isles.

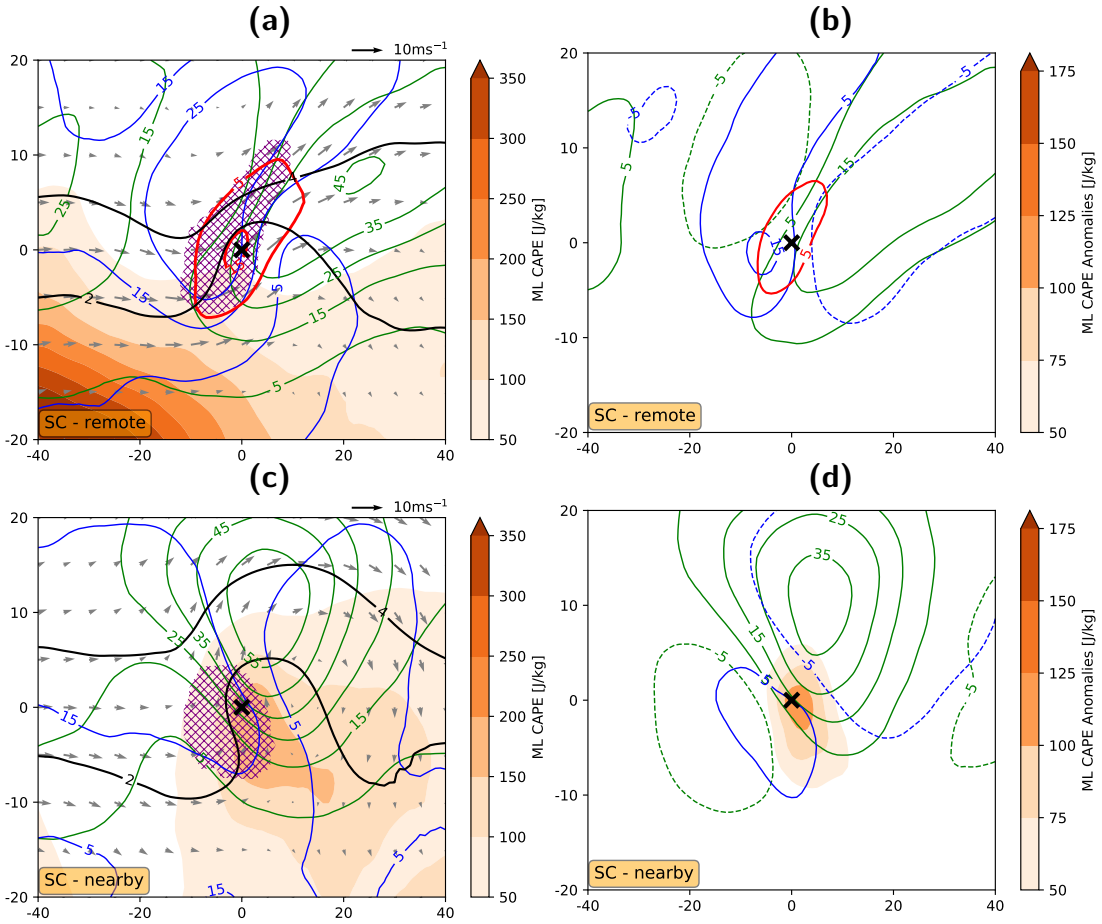

Figure A2.7: Same as Fig. A2.5, but for Scandinavia.

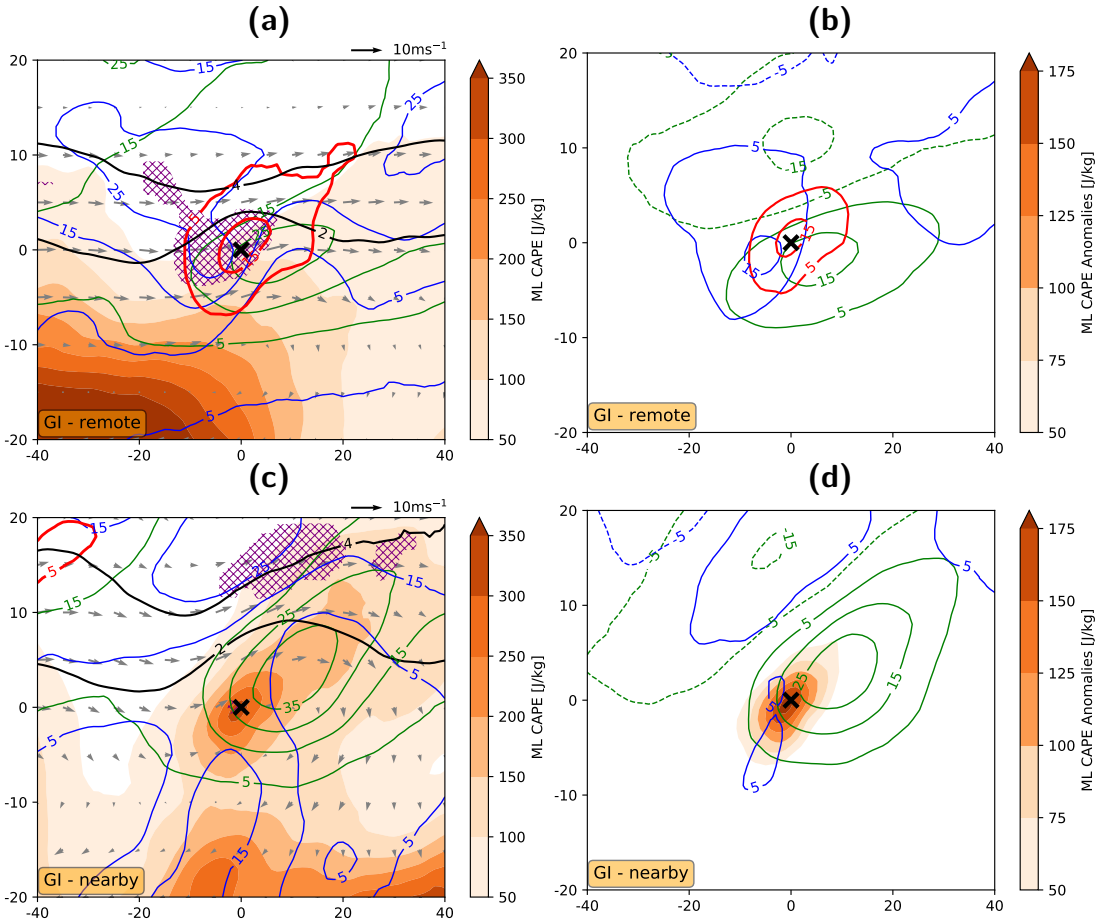

Figure A2.8: Same as Fig. A2.5, but for Greece/Italy.

Bibliography

Alexander, L. V., Zhang, X., Peterson, T. C., Caesar, J., Gleason, B., Klein Tank, A. M. G., Haylock, M., Collins, D., Trewin, B., Rahimzadeh, F., Tagipour, A., Rupa Kumar, K., Revadekar, J., Griffiths, G., Vincent, L., Stephenson, D. B., Burn, J., Aguilar, E., Brunet, M., Taylor, M., New, M., Zhai, P., Rusticucci, M., and Vazquez-Aguirre, J. L. Global observed changes in daily climate extremes of temperature and precipitation. *Journal of Geophysical Research: Atmospheres*, 111(D5), 2006. doi: 10.1029/2005JD006290.

Alexander, L. Extreme heat rooted in dry soils. *Nature Geoscience*, 4:12–13, 2011. doi: 10.1038/ngeo1045.

American Meteorological Society. Predictability. *Glossary of Meteorology*, 2012. URL `http://glossary.ametsoc.org/wiki/Predictability`. last accessed: 21 April 2020.

Barriopedro, D., García-Herrera, R., and Trigo, R. Application of blocking diagnosis methods to General Circulation Models. Part I: a novel detection scheme. *Climate Dynamics*, 35:1373–1391, 2010. doi: 10.1007/s00382-010-0767-5.

Baumgart, M. and Riemer, M. Processes governing the amplification of ensemble spread in a medium-range forecast with large forecast uncertainty. *Quarterly Journal of the Royal Meteorological Society*, 145(724):3252–3270, 2019. doi: 10.1002/qj.3617.

Berrisford, P., Dee, D., Poli, P., Brugge, R., Fielding, K., Fuentes, M., Kallberg, P., Kobayashi, S., Uppala, S., and Simmons, A. The ERA-Interim archive, version 2.0. 2011.

Bieli, M., Pfahl, S., and Wernli, H. A Lagrangian investigation of hot and cold temperature extremes in Europe. *Quarterly Journal of the Royal Meteorological Society*, 141 (686):98–108, 2015. doi: 10.1002/qj.2339.

Binder, H., Boettcher, M., Grams, C. M., Joos, H., Pfahl, S., and Wernli, H. Exceptional Air Mass Transport and Dynamical Drivers of an Extreme Wintertime Arctic Warm

Event. *Geophysical Research Letters*, 44(23):12,028–12,036, 2017. doi: 10.1002/2017GL075841.

Black, E., Blackburn, M., Harrison, G., Hoskins, B., and Methven, J. Factors contributing to the summer 2003 European heatwave. *Weather*, 59(8):217–223, 2004. doi: 10.1256/wea.74.04.

Boschat, G., Pezza, A., Simmonds, I., Perkins, S., Cowan, T., and Purich, A. Large scale and sub-regional connections in the lead up to summer heat wave and extreme rainfall events in eastern Australia. *Climate Dynamics*, 44(7-8):1823–1840, 2015. doi: 10.1007/s00382-014-2214-5.

Browning, K. A., Hardman, M. E., Harrold, T. W., and Pardoe, C. W. The structure of rainbands within a mid-latitude depression. *Quarterly Journal of the Royal Meteorological Society*, 99(420):215–231, 1973. doi: 10.1002/qj.49709942002.

Brunner, L., Schaller, N., Anstey, J., Sillmann, J., and Steiner, A. K. Dependence of present and future European temperature extremes on the location of atmospheric blocking. *Geophysical Research Letters*, 45(12):6311–6320, 2018. doi: 10.1029/2018GL077837.

BSH. Press release of the Federal Maritime and Hydrographic Agency (BSH) of Germany: a record warmth left its mark in the North Sea (in German). 2016. URL `http://www.bsh.de/de/Das_BSH/Presse/Pressearchiv/Pressemitteilungen2016/Pressemitteilung17-2016.pdf`. last accessed: 30 November 2017.

Carlson, T. N. *Mid-latitude Weather Systems*. Routledge, New York, 1994. 507 pp.

Cassou, C., Terray, L., and Phillips, A. S. Tropical Atlantic influence on European heatwaves. *Journal of Climate*, 18:2805–2811, 2005. doi: 10.1175/JCLI3506.1.

Cattiaux, J., Vautard, R., Cassou, C., Yiou, P., Masson-Delmotte, V., and Codron, F. Winter 2010 in Europe: A cold extreme in a warming climate. *Geophysical Research Letters*, 37(20), 2010. doi: 10.1029/2010GL044613.

Chan, P.-W., Hassanzadeh, P., and Kuang, Z. Evaluating indices of blocking anticyclones in terms of their linear relations with surface hot extremes. *Geophysical Research Letters*, 46(9):4904–4912, 2019. doi: 10.1029/2019GL083307.

Chang, F.-C. and Wallace, J. M. Meteorological Conditions during Heat Waves and Droughts in the United States Great Plains. *Monthly Weather Review*, 115(7):1253–1269, 1987. doi: 10.1175/1520-0493(1987)115⟨1253:MCDHWA⟩2.0.CO;2.

Chung, U., Gbegbelegbe, S., Shiferaw, B., Robertson, R., Yun, J. I., Tesfaye, K., Hoogenboom, G., and Sonder, K. Modeling the effect of a heat wave on maize production in the USA and its implications on food security in the developing world. *Weather and Climate Extremes*, 5-6:67 – 77, 2014. doi: 10.1016/j.wace.2014.07.002.

Collins, M., Knutti, R., Arblaster, J., Dufresne, J.-L., Fichefet, T., Friedlingstein, P., Gao, X., Gutowski, W. J., Johns, T., Krinner, G., Shongwe, M., Tebaldi, C., Weaver, A., and Wehner, M. Long-term climate change: projections, commitments and irreversibility. In *Climate Change 2013 – The Physical Science Basis: Contribution of Working Group I to the Fifth Assessment Report of the Intergovernmental Panel on Climate Change*. [Stocker, T.F., D. Qin, G.-K. Plattner, M. Tignor, S.K. Allen, J. Boschung, A. Nauels, Y. Xia, V. Bex and P.M. Midgley (eds.)]. Cambridge University Press, Cambridge, United Kingdom and New York, NY, USA, pp. 1029-1136, 2013.

Colucci, S. J. Explosive Cyclogenesis and Large-Scale Circulation Changes: Implications for Atmospheric Blocking. *Journal of the Atmospheric Sciences*, 42(24):2701–2717, 1985. doi: 10.1175/1520-0469(1985)042⟨2701:ECALSC⟩2.0.CO;2.

Croci-Maspoli, M., Schwierz, C., and Davies, H. C. A Multifaceted Climatology of Atmospheric Blocking and Its Recent Linear Trend. *Journal of Climate*, 20(4):633–649, 2007. doi: 10.1175/JCLI4029.1.

D'Andrea, F., Provenzale, A., Vautard, R., and De Noblet-Decoudré, N. Hot and cool summers: Multiple equilibria of the continental water cycle. *Geophysical Research Letters*, 33(24), 2006. doi: 10.1029/2006GL027972.

De Perez, E. C., Van Aalst, M., Bischiniotis, K., Mason, S., Nissan, H., Pappenberger, F., Stephens, E., Zsoter, E., and Van Den Hurk, B. Global predictability of temperature extremes. *Environmental Research Letters*, 13(5):054017, 2018.

Dee, D. P., Uppala, S. M., Simmons, A. J., Berrisford, P., Poli, P., Kobayashi, S., Andrae, U., Balmaseda, M. A., Balsamo, G., Bauer, P., Bechtold, P., Beljaars, A. C., van de Berg, L., Bidlot, J., Bormann, N., Delsol, C., Dragani, R., Fuentes, M., Geer, A. J., Haimberger, L., Healy, S. B., Hersbach, H., Hólm, E. V., Isaksen, L., Kållberg, P., Köhler, M., Matricardi, M., Mcnally, A. P., Monge-Sanz, B. M., Morcrette, J. J., Park, B. K., Peubey, C., de Rosnay, P., Tavolato, C., Thépaut, J. N., and Vitart, F. The ERA-Interim reanalysis: Configuration and performance of the data assimilation system. *Quarterly Journal of the Royal Meteorological Society*, 137(656):553–597, 2011. doi: 10.1002/qj.828.

Della-Marta, P., Luterbacher, J., von Weissenfluh, H., Xoplaki, E., Brunet, M., and Wanner, H. Summer heat waves over western Europe 1880–2003, their relationship to large-scale forcings and predictability. *Climate Dynamics*, 29:251–275, 2007. doi: 10.1007/s00382-007-0233-1.

Dong, B., Sutton, R. T., Woollings, T., and Hodges, K. Variability of the North Atlantic summer storm track: mechanisms and impacts on European climate. *Environmental Research Letters*, 8(3):034037, 2013. doi: 10.1088/1748-9326/8/3/034037.

Dong, B., Sutton, R., Shaffrey, L., and Wilcox, L. The 2015 European heat wave. *Bulletin of the American Meteorological Society*, 97(12):S57–S62, 2016. doi: 10.1175/BAMS-D-16-0140.1.

Duchez, A., Frajka-Williams, E., Josey, S. A., Evans, D. G., Grist, J. P., Marsh, R., McCarthy, G. D., Sinha, B., Berry, D. I., and Hirschi, J. J. Drivers of exceptionally cold North Atlantic Ocean temperatures and their link to the 2015 European heat wave. *Environmental Research Letters*, 11(7):074004, 2016. doi: 10.1088/1748-9326/11/7/074004.

DWD. Hitzewelle Juli 2019 in Westeuropa – neuer nationaler Rekord in Deutschland. 2019. URL `https://www.dwd.de/DE/leistungen/besondereereignisse/temperatur/20190801_hitzerekord_juli2019.pdf?__blob=publicationFile&v=3`. last accessed: 03 April 2020.

Ertel, H. Ein neuer hydrodynamischer Wirbelsatz. *Meteorologische Zeitschrift*, 59:271–281, 1942.

Ferranti, L., Corti, S., and Janousek, M. Flow-dependent verification of the ECMWF ensemble over the Euro-Atlantic sector. *Quarterly Journal of the Royal Meteorological Society*, 141(688):916–924, 2015. doi: 10.1002/qj.2411.

Fink, A. H., Brucher, T., Kruger, A., Leckebusch, G. C., Pinto, J. G., and Ulbrich, U. The 2003 European summer heat waves and drought - synoptic diagnosis and impact. *Weather*, 59(8):209–216, 2004. doi: 10.1256/wea.73.04.

Fink, A. H., Engel, T., Ermert, V., van der Linden, R., Schneidewind, M., Redl, R., Afiesimama, E., Thiaw, W. M., Yorke, C., Evans, M., and Janicot, S. *Mean Climate and Seasonal Cycle*. John Wiley and Sons. Ltd, 2017. doi: 10.1002/9781118391297.ch1.

Fischer, E. M. and Schär, C. Consistent geographical patterns of changes in high-impact European heatwaves. *Nature Geoscience*, 3(6):398–403, 2010. doi: 10.1038/ngeo866.

Fischer, E. M., Seneviratne, S. I., Lüthi, D., and Schär, C. Contribution of land-atmosphere coupling to recent European summer heat waves. *Geophysical Research Letters*, 34(6):L06707, 2007. doi: 10.1029/2006GL029068.

Ford, T. W., Dirmeyer, P. A., and Benson, D. O. Evaluation of heat wave forecasts seamlessly across subseasonal timescales. *NPJ Climate and Atmospheric Science*, 1 (1):1–9, 2018. doi: 10.1038/s41612-018-0027-7.

Fragkoulidis, G., Wirth, V., Bossmann, P., and Fink, A. H. Linking Northern Hemisphere temperature extremes to Rossby wave packets. *Quarterly Journal of the Royal Meteorological Society*, 144(711):553–566, 2018. doi: 10.1002/qj.3228.

Frank, D., Reichstein, M., Bahn, M., Thonicke, K., Frank, D., Mahecha, M. D., Smith, P., van der Velde, M., Vicca, S., Babst, F., Beer, C., Buchmann, N., Canadell, J. G., Ciais, P., Cramer, W., Ibrom, A., Miglietta, F., Poulter, B., Rammig, A., Seneviratne, S. I., Walz, A., Wattenbach, M., Zavala, M. A., and Zscheischler, J. Effects of climate extremes on the terrestrial carbon cycle: concepts, processes and potential future impacts. *Global Change Biology*, 21(8):2861–2880, 2015. doi: 10.1111/gcb.12916.

Garcia-Herrera, R., Diaz, J., Trigo, R. M., Luterbacher, J., and Fischer, E. M. A review of the european summer heat wave of 2003. *Critical Reviews in Environmental Science and Technology*, 40(4):267–306, 2010. doi: 10.1080/10643380802238137.

Gilbert, N. Russia counts environmental cost of wildfires. *Nature*, 2010. doi: 10.1038/news.2010.404.

Grams, C. M., Wernli, H., Böttcher, M., Campa, J., Corsmeier, U., Jones, S. C., Keller, J. H., Lenz, C.-J., and Wiegand, L. The key role of diabatic processes in modifying the upper-tropospheric wave guide: a North Atlantic case-study. *Quarterly Journal of the Royal Meteorological Society*, 137(661):2174–2193, 2011. doi: 10.1002/qj.891.

Grams, C. M., Magnusson, L., and Madonna, E. An atmospheric dynamics perspective on the amplification and propagation of forecast error in numerical weather prediction models: A case study. *Quarterly Journal of the Royal Meteorological Society*, 144 (717):2577–2591, 2018. doi: 10.1002/qj.3353.

Green, J. S. A. The weather during July 1976: some dynamical considerations of the drought. *Weather*, 32(4):120–126, 1977. doi: 10.1002/j.1477-8696.1977.tb04532.x.

Green, J. S. A., Ludlam, F. H., and McIlveen, J. F. R. Isentropic relative-flow analysis and the parcel theory. *Quarterly Journal of the Royal Meteorological Society*, 92(392): 210–219, 1966. doi: 10.1002/qj.49709239204.

Grumm, R. H. The Central European and Russian heat event of July-August 2010. *Bulletin of the American Meteorological Society*, 92(10):1285–1296, 2011. doi: 10.1175/2011BAMS3174.1.

Haiden, T., Sandu, I., Balsamo, G., Arduini, G., and Beljaars, A. Addressing biases in near-surface forecasts. *ECMWF Newsletter*, 157:20–25, 2018.

Hall, R., Erdélyi, R., Hanna, E., Jones, J. M., and Scaife, A. A. Drivers of North Atlantic Polar Front jet stream variability. *International Journal of Climatology*, 35(8):1697–1720, 2015. doi: 10.1002/joc.4121.

Hantel, M. *Einführung Theoretische Meteorologie*. Springer-Verlag, 2013. 430 pp.

Harrold, T. W. Mechanisms influencing the distribution of precipitation within baroclinic disturbances. *Quarterly Journal of the Royal Meteorological Society*, 99(420):232–251, 1973. doi: 10.1002/qj.49709942003.

Hartmann, D. L., Tank, A. M. K., Rusticucci, M., Alexander, L. V., Brönnimann, S., Charabi, Y. A. R., Dentener, F. J., Dlugokencky, E. J., Easterling, D. R., Kaplan, A., Soden, B., Thorne, P., Wild, M., and Zhai, P. Observations: atmosphere and surface. In *Climate change 2013 the physical science basis: Working group I contribution to the fifth assessment report of the intergovernmental panel on climate change*. [Stocker, T.F., D. Qin, G.-K. Plattner, M. Tignor, S.K. Allen, J. Boschung, A. Nauels, Y. Xia, V. Bex and P.M. Midgley (eds.)]. Cambridge University Press, Cambridge, United Kingdom and New York, NY, USA, pp. 159-254, 2013.

Held, I. M. and Soden, B. J. Robust Responses of the Hydrological Cycle to Global Warming. *Journal of Climate*, 19(21):5686–5699, 2006. doi: 10.1175/JCLI3990.1.

Hillel, D. *Environmental soil physics: Fundamentals, applications, and environmental considerations*. Elsevier, 1998. 771 pp.

Hirschi, M., Seneviratne, S. I., Alexandrov, V., Boberg, F., Boroneant, C., Christensen, O. B., Formayer, H., Orlowsky, B., and Stepanek, P. Observational evidence for soil-moisture impact on hot extremes in southeastern Europe. *Nature Geoscience*, 4:17–21, 2011. doi: 10.1038/ngeo1032.

Holton, J. R. and Hakim, G. J. *An Introduction fo Dynamic Meteorology*. Elsevier Academic press, Oxford, 2013. 532 pp.

Horton, R. M., Mankin, J. S., Lesk, C., Coffel, E., and Raymond, C. A Review of Recent Advances in Research on Extreme Heat Events. *Current Climate Change Reports*, 2 (4):242–259, 2016. doi: 10.1007/s40641-016-0042-x.

Hoskins, B. J., McIntyre, M. E., and Robertson, A. W. On the use and significance of isentropic potential vorticity maps. *Quarterly Journal of the Royal Meteorological Society*, 111(470):877–946, 1985. doi: 10.1002/qj.49711147002.

Hoskins, B. Potential vorticity and the PV perspective. *Advances in Atmospheric Sciences*, 32:2–9, 2015. doi: 10.1007/s00376-014-0007-8.

Huang, J. and van den Dool, H. M. Monthly Precipitation-Temperature Relations and Temperature Prediction over the United States. *Journal of Climate*, 6(6):1111–1132, 1993. doi: 10.1175/1520-0442(1993)006⟨1111:MPTRAT⟩2.0.CO;2.

Hudson, D., Marshall, A. G., and Alves, O. Intraseasonal Forecasting of the 2009 Summer and Winter Australian Heat Waves Using POAMA. *Weather and Forecasting*, 26 (3):257–279, 2011. doi: 10.1175/WAF-D-10-05041.1.

Karl, T. R. and Quayle, R. G. The 1980 Summer Heat Wave and Drought in Historical Perspective. *Monthly Weather Review*, 109(10):2055–2073, 1981. doi: 10.1175/1520-0493(1981)109⟨2055:TSHWAD⟩2.0.CO;2.

Kornhuber, K., Osprey, S., Coumou, D., Petri, S., Petoukhov, V., Rahmstorf, S., and Gray, L. Extreme weather events in early summer 2018 connected by a recurrent hemispheric wave-7 pattern. *Environmental Research Letters*, 14(5):054002, 2019. doi: 10.1088/1748-9326/ab13bf.

Kyselý, J. Influence of the persistence of circulation patterns on warm and cold temperature anomalies in Europe: Analysis over the 20th century. *Global and Planetary Change*, 62(1):147–163, 2008. doi: 10.1016/j.gloplacha.2008.01.003.

Lackmann, G. *Midlatitude Synoptic Meteorology: Dynamics, Analysis and Forecasting*. American Meteorological Society, Boston, USA, 2011. 345 pp.

Lafore, J.-P., Flamant, C., Giraud, V., Guichard, F., Knippertz, P., Mahfouf, J.-F., Mascart, P., and Williams, E. Introduction to the AMMA Special Issue on 'Advances in understanding atmospheric processes over West Africa through the AMMA field campaign'. *Quarterly Journal of the Royal Meteorological Society*, 136(S1):2–7, 2010. doi: 10.1002/qj.583.

Lau, W. K. and Kim, K.-M. The 2010 Pakistan flood and Russian heat wave: Teleconnection of hydrometeorological extremes. *Journal of Hydrometeorology*, 13(1):392–403, 2012. doi: doi.org/10.1175/JHM-D-11-016.1.

Lavayasse, C., Naumann, G., Alfieri, L., Salamon, P., and Vogt, J. Predictability of the European heat and cold waves. *Climate Dynamics*, 52:2481–2495, 2018. doi: 10.1007/s00382-018-4273-5.

Lee, Y. Y. and Grotjahn, R. California Central Valley summer heat waves form two ways. *Journal of Climate*, 29(3):1201–1217, 2016. doi: 10.1175/JCLI-D-15-0270.1.

Madonna, E., Wernli, H., Joos, H., and Martius, O. Warm Conveyor Belts in the ERA-Interim Dataset (1979–2010). Part I: Climatology and Potential Vorticity Evolution. *Journal of Climate*, 27(1):3–26, 2014. doi: 10.1175/JCLI-D-12-00720.1.

Magnusson, L., Thorpe, A., Buizza, R., Rabier, F., and Nicolau, J. Predicting this year's European heat wave. *ECMWF Newsletter*, 145:4–5, 2015.

Magnusson, L., Ferranti, L., and Vamborg, F. Forecasting the 2018 European heatwave. *ECMWF Newsletter*, (157):2–3, 2018.

Magnusson, L. and Sandu, I. Experts review synergies between observational campaigns and weather forecasting. *ECMWF Newsletter*, 161:6–7, 2019.

Maier-Gerber, M., Pantillon, F., Di Muzio, E., Riemer, M., Fink, A. H., and Knippertz, P. Birth of the Biscane. *Weather*, 72(8):236–241, 2017. doi: 10.1002/wea.2995.

Marshall, A. G., Hudson, D., Wheeler, M. C., Alves, O., Hendon, H. H., Pook, M., and Risbey, J. S. Intra-seasonal drivers of extreme heat over Australia in observations and POAMA-2. *Climate Dynamics*, 43:1915–1937, 2014. doi: 10.1007/s00382-013-2016-1.

Martin, J. E. *Mid-Latitude Atmospheric Dynamics*. Wiley, West Sussex, England, 2006. 324 pp.

Mastrandrea, M. D., Field, C. B., Stocker, T. F., Edenhofer, O., Ebi, K. L., Frame, D. J., Held, H., Kriegler, E., Mach, K. J., Matschoss, P. R., Plattner, G.-K., Yohe, G., and Zwiers, F. Guidance note for lead authors of the IPCC fifth assessment report on consistent treatment of uncertainties. 2010. URL `http://www.ipcc.ch`. last accessed: 29 April 2020.

Matsueda, M. Predictability of Euro-Russian blocking in summer of 2010. *Geophysical Research Letters*, 38(6), 2011. doi: 10.1029/2010GL046557.

Meehl, G. A. and Tebaldi, C. More Intense, More Frequent, and Longer Lasting Heat Waves in the 21st Century. *Science*, 305(5686):994–997, 2004. doi: 10.1126/science.1098704.

Messori, G., Caballero, R., Bouchet, F., Faranda, D., Grotjahn, R., Harnik, N., Jewson, S., Pinto, J. G., Rivière, G., Woollings, T., and Yiou, P. An interdisciplinary approach to the study of extreme weather events: Large-scale atmospheric controls and insights from dynamical systems theory and statistical mechanics. *Bulletin of the American Meteorological Society*, 99(5):ES81–ES85, 2018. doi: 10.1175/BAMS-D-17-0296.1.

Miltenberger, A. K., Pfahl, S., and Wernli, H. An online trajectory module (version 1.0) for the nonhydrostatic numerical weather prediction model COSMO. *Geoscientific Model Development*, 6(6):1989–2004, 2013. doi: 10.5194/gmd-6-1989-2013.

Miralles, D. G., Teuling, A. J., Van Heerwaarden, C. C., and De Arellano, J. V. G. Mega-heatwave temperatures due to combined soil desiccation and atmospheric heat accumulation. *Nature Geoscience*, 7(5):345–349, 2014. doi: 10.1038/ngeo2141.

Miralles, D. G., Gentine, P., Seneviratne, S. I., and Teuling, A. J. Land-atmospheric feedbacks during droughts and heatwaves: state of the science and current challenges. *Annals of the New York Academy of Sciences*, 1436:19–35, 2019. doi: 10.1111/nyas.13912.

MunichRe. *TOPICS GEO Natural Catastrophes 2017*. Münchener Rückversicherungs-Gesellschaft, Munich, 2018. URL `https://www.munichre.com/site/touch-publications/get/documents_E711248208/mr/assetpool.shared/Documents/5_Touch/_Publications/TOPICS_GEO_2017-en.pdf`. 68pp., last accessed: 17 June 2019.

Nairn, J. and Fawcett, R. Defining heatwaves: heatwaves defined as a heat impact event servicing all community and business sectors in Australia. *CAWCR Technical report No 060. The Centre for Australian Weather and Climate Research A partnership between the Bureau of Meteorology and CSIRO*, 2013. 96 pp.

Oertel, A., Boettcher, M., Joos, H., Sprenger, M., and Wernli, H. Potential vorticity structure of embedded convection in a warm conveyor belt and its relevance for large-scale dynamics. *Weather and Climate Dynamics*, 1(1):127–153, 2020. doi: 10.5194/wcd-1-127-2020.

Owens, R. G. and Hewson, T. D. ECMWF Forecast User Guide. *ECMWF, Reading*, 2018. doi: 10.21957/m1cs7h. URL `https://confluence.ecmwf.int/display/FUG/Forecast+User+Guide`. last accessed: 26 March 2020.

Pante, G. and Knippertz, P. Resolving Sahelian thunderstorms improves mid-latitude weather forecasts. *Nature Communications*, 10(3487):1–9, 2019. doi: 10.1038/s41467-019-11081-4.

Pelly, J. L. and Hoskins, B. J. A New Perspective on Blocking. *Journal of the Atmospheric Sciences*, 60(5):743–755, 2003. doi: 10.1175/1520-0469(2003)060⟨0743:ANPOB⟩2.0.CO;2.

Pelly, J. L. and Hoskins, B. J. How well does the ECMWF Ensemble Prediction System predict blocking? *Quarterly Journal of the Royal Meteorological Society*, 129(590): 1683–1702, 2006. doi: 10.1256/qj.01.173.

Perkins, S. E. and Alexander, L. V. On the Measurement of Heat Waves. *Journal of Climate*, 26(13):4500–4517, 2013. doi: 10.1175/JCLI-D-12-00383.1.

Perkins, S. E., Alexander, L. V., and Nairn, J. R. Increasing frequency, intensity and duration of observed global heatwaves and warm spells. *Geophysical Research Letters*, 39(20):L20714, 2012. doi: 10.1029/2012GL053361.

Perkins, S. E. A review on the scientific understanding of heatwaves -Their measurement, driving mechanisms, and changes at the global scale. *Atmospheric Research*, 164-165: 242–267, 2015. doi: 10.1016/j.atmosres.2015.05.014.

Pezza, A., van Rensch, P., and Cai, W. Severe heat waves in Southern Australia: synoptic climatology and large scale connections. *Climate Dynamics*, 38:209–224, 2012. doi: 10.1007/s00382-011-1016-2.

Pfahl, S. Characterising the relationship between weather extremes in Europe and synoptic circulation features. *Natural Hazards and Earth System Sciences*, 14(6):1461–1475, 2014. doi: 10.5194/nhess-14-1461-2014.

Pfahl, S. and Wernli, H. Quantifying the relevance of atmospheric blocking for co-located temperature extremes in the Northern Hemisphere on (sub-)daily time scales. *Geophysical Research Letters*, 39(12):L12807, 2012. doi: 10.1029/2012GL052261.

Pfahl, S., Schwierz, C., Croci-Maspoli, M., Grams, C. M., and Wernli, H. Importance of latent heat release in ascending air streams for atmospheric blocking. *Nature Geoscience*, 8(8):610–614, 2015. doi: 10.1038/ngeo2487.

Pomroy, H. R. and Thorpe, A. J. The Evolution and Dynamical Role of Reduced Upper-Tropospheric Potential Vorticity in Intensive Observing Period One of FASTEX. *Monthly Weather Review*, 128(6):1817–1834, 2000. doi: 10.1175/1520-0493(2000)128⟨1817:TEADRO⟩2.0.CO;2.

Quandt, L.-A., Keller, J. H., Martius, O., and Jones, S. C. Forecast Variability of the Blocking System over Russia in Summer 2010 and Its Impact on Surface Conditions. *Weather and Forecasting*, 32(1):61–82, 2017. doi: 10.1175/WAF-D-16-0065.1.

Quesada, B., Vautard, R., Yiou, P., Hirschi, M., and Seneviratne, S. I. Asymmetric European summer heat predictability from wet and dry southern winters and springs. *Nature Climate Change*, 2:736–741, 2012. doi: 10.1038/nclimate1536.

Quinting, J. F. and Reeder, M. J. Southeastern Australian Heat Waves from a Trajectory Viewpoint. *Monthly Weather Review*, 145(10):4109–4125, 2017. doi: 10.1175/MWR-D-17-0165.1.

Raveh-Rubin, S. Dry intrusions: Lagrangian climatology and dynamical impact on the planetary boundary layer. *Journal of Climate*, 30(17):6661–6682, 2017. doi: 10.1175/JCLI-D-16-0782.1.

Robine, J.-M., Cheung, S. L. K., Roy, S. L., Oyen, H. V., Griffiths, C., Michel, J.-P., and Herrmann, F. R. Death toll exceeded 70,000 in Europe during the summer of 2003. *Comptes Rendus Biologies*, 331(2):171 – 178, 2008. doi: 10.1016/j.crvi.2007.12.001. Dossier : Nouveautés en cancérogenèse / New developments in carcinogenesis.

Robinson, A., Haley, P., Lermusiaux, P., and Leslie, W. Predictive skill, predictive capability and predictability in ocean forecasting. *OCEANS'02 MTS/IEEE*, 2:787–794, 2002.

Robinson, P. J. On the Definition of a Heat Wave. *Journal of Applied Meteorology*, 40 (4):762–775, 2001. doi: 10.1175/1520-0450(2001)040⟨0762:OTDOAH⟩2.0.CO;2.

Rodwell, M. J., Magnusson, L., Bauer, P., Bechtold, P., Bonavita, M., Cardinali, C., Diamantakis, M., Earnshaw, P., Garcia-Mendez, A., Isaksen, L., Källén, E., Klocke, D., Lopez, P., McNally, T., Persson, A., Prates, F., and Wedi, N. Characteristics of Occasional Poor Medium-Range Weather Forecasts for Europe. *Bulletin of the American Meteorological Society*, 94(9):1393–1405, 2013. doi: 10.1175/BAMS-D-12-00099.1.

Rossby, C.-G. Planetary flow patterns in the atmosphere. *Quarterly Journal of the Royal Meteorological Society*, 66:68–87, 1940.

Röthlisberger, M., Pfahl, S., and Martius, O. Regional-scale jet waviness modulates the occurrence of midlatitude weather extremes. *Geophysical Research Letters*, 43(20): 10,989–10,997, 2016. doi: 10.1002/2016GL070944.

Russo, S., Sillmann, J., and Fischer, E. M. Top ten European heatwaves since 1950 and their occurrence in the coming decades. *Environmental Research Letters*, 10(12): 124003, 2015. doi: 10.1088/1748-9326/10/12/124003.

Sanders, F. and Gyakum, J. R. Synoptic-Dynamic Climatology of the "Bomb". *Monthly Weather Review*, 108(10):1589–1606, 1980. doi: 10.1175/1520-0493(1980)108⟨1589:SDCOT⟩2.0.CO;2.

Santos, J. A., Pfahl, S., Pinto, J. G., and Wernli, H. Mechanisms underlying temperature extremes in Iberia: A Lagrangian perspective. *Tellus, Series A: Dynamic Meteorology and Oceanography*, 67(1):26032, 2015. doi: 10.3402/tellusa.v67.26032.

Schaller, N., Sillmann, J., Anstey, J., Fischer, E. M., Grams, C. M., and Russo, S. Influence of blocking on Northern European and Western Russian heatwaves in large climate model ensembles. *Environmental Research Letters*, 13(5):054015, 2018. doi: 10.1088/1748-9326/aaba55.

Schubert, S., Wang, H., and Suarez, M. Warm Season Subseasonal Variability and Climate Extremes in the Northern Hemisphere: The Role of Stationary Rossby Waves. *Journal of Climate*, 24(18):4773–4792, 2011. doi: 10.1175/JCLI-D-10-05035.1.

Schumacher, D. L., Keune, J., Van Heerwaarden, C. C., de Arellano, J. V.-G., Teuling, A. J., and Miralles, D. G. Amplification of mega-heatwaves through heat torrents fuelled by upwind drought. *Nature Geoscience*, 12(9):712–717, 2019.

Schwierz, C., Croci-Maspoli, M., and Davies, H. C. Perspicacious indicators of atmospheric blocking. *Geophysical Research Letters*, 31(6):L06125, 2004. doi: 10.1029/2003GL019341.

Schär, C., Vidale, P. L., Lüthi, D., Frei, C., Häberli, C., Liniger, M. A., and Appenzeller, C. The role of increasing temperature variability in European summer heatwaves. *Nature*, 427:332–336, 2004. doi: 10.1038/nature02300.

Seneviratne, S., Nicholls, N., Easterling, D., Goodess, C., Kanae, S., Kossin, J., Luo, Y., Marengo, J., McInnes, K., Rahimi, M., Reichstein, M., Sorteberg, A., Vera, C., and Zhang, X. Changes in climate extremes and their impacts on the natural physical environment. [Field, C.B., V. Barros, T.F. Stocker, D. Qin, D.J. Dokken, K.L. Ebi, M.D. Mastrandrea, K.J. Mach, G.-K. Plattner, S.K. Allen,M. Tignor, and P.M. Midgley (eds.)]. A Special Report of Working Groups I and II of the Intergovernmental Panel on ClimateChange (IPCC). Cambridge University Press, Cambridge, UK, and New York, NY, USA, pp. 109-230, 2012.

Seneviratne, S. I., Corti, T., Davin, E. L., Hirschi, M., Jaeger, E. B., Lehner, I., Orlowsky, B., and Teuling, A. J. Investigating soil moisture–climate interactions in a changing climate: A review. *Earth-Science Reviews*, 99(3):125–161, 2010. doi: 10.1016/j.earscirev.2010.02.004.

Shukla, J. and Mintz, Y. Influence of Land-Surface Evapotranspiration on the Earth's Climate. *Science*, 215(4539):1498–1501, 1982. doi: 10.1126/science.215.4539.1498.

Sousa, P. M., Trigo, R. M., Barriopedro, D., Soares, P. M. M., and Santos, J. A. European temperature responses to blocking and ridge regional patterns. *Climate Dynamics*, 50 (1-2):457–477, 2018. doi: 10.1007/s00382-017-3620-2.

Sprenger, M. and Wernli, H. The LAGRANTO Lagrangian analysis tool - Version 2.0. *Geoscientific Model Development*, 8(8):2569–2586, 2015. doi: 10.5194/gmd-8-2569-2015.

Sprenger, M., Fragkoulidis, G., Binder, H., Croci-Maspoli, M., Graf, P., Grams, C. M., Knippertz, P., Madonna, E., Schemm, S., Škerlak, B., and Wernli, H. Global Climatologies of Eulerian and Lagrangian Flow Features based on ERA-Interim. *Bulletin of the American Meteorological Society*, 98(8):1739–1748, 2017. doi: 10.1175/BAMS-D-15-00299.1.

Stefanon, M., Dandrea, F., and Drobinski, P. Heatwave classification over Europe and the Mediterranean region. *Environmental Research Letters*, 7(1):014023, 2012. doi: 10.1088/1748-9326/7/1/014023.

Steinfeld, D. and Pfahl, S. The role of latent heating in atmospheric blocking dynamics: a global climatology. *Climate Dynamics*, 53(9-10):6159–6180, 2019. doi: 10.1007/s00382-019-04919-6.

Teubler, F. and Riemer, M. Dynamics of Rossby wave packets in a quantitative potential vorticity–potential temperature framework. *Journal of the Atmospheric Sciences*, 73 (3):1063–1081, 2016. doi: 10.1175/JAS-D-15-0162.1.

Tibaldi, S. and Molteni, F. On the operational predictability of blocking. *Tellus A*, 42(3): 343–365, 1990. doi: 10.1034/j.1600-0870.1990.t01-2-00003.x.

Trigo, R. M., Trigo, I. F., DaCamara, C. C., and Osborn, T. J. Climate impact of the European winter blocking episodes from the NCEP/NCAR Reanalyses. *Climate Dynamics*, 23:17–28, 2004. doi: 10.1007/s00382-004-0410-4.

Trigo, R. M., García-Herrera, R., Díaz, J., Trigo, I. F., and Valente, M. A. How exceptional was the early August 2003 heatwave in France? *Geophysical Research Letters*, 32(10), 2005. doi: 10.1029/2005GL022410.

Tyrlis, E. and Hoskins, B. J. Aspects of a Northern Hemisphere Atmospheric Blocking Climatology. *Journal of the Atmospheric Sciences*, 65(5):1638–1652, 2008. doi: 10.1175/2007JAS2337.1.

UNEP. Impacts of summer 2003 heat wave in Europe. *Environment Alert Bulletin*, 2004. URL `https://www.unisdr.org/files/1145_ewheatwave.en.pdf`. last accessed: 12.02.2020.

Vautard, R., Yiou, P., D'Andrea, F., de Noblet, N., Viovy, N., Cassou, C., Polcher, J., Ciais, P., Kageyama, M., and Fan, Y. Summertime European heat and drought waves induced by wintertime Mediterranean rainfall deficit. *Geophysical Research Letters*, 34(7), 2007. doi: 10.1029/2006GL028001.

Vogel, M. M., Zscheischler, J., Wartenburger, R., Dee, D., and Seneviratne, S. I. Concurrent 2018 Hot Extremes Across Northern Hemisphere Due to Human-Induced Climate Change. *Earth's Future*, 7(7):692–703, 2019. doi: 10.1029/2019EF001189.

Wallace, J. M. and Hobbs, P. V. *Atmospheric Science: An Introductory Survey*. Elsevier Academic press, Amsterdam, 2006. 504 pp.

Wang, Z., Li, W., Peng, M. S., Jiang, X., McTaggart-Cowan, R., and Davis, C. A. Predictive skill and predictability of North Atlantic tropical cyclogenesis in different synoptic flow regimes. *Journal of the Atmospheric Sciences*, 75(1):361–378, 2018. doi: 10.1175/JAS-D-17-0094.1.

Watts, N., Amann, M., Ayeb-Karlsson, S., Belesova, K., Bouley, T., Boykoff, M., Byass, P., Cai, W., Campbell-Lendrum, D., Chambers, J., Cox, P. M., Daly, M., Dasandi, N., Davies, M., Depledge, M., Depoux, A., Dominguez-Salas, P., Drummond, P., Ekins, P., Flahault, A., Frumkin, H., Georgeson, L., Ghanei, M., Grace, D., Graham, H., Grojsman, R., Haines, A., Hamilton, I., Hartinger, S., Johnson, A., Kelman, I., Kiesewetter, G., Kniveton, D., Liang, L., Lott, M., Lowe, R., Mace, G., Odhiambo Sewe, M., Maslin, M., Mikhaylov, S., Milner, J., Latifi, A. M., Moradi-Lakeh, M., Morrissey, K., Murray, K., Neville, T., Nilsson, M., Oreszczyn, T., Owfi, F., Pencheon, D., Pye, S., Rabbaniha, M., Robinson, E., Rocklöv, J., Schütte, S., Shumake-Guillemot, J., Steinbach, R., Tabatabaei, M., Wheeler, N., Wilkinson, P., Gong, P., Montgomery, H., and Costello, A. The Lancet Countdown on health and climate change: from 25 years of inaction to a global transformation for public health. *The Lancet*, 391(10120):581–630, 2018. doi: 10.1016/s0140-6736(17)32464-9.

Weisheimer, A., Doblas-Reyes, F. J., Jung, T., and Palmer, T. N. On the predictability of the extreme summer 2003 over Europe. *Geophysical Research Letters*, 38(5), 2011. doi: 10.1029/2010GL046455.

Wernli, H. and Davies, H. C. A lagrangian-based analysis of extratropical cyclones. I:

The method and some applications. *Quarterly Journal of the Royal Meteorological Society*, 123(538):467–489, 1997. doi: 10.1002/qj.49712353811.

Wernli, H. and Schwierz, C. Surface Cyclones in the ERA-40 Dataset (1958–2001). Part I: Novel Identification Method and Global Climatology. *Journal of the Atmospheric Sciences*, 63(10):2486–2507, 2006. doi: 10.1175/JAS3766.1.

Whan, K., Zscheischler, J., Orth, R., Shongwe, M., Rahimi, M., Asare, E. O., and Seneviratne, S. I. Impact of soil moisture on extreme maximum temperatures in Europe. *Weather and Climate Extremes*, 9:57 – 67, 2015. doi: 10.1016/j.wace.2015.05.001.

Wilks, D. S. *Statistical methods in the atmospheric sciences*, volume 100. Elsevier Academic press, Amsterdam, Boston, 2011. 840 pp.

Wirth, V., Riemer, M., Chang, E. K. M., and Martius, O. Rossby Wave Packets on the Midlatitude Waveguide – A Review. *Monthly Weather Review*, 146:1965–2001, 2018. doi: 10.1175/MWR-D-16-0483.1.

WMO and WHO. *Heatwaves and Health: Guidance on Warning-System Development*. Number 1142. World Meteorological Organization and World Health Organization, Geneva, 2015. URL `http://www.who.int/globalchange/publications/WMO_WHO_Heat_Health_Guidance_2015.pdf`. 114 pp.

Woollings, T., Barriopedro, D., Methven, J., Son, S.-W., Martius, O., Harvey, B., Sillmann, J., Lupo, A. R., and Seneviratne, S. Blocking and its Response to Climate Change. *Current Climate Change Reports*, 4:287–300, 2018. doi: 10.1007/s40641-018-0108-z.

Xu, Z., FitzGerald, G., Guo, Y., Jalaludin, B., and Tong, S. Impact of heatwave on mortality under different heatwave definitions: A systematic review and meta-analysis. *Environment International*, 89-90:193–203, 2016. doi: 10.1016/j.envint.2016.02.007.

Yamazaki, A. and Itoh, H. Vortex-Vortex Interactions for the Maintenance of Blocking. Part I: The Selective Absorption Mechanism and a Case Study. *Journal of the Atmospheric Sciences*, 70(3):725–742, 2013. doi: 10.1175/JAS-D-11-0295.1.

Zschenderlein, P., Pfahl, S., Wernli, H., and Fink, A. H. A Lagrangian analysis of upper-tropospheric anticyclones associated with heat waves in Europe. *Weather and Climate Dynamics*, 1:191–206, 2020. doi: 10.5194/wcd-1-191-2020.

Zschenderlein, P., Fragkoulidis, G., Fink, A. H., and Wirth, V. Large-scale Rossby wave and synoptic-scale dynamic analyses of the unusually late 2016 heatwave over Europe. *Weather*, 73(9):275–283, 2018. doi: 10.1002/wea.3278.

Zschenderlein, P., Fink, A. H., Pfahl, S., and Wernli, H. Processes determining heat waves across different European climates. *Quarterly Journal of the Royal Meteorological Society*, 145(724):2973–2989, 2019. doi: 10.1002/qj.3599.

Acknowledgements

I want to express my deepest gratitude to my supervisor Andreas H. Fink for giving me the opportunity to work on this interesting research area, for his guidance, for the scientific discussions and for giving me the freedom to pursue my own research interests. I also want to thank Volkmar Wirth and Joaquim Pinto for numerous scientific discussions during several meetings. My sincere thanks also go to Peter Knippertz, our group leader, for welcoming me in his group, for doing research on giant dust particles and for organising the famous summer partys with our working group and his family.

Collaboration in science is fundamental, because new and interesting ideas usually result from discussions. As such, many people contributed to this thesis and accompanied me during my doctorate. In particular, I want to express my deep sense of gratitude to Stephan Pfahl and Heini Wernli, with whom I collaborated nearly during my entire doctorate. Thank you for scientific discussions at ETH Zürich and later at FU Berlin, when Stephan moved there. I am really grateful to the folks in our working group "Atmospheric Dynamics", especially Michael Maier-Gerber, Andreas Schlüter, Marlon Maranan, Florian Pantillon, Josef Njeri, and Peter Vogel, for discussions on science, programming, politics and other topics :). My thanks also go to my project partner, Georgios Fragkoulidis, for analysing the Rossby wave packages of the 2016 heat wave and especially the pleasant collaboration in our project C4. Many thanks Julian Quinting, for discussions on forward trajectories, backward trajectories, European heat waves, Australian heat waves and the continuous support in case of technical problems with LAGRANTO. Data is fundamental for scientific work, I am therefore grateful to Christian Grams for granting access to various datasets, which his group is steadily downloading from ECMWF. Moreover, I want to thank the whole Waves to Weather Team, for the various ECS meetings and many valuable conversations on our projects. In particular I want to thank Florian Baur and Marlene Baumgart for the teamwork in the ECS Committee! I am also thankful to Lukas Papritz, Matthias Röthlisberger and Daniel Steinfeld for discussions during my research visit at ETH Zurich.

Last but not least I want to thank my friends for the continuous support and especially my parents, for their unlimited support, encouragement and love. It wouldn't have

happened without you! Thank you!!